ABSTRACT

Title of Thesis: HARMONIC VIBRATION DURABILITY OF LOW-TEMPERATURE SOLDER INTERCONNECTS IN PRINTED BOARD ASSEMBLIES

Thesis Directed by: Jonathan Martin, Master of Science
Dr. Abhijit Dasgupta

The harmonic vibration durability of several low-temperature solder (LTS) interconnects in printed board assemblies (PBA) is examined and compared against benchmark results from SAC305 interconnects. Test vehicles consist of 24 surface-mounted daisy-chained components assembled on an FR4 substrate, including four replicates each of CTBGA192, CVBGA228, CABGA360, and QFN68 components. Each test vehicle is assembled using one of four distinct solder alloys, consisting of either SAC305, LTS1, LTS2, or LTS3. All the BGA interconnects are hybrid bi-material joints with SAC305 ball and respective LTS solder paste. All specimens were isothermally pre-aged at a selected condition and then instrumented with strain gauges, accelerometers and resistance measurement wires to quantify the response and electrical continuity.

Vibration durability testing of all test specimens was conducted under clamped-free-clamped-free (CFCF) boundary conditions, using harmonic excitation at the test vehicles' first resonant frequency. The first resonant frequency was identified for each test specimen using a sine-sweep test and the load levels for the durability tests were established by identifying the overstress limit (through stepped-stress testing) for one SAC305 board and one representative LTS board.

During durability trials, components were considered to have failed when the resistance of the corresponding daisy-chain net exhibited at least a 20% increase, over five consecutive scans. The flexural strain amplitudes in the PBA at the footprint of each component (estimated with a calibrated dynamic finite element model of the PBA) and the cycles-to-failure (CTF) of each component were used to construct durability plots for each tested solder alloy and for all four tested component types.

A multiscale finite element modeling approach was developed to estimate the volume-averaged Von Mises' strain within the critical region of the critical solder joints of the CABGA192 and QFN68 components. This was accomplished by starting with the calibrated PBA model mentioned above, which is a simplified linear model that was calibrated against the measured dynamic behavior (natural frequency and response amplitude) of the PBAs under test. The calibrated global model provided nodal displacement boundary conditions to detailed local nonlinear half-models of the modeled components, enabling solder strain estimation in the critical solder joint, for fatigue characterization. All solders were modeled with SAC305 stress-strain curves since LTS stress strain curves are not widely available. The solder strain at the failure site was used to develop strain-life (SN) fatigue models for all four tested solders. SN models showed that all LTS joints consistently outperformed the SAC305 joints across all component types, with LTS3 generally exhibiting the best vibration durability. The alloy with the highest vibration durability was dependent on component type and response level, with LTS3 and LTS1 generally showing the highest durability.

Destructive failure analysis was conducted for all component styles. For the BGA component styles, cracking generally occurred in the neck region of the solder ball, with no copper trace failures being observed. In the QFN68 components, fatigue crack locations were found in the

bulk of the solder (biased towards the component side), and in some cases, also in copper traces. Thus, the SN models presented here are considered to be lower-bound representations for design purposes.

Analysis of the strain and acceleration test data revealed the onset of superharmonic response due to non-linear dynamic behavior at large base excitation levels. In some cases, this nonlinearity allowed transfer of energy to the third resonant mode although the excitation was only in the first resonant frequency. There was significant piece-to-piece variability of this nonlinear response. Nonlinear Finite element analysis confirmed that this variability is attributed to resonance dependent amplification, which occurs when the third superharmonic frequency coincides with the third resonant frequency of the test vehicle, resulting in a substantial increase in the third mode response.

In summary, this work has provided strain-based vibration durability assessments for selected high-Bi LTS interconnects, by relating the local PBA flexural strain amplitudes and solder strain amplitudes to CTF across multiple component geometries. The combined experimental and finite element methodology used in this study establishes a framework for vibration fatigue characterization and provides a method for developing high-cycle fatigue (HCF) models for solders, under harmonic loading. The study also elucidates the sensitivity of the interconnect strain fields, and resulting HCF response, on: (i) hybrid bi-material construction of BGA joints; and (ii) geometric differences between BGA and QFN interconnects.

HARMONIC VIBRATION DURABILITY OF LOW-TEMPERATURE SOLDER INTERCONNECTS IN PRINTED BOARD ASSEMBLIES

BY

JONATHAN MARTIN

THESIS SUBMITTED TO THE FACULTY OF THE GRADUATE SCHOOL OF THE UNIVERSITY OF MARYLAND, COLLEGE PARK, IN PARTIAL FULFILLMENT OF THE REQUIREMENTS FOR THE DEGREE OF

MASTER OF SCIENCE

2026

ADVISORY COMMITTEE:
Dr. Abhijit Dasgupta, Chair
Dr. Michael Osterman
Dr. Amr Baz

ACKNOWLEDGEMENTS

The CALCE Consortium has served the electronics industry for more than 40 years, providing a knowledge and resource base for the development and sustainment of competitive electronics products and systems. CALCE members define research needs and direction and share in the findings. The author would like to thank several graduate research assistants who supported this study, including but not limited to Idowu Olajire Olatunji, Randall Silvestro, Jonathan Hower, and Louis Hardock.

Thank you to all of those who have supported my thesis and provided assistance to me over the last two years.

I'd like to thank my advisor Dr. Ahbijit Dasgupta for taking me on, first as an intern, then later as a graduate student. Dr. Dasgupta has guided me over the last two years and provided me with the opportunity to learn more than I ever could have hoped. His vast knowledge has encouraged me to be the best version of myself, both academically and personally.

I also want to thank my advisory committee, Dr. Michael Osterman and Dr. Amr Baz, for serving on my thesis committee, as well as the guidance they have provided throughout my thesis. I am grateful for all of the "A-Team" members who have provided their expertise and assistance.

Table of Contents

ABSTRACT ii

ACKNOWLEDGEMENTS ii

Table of Contents iii

List of Figures: viii

Chapter 2 Figures: viii

Chapter 3 Figures: ix

List of Tables: xii

Chapter 2 Tables: xii

Chapter 3 Tables: xii

1. CHAPTER 1: INTRODUCTION 1

1.1. Background, Motivation, and Problem Statement 1

1.2. Scope of Thesis 3

CHAPTER 2: HARMONIC VIBRATION EXPEIRMENTS 5

2.1. Introduction 6

2.2 Materials and Experimental Methods 8

2.2.1. Test Specimen: Surface Mounted Printed Board Assembly (PBA) 8

2.2.2. Test Setup: Instrumentation, Data Acquisition Systems (DAQs), and Post-Processing 13

2.2.3. Test Matrix: Design of Experiment 17

2.2.4. Aging Protocol 19

2.2.5. Vibration Testing Methodology 19

2.2.5.1. Dynamic Considerations for Vibration Testing 19

2.2.5.2. Vibration Test Procedure 20

2.3. Results and Discussion 22

2.3.1. Sine-Sweep Results 22

2.3.2. Nonlinear Response of CFCF PBAs 26

2.3.3. Overstress Test Results 26

2.3.4. Failure Data and Fatigue life Results 27

2.3.5. Failure Analysis 31

2.4. Conclusions and Future Work 36

Acknowledgement 37

Funding Data 38

Conflict of Interest 38

Data Availability Statement 38

Nomenclature 38

A.2. Appendices 38

A.2.1 Multiscale Finite Element Model to Estimate Flexural Strain Distribution 39

A.2.2 Nonlinear Analysis of the CFCF PBA 41

References 47

CHAPTER 3: FINITE ELEMENT MODELING 50

3.1 Introduction 50

3.2 Summary of Experimental Results 54

3.3 Finite Element Modeling 60

3.3.1 Global/Local Sub-modeling Approach 61

3.3.2 Modeling of Materials 62

3.3.3 Global Model (GM) 62

3.3.4 Global Model (GM) Calibration 65

3.3.4.1 Stiffening Effect due to Components 66

3.3.4.1.1 Neutral Surface Calibration 66

3.3.4.1.2 Stiffening Factor 67

3.3.4.2 Calibration of Resonant Frequencies 69

3.3.4.3 Calibration of the Dynamic Strain and Acceleration Responses 70

3.3.5 Local Half Model 71

3.4 Results and Discussion 74

3.4.1 Strain Transfer Functions 75

3.4.2 Fatigue Life Curves 77

3.4.2.1 Influence of Strain State (Triaxiality Ratio) on Solder Joint Fatigue 80

3.4.2.2 Influence of Hybrid Construction on Failure of LTS Joints 82

3.4.3 Non-linear Vibration Contributions in CFCF Test Setups 83

3.4.4. Validation of Quasi-Static LHM Assumption 84

3.5 Conclusion 85

A.3. Appendices 86

A.3.1 Material Properties 87

A.3.2 Mesh Sensitivity Analysis 88

A.3.3 Nonlinear Response Leading to Super-Harmonics of a PBA 90

Acknowledgement 93

Funding Data 93

Conflict of Interest 93

Data Availability Statement 93

Nomenclature 93

References 95

Chapter 4: Conclusions, Contributions, Future Work 99

4.1. Conclusions, Contributions, Future Work 99

4.1.1. Summary and Conclusions 99

4.2. Contributions 103

4.3. Future Work 105

BIBLIOGRAPHY 107

List of Figures:

Chapter 2 Figures:

Figure 1. Test Vehicle and Different Component Styles 9

Figure 2. Hybrid LTS Solder Ball (adapted from [20]) 9

Figure 3. SEM and EDS Mapping of LTS1 BGA192 11

Figure 4. SEM and EDS Mapping of LTS3 BGA192 12

Figure 5. Vibration Test Setup and Test Vehicle Mounted in Fixture 14

Figure 6. Location of Strain Gauges and Board Accelerometers 16

Figure 7. High-level Overview of Test Setup and Closed-Loop Control Algorithm 16

Figure 8. Strain Contour Plot of Mode 1 18

Figure 9. Sample of Sine-Sweep Test 22

Figure 10. First Natural Frequency of Each Test Vehicle at Start of Test 23

Figure 11. Control Algorithm Software Depiction of the Board-Band Sine-Sweep 23

Figure 12. FFT of Strain Gauge at Location A 25

Figure 13. Crack Initiation (2% resistance increase) and Propagation to Failure for QFN68 and CABGA192 (20% resistance increase) components 28

Figure 14(a)(b)(c)(d). Fatigue life Plots for Each Component Style 30

Figure 15. Failure Analysis Cross-Sectioning Orientation 31

Figure 16. Side View of SAC305, CABGA192 32

Figure 17. Side View of LTS3, CABGA192 32

Figure 18. Side View of LTS2, CABGA192 33

Figure 19. Side View of LTS3, QFN68 33

Figure 20. SEM Imaging of Etched QFN68 Copper Trace Crack 34

Figure 21. Cross-Polarized Side View of Healthy CABGA192 SAC305 Interconnect 35

Figure 22(a)(b). Cross-Polarized Side View of Failed CABGA192 SAC305 and LTS3 Interconnect, respectively 35

Figure 23. Side View of LTS3, CTBGA228 36

Figure 24. Side View of LTS3, CVBGA360 36

Figure 25. Local Half-Symmetry Model of CABGA192 40

Figure 26(a)(b)(c). FE Estimation of First Three Mode Shapes 40

Figure 27. Base Excitation vs PB Strain Response showing nonlinear transmissibility 41

Figure 28. Time History of Board Response (g) during High Excitation 42

Figure 29. FFT of Board Response (g) under Low and High Excitation, showing Spurious Nonlinear Third Superharmonic Response Under Mode 1 excitation 42

Figure 30. Board Response Amplitude as a Function of the Ratio of the 3:1 Superharmonics for LTS3 #2 (Overstress Test) 43

Figure 31. 3:1 Ratio of SG4, sorted by Base Excitation (smallest to largest) 44

Figure 32(a)(b). Board Response Amplitude as a Function of the Ratio of the 3:1 Superharmonics for LTS2 #4 and LTS1 #2, respectively 44

Figure 33. Phase Shift between SG2 and SG4, sorted by Base Excitation (smallest to largest) 45

Figure 34. SG2 and SG4 Filtered Around ~600 Hz and ~200 Hz, respectively 46

Chapter 3 Figures:

Figure 1. Assembled Test Vehicle 54

Figure 2. Mounted Test Vehicle 55

Figure 3. Approximate Sensor Location and Nomenclature on Test Vehicle 56

Figure 4. FEM of the GM PB 63

Figure 5. Edge-Centered Virtual Strain Gauge on Global Model 64

Figure 6. Representative Virtual Strain Gauge on Global Model..... 64

Figure 7. Mesh Density of GM 65

Figure 8. Local Quarter-Symmetry Model (LQM) of QFN68, using Linear FE Analysis..... 67

Figure 9. Neutral Surface Shift Distribution Across the Entire Package Footprint for a QFN68 assembly..... 68

Figure 10. Component Shell Heights in Global Model 69

Figure 11. FEM PB Strain Response vs Time 70

Figure 12. Position of the LHM of the QFN68 & CABGA192 on the GM 73

Figure 13. Cross Section & Mesh of CABGA192 LHM..... 73

Figure 14. LHM of QFN68 Solder Joint Geometry & Cross Section 74

Figure 15. Critical Neck Region of CABGA192 Solder Ball..... 75

Figure 16. Critical Region of QFN68 Solder Joint 75

Figure 17. Representation of footprint of Corner Strain Gauge for the QFN68 component .. 76

Figure 18. Strain Transfer Functions for the QFN68 and CABGA192 assemblies..... 77

Figure 19(a)(b). Consolidated SAC305 Fatigue SN Curve, with and without QFN68 Data . 79

Figure 20. LTS Fatigue Life Curve for QFN68 Component 79

Figure 21. LTS Fatigue Life Curves for CABGA192 Components 80

Figure 22. Strain Triaxiality Ratio vs VM Strain in CABGA192 and QFN68 Components . 82

Figure 23. Triaxiality Ratio History for CABGA192 and QFN68 Components..... 82

Figure 24. FEA Approximation of LTS Hybrid BGA 83

Figure 25. Time Histories of PBA Accelerometer Reading: Ramp-Up (Low Load) and Dwell (High Load) 84

Figure 26. Mesh Density in Each Case 89

Figure 27. Results from Mesh Sensitivity Analysis 89

Figure 28. FEA Guided Locations where the PB is Artificially Stiffened 91

Figure 29. Analyzed Locations for Non-Linear Effect Analysis in FEA 91

Figure 30. Example of the FFTs Performed in this Analysis 92

List of Tables:

Chapter 2 Tables:

Table 1. Test Vehicle and Component Details 13

Table 2. Tested Solder Alloy Composition..... 13

Table 3. Table 3. Resonant Frequencies of Test Fixture 14

Table 4. Tests Matrix: Test type for Each Test Vehicle 18

Table 5. Summary of Base Excitation and Board Response 25

Table 6. Stepped-Stress Test Results for the LTS3 #2 Board..... 27

Table 7. Stepped-Stress Test Results for the SAC305 #3 Board..... 27

Table 8. Summary of Solder Interconnect Performance per Component Type..... 30

Chapter 3 Tables:

Table 1. Tested Solder Alloy Composition..... 55

Table 2. Summary of each Test Vehicles' Fundamental Frequency 57

Table 3. Summary of each Test Vehicles' Base Excitation, Board Response, and SG3 Response. Board (g) and SG3 (με) response show variability of ±79 g and ±145 με, respectively, at 90% confidence..... 58

Table 4. Fatigue Life Test Results for QFN68 from Prior Work [3]..... 59

Table 5. Fatigue Life Test Results for QFN68 from Prior Work [3]..... 60

Table 9. Neutral Surface Position in LQM and GM..... 69

Table 10. Comparison Between Measured and Calculated Resonant Frequencies 69

Table 11. FE Model Prediction vs Experimental Measurement..... 71

Table 6. Summary of Material Properties..... 87

Table 7. Detailed material properties for orthotropic materials 87

Table 8. Inelastic material properties for SAC305 88

Table 12. Summary of Case 1 and Case 2 FEA Natural Frequencies 91

Table 13. Summary of FFT Ratio Analysis 92

1. CHAPTER 1: INTRODUCTION

The background, motivation, problem statement, and structure of this thesis are presented in this Chapter. Further details regarding the gaps in the literature are presented in Chapters 2 and 3, in Sections 2.1 and 3.1 respectively.

1.1. Background, Motivation, and Problem Statement

The adoption of lead-free solders in the electronics industry was primarily driven by government regulations restricting the use of hazardous materials in electronic devices. In 2003, the European Union's Restriction of Hazardous Substances (RoHS) directive prohibited the use of lead (Pb), as well as other toxic materials, in electronic equipment.

As electronic assemblies grow increasingly miniaturized and complex, the reliability demands placed on solder interconnects have grown accordingly. Modern electronic components have become thinner and now incorporate greater numbers of semiconductors, interconnects, and embedded features. This added complexity introduces significant challenges during the solder reflow assembly process. The peak reflow temperatures required to melt conventional lead-free solders, such as SAC305, are upwards of 240°C. This causes thermal expansion mismatches between the semiconductor, substrate, and surrounding materials. These mismatches produce warpage of the printed board (PB) and component package, resulting in assembly defects such as head-on-pillow (HOP) and solder bridging, which compromise the integrity of the solder interconnect before the product even enters service.

To address this, low-temperature solders (LTS) have emerged as a viable alternative to SAC305, with melt temperatures between 139-150°C and peak reflow temperatures in the range of 170-180°C. LTS alloys significantly reduce the thermal excursion during assembly, thereby

mitigating warpage-induced defects. As a result, LTS materials have gained considerable interest from the electronics industry as a means of improving assembly yield without sacrificing interconnect performance.

However, the adoption of LTSs require a thorough understanding of their fatigue behavior under the loading conditions that electronic assemblies encounter while in service. Although the thermal cycling and mechanical shock reliability of LTS alloys has received growing attention in the literature, their behavior under vibration loading remains underrepresented. This is a significant gap, as vibration has been identified to cause approximately 16% of electronic failures, and harmonic vibration in particular represents a common and damaging loading condition found in many applications including automotive, aerospace, and industrial electronics.

Unlike thermal cycling, where damage accumulates slowly over many hours, vibration fatigue operates in the high-cycle regime, where millions of loading cycles can accumulate in a relatively short period of time. Knowledge of high-cycle fatigue (HCF) model constants is therefore essential for physics-based life prediction models that guide engineers in design decisions such as component placement, board mounting strategies, and the application of mechanical reinforcement methods. Without these model constants, engineers cannot reliably assess whether LTS assemblies will meet durability requirements in vibration sensitive applications, nor can they make informed comparisons when extrapolating design guidelines from SAC305 assemblies to new LTS assemblies.

SAC305 has been extensively studied under harmonic and random vibration loading, and a substantial body of fatigue data exists in the literature to support life predictions for SAC305 assemblies. No equivalent dataset currently exists for micro-alloyed LTS interconnects under vibration loading. *This thesis addresses that gap by characterizing the harmonic vibration*

fatigue behavior of three commercially available micro-alloyed LTS interconnects across multiple component styles, and by developing the fatigue model constants necessary for supporting physics-based life predictions of LTS assemblies.

1.2. Scope of Thesis

The findings of this thesis are presented in the form of two journal manuscripts prepared for submission to the ASME Journal of Electronic Packaging, organized in the two following chapters:

i) Chapter 2: Durability Comparison of Low-Temperature Solders Under Harmonic Vibration: Part 1 – Experiments

This chapter presents the experimental phase of the study, including the design of the test vehicle, vibration test methodology, and durability results for three commercially available LTS alloys and SAC305 across four component styles. Harmonic vibration durability tests were conducted at the first natural frequency of each test vehicle using a resonance tracking control algorithm. Failure analysis, through destructive cross-sectioning, was performed to identify the dominant failure mechanisms in each component style. A nonlinear dynamic response was observed in the experimental data and is also characterized using Fast Fourier Transform (FFT) and phase shift analysis.

ii) Chapter 3: Durability Comparison of Low-Temperature Solder Interconnects Under Harmonic Vibration: Part 2 – Modeling and Simulation

This chapter presents the multiscale finite element modeling framework developed to extract solder strain histories from the vibration durability experiments reported in Chapter 2. A calibrated global model of the printed board assembly (PBA) is used to

estimate the printed wiring board (PWB) strain amplitudes at consistent locations across all test vehicles, which were used to develop durability plots presented in Chapter 2. A detailed nonlinear local half model of the CABGA192 and QFN68 components is used to estimate solder strain amplitudes within the critical solder joints. These estimated strains are combined with the experimental cycles-to-failure data to develop strain-based fatigue models for each tested solder alloy for the CABGA192 and QFN68 components. Final summary, conclusions and future work are discussed in Chapter 4.

CHAPTER 2: HARMONIC VIBRATION EXPEIRMENTS

ABSTRACT – ABSTRACT – Low-temperature solder (melt temperature between 139-150°C) have gained interest for printed board assembly (PBA) solder interconnection as a means of reducing warpage defects such as head on pillow (HOP). While fatigue life has been investigated for drop and thermal cycling, studies on vibration fatigue life have not been presented. This paper presents testing of low temperature solders (LTS) under harmonic excitation. All assemblies were thermally aged prior to vibration testing. Components on all PBAs were daisy-chained to allow for individual in-situ resistance monitoring, to evaluate the health of their solder interconnects. Prior to testing, a sine-sweep test was performed to identify the fundamental frequency of each PBA. Vibration tests were conducted at the first natural frequency using a resonance tracking control algorithm to maintain consistent board response levels. Vibration fatigue performance was quantified by relating cycles-to-failure (CTF) to local board flexural strain amplitudes, which were estimated using finite element analysis. Test results showed scatter due to test variability and nonlinear dynamic responses. Despite the variability, consistent fatigue life trends were apparent across the tested alloys. SAC305 solder interconnects consistently showed the lowest vibration fatigue life compared to the LTS interconnects, LTS1 and LTS3 demonstrated the highest vibration fatigue life overall. Failure analysis revealed that CABGA192 interconnects contained cracks through the neck region of the solder joint close to the component side. QFN68 interconnects often contained copper trace cracks in addition to cracks through the bulk of the solder.

Keywords: low-temperature solder (LTS), SAC305, Ball Grid Array (BGA), Quad Flat No-lead (QFN), SAC305, harmonic vibration fatigue life testing, finite element (FE)

2.1. Introduction

Since 2003, the use of lead-free solders has increased significantly due to government regulations, such as the European Union's Restriction of Hazardous Substances (RoHS) directive, which banned the use of lead (Pb), as well as other toxic materials, in soldered electronics [1]. While the restrictions were not globally adopted, the part manufacturers and electronic manufacturers converted to lead-free to avoid the complexity of supporting varying product configurations based on different geographic markets. At the time of the conversion, tin-silver-copper solder with a composition of 3.0% wgt silver (Ag), 0.5% wgt copper (Cu) and remainder tin (Sn), SAC305, became a widely used lead-free solder. SAC305 has been extensively studied under a variety of loading conditions including thermal cycling, random and harmonic vibration, and mechanical shock.

As electronic assemblies grow more complex and compact, ensuring the reliability of solder interconnects presents a challenge. With increasingly thinner electronic packaging, part and printed board (PB) warpage under the solder reflow assembly due to elevated temperatures (230-245℃) has resulted in an increase of assembly defects, such as head on pillow (HOP) and solder bridging [2,3]. The warpage is caused by thermal expansion mismatches between the semiconductors, substrates and surrounding materials during the thermal excursion for solder reflow [4-6]. The desire to reduce solder reflow assembly temperature has led to an interest in low-temperature solders (LTSs). LTSs have a melt temperature between 139-150℃ with a peak reflow temperature in the range of 170-180℃. Furthermore, vibration has been shown to cause

solder interconnects to fail and therefore must be studied to ensure the reliability of LTS assemblies.

As such, there are fewer vibration fatigue life studies in comparison to thermal cycling fatigue life, since vibration fatigue can be mitigated by careful design, such as component positioning, board mounting, and mechanical reinforcement (corner staking, edge bonding, underfill) [7,8]. These mitigation decisions still rely on an understanding of the solder alloy's high cycle fatigue (HCF) behavior. Knowledge of HCF life model constants is necessary for developing life prediction models that guide engineers in design decisions and in determining if and where mitigation strategies are needed.

Vibration fatigue life of PBAs assembled with SAC305 as well as SnPb solders have been investigated using both random and harmonic excitation [9-13]. In this study, harmonic vibration was selected due to its suitability for controlled reliability testing and ease of data extraction for fatigue model constants. Harmonic excitation provides a narrow-band, constant-amplitude loading condition, which is well suited for the development of fatigue life relationships and compatibility with finite element (FE) modeling. Tests are typically conducted at a single resonant mode, enabling simplified interpretation of the dynamic response and reducing uncertainty in strain and acceleration data.

LTSs remain under explored in comparison to SAC305 and SnPb. Although some work has been conducted on LTS materials, the majority of studies focus on mechanical shock and temperature cycling reliability. The LTSs evaluated in this paper have been reported in the literature to have outperformed SAC305 under thermal cycling [14]. Studies of mechanical shock have indicated that LTSs failure sooner that SAC305 [15,16]. While a limited amount of vibration related work does exist, it has primarily focused on eutectic SnBi alloys [17,18]. As a

result, the vibration fatigue life of micro-alloyed LTS interconnects, such as those presented in this study, remain insufficiently investigated.

To address the lack of board level vibration fatigue life data for LTS interconnects, this study evaluates the harmonic vibration performance of selected LTS interconnects in comparison to SAC305 baseline, using PBAs populated with both BGA and QFN components. Harmonic vibration testing is performed at the test vehicles' first resonant frequency. Experimental fatigue life results are supported by a multiscale finite element model used to estimate PBA strain distributions. In a complementary study, detailed finite element analysis (FEA) is used to estimate strain in the solder interconnects for the purpose of formulating vibration fatigue models, referenced as SN curves [19].

2.2 Materials and Experimental Methods

Details of the test vehicle design, test matrix, sensors and data acquisition setup, aging protocol, and the vibration testing procure are discussed for the tested solder interconnects in this section. These elements establish the framework used to generate the fatigue data presented in this study.

2.2.1. Test Specimen: Surface Mounted Printed Board Assembly (PBA)

Each test vehicle consists of a printed board assembly (PBA) with dimensions of 228 x 114 x 1.41 mm, as shown in Figure 1. Each PBA consists of a printed board, populated with 24 surface-mounted components. Component styles and details about the test vehicle are summarized in Table 1. Components and the printed board are designed with daisy-chain nets to permit in-situ real-time resistance monitoring during vibration testing, described later in Section 2.2.3.

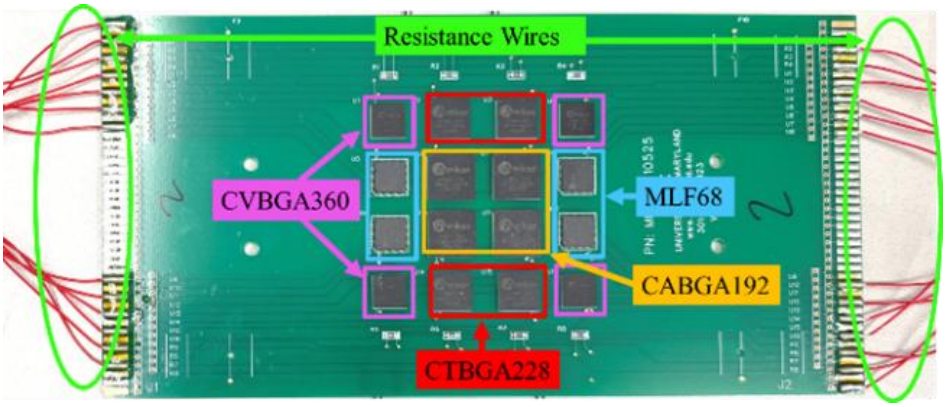

Figure 1. Test Vehicle and Different Component Styles

Separate test vehicles were created using one of four distinct solders: SAC305, LTS1, LTS2, and LTS3 (compositions defined in Table 2 based on x-ray fluorescence (XRF) spectroscopy). For ball grid array parts in LTS test vehicles, the solder interconnects were hybrid created by the combination of LTS paste and SAC305 solder spheres. During reflow, the LTS diffuses into the SAC305, as illustrated in Figure 2 (adapted from [20]).

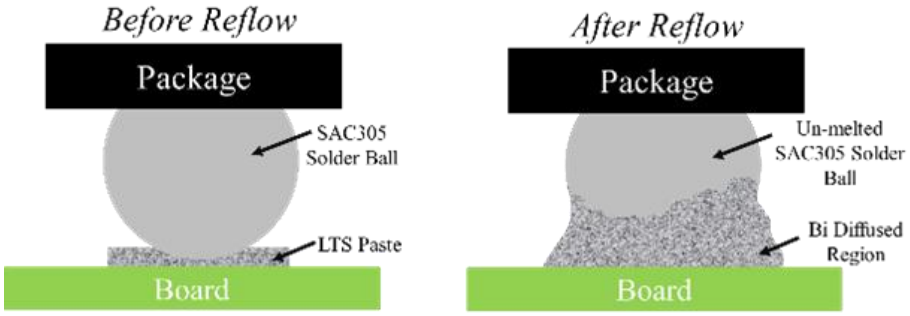

Figure 2. Hybrid LTS Solder Ball (adapted from [20])

The solder interconnects for the quad flat no-lead (QFN)s and resistors were assembled using a single distinct solder alloy corresponding to the test vehicle designation. It should be noted the center pad of the QFNs were not attached with solder.

Energy dispersive X-ray spectroscopy (EDS) was used to characterize the elemental distribution of Sn, Bi, and Ag within the LTS1 and LTS3 CABGA192 solder joints to ensure adequate separation between the SAC305 sphere and the reflowed LTS. EDS mapping for each interconnect is presented in Figure 3 and Figure 4. LTS1 and LTS3 were selected for this analysis as they contain the lowest and highest Bi content in this study. In the EDS maps, the colored regions indicate the presence of the respective element, while black regions represent its absence. These EDS maps show clear separation between the SAC305 sphere and reflowed LTS paste, with a narrow interdiffusion zone in between these two regions. The microstructure of the QFN68 copper traces and CABGA192 solder interconnect are presented and discussed in Section 2.3.4.

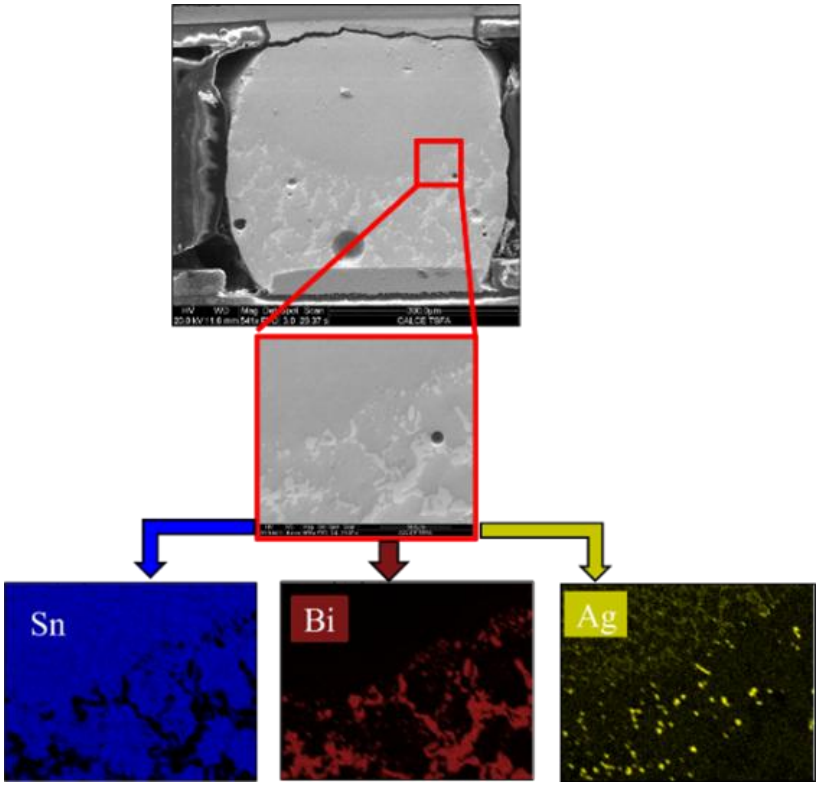

Figure 3. SEM and EDS Mapping of LTS1 BGA192

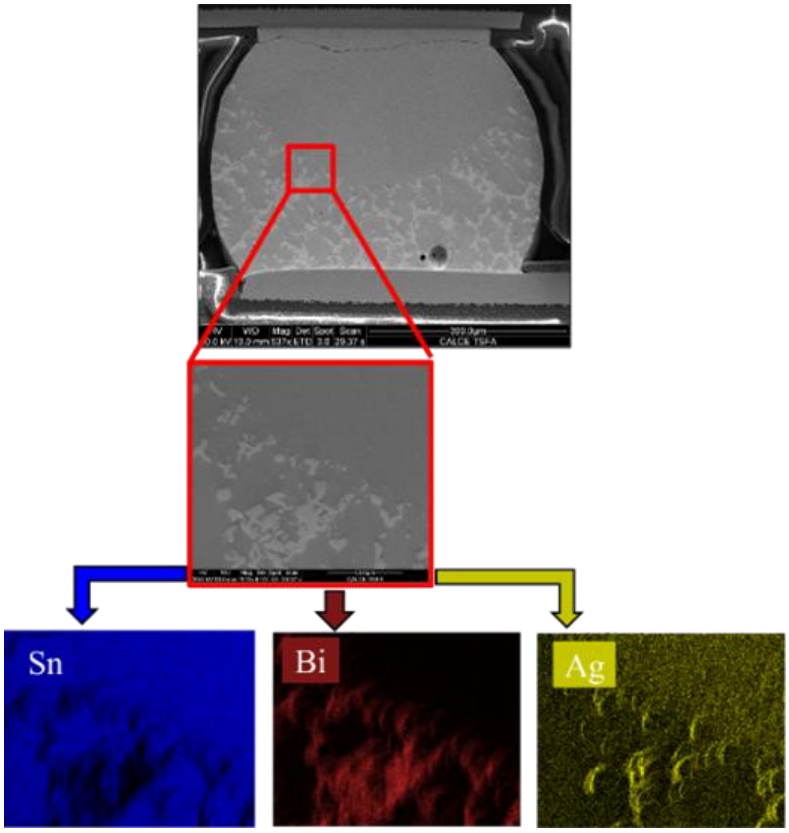

Figure 4. SEM and EDS Mapping of LTS3 BGA192

Table 1. Test Vehicle and Component Details

Board Details	Components	Count
• **4 Layers** • **228x114x1.41 mm** • **OSP**	CVBGA360, 10x10mm, SAC305 Ball Dia. 0.25 mm, Pitch 0.4 mm	4
	CTBGA228, 12x12mm, SAC305 Ball Dia. 0.3 mm, Pitch 0.5 mm	4
	CABGA192, 14x14mm, SAC 305 Ball Dia. 0.46 mm, Pitch 0.8 mm	4
	MLF68 (QFN68), 9.5x9.5 Pitch 0.5 mm	4
	1206 Resistor (50% Pad Width)	4
	1206 Resistor	4

Table 2. Tested Solder Alloy Composition

Source	Alloy	Melt Temp (℃)	Aging Temp (℃)
SAC305	SAC305	217	125
LTS1	Sn57.3Bi0.5Ag	137-142	62
LTS2	Sn56.2Bi1.4Sb	140-145	62
LTS3	Sn48.2Bi0.5Ag0.2Sb	145-150	62

2.2.2. Test Setup: Instrumentation, Data Acquisition Systems (DAQs), and Post-Processing

A custom vibration test fixture was designed to impose a clamped-free clamped-free (CFCF) boundary condition on the PBAs. The fixture consists of two ridged clamps secured to the shakers base plate using a consistent torque specification for all tests to ensure repeatability, lock washers were also used to ensure nuts/bolts did not come loose. Figure 5 depicts the test setup and mounted test vehicle.

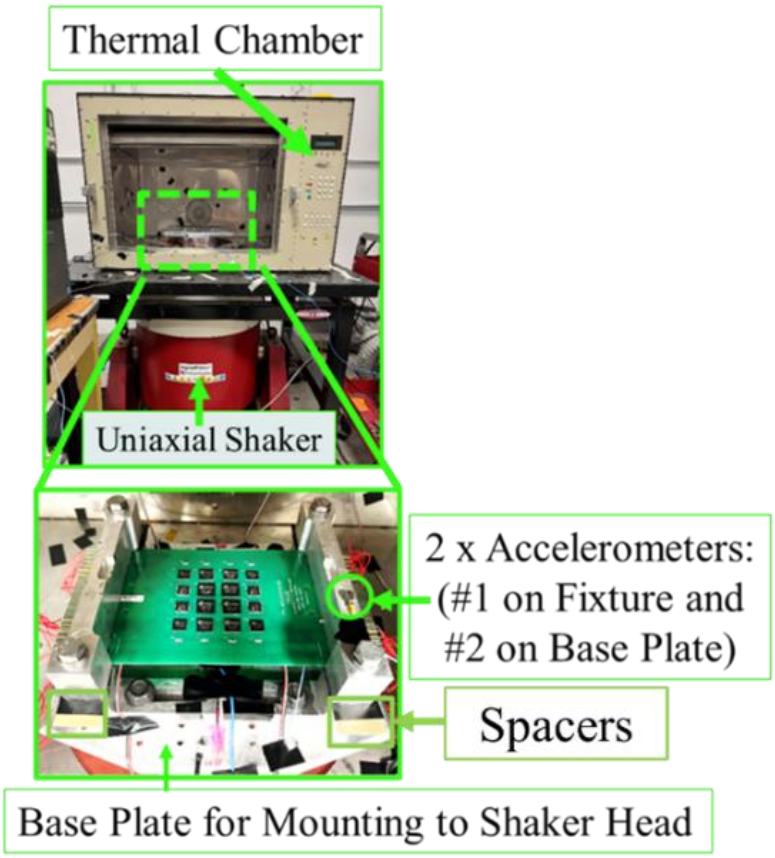

Figure 5. Vibration Test Setup and Test Vehicle Mounted in Fixture

To ensure that the fixture does not influence the dynamic response of the test vehicle during fatigue life testing, the resonant frequencies of the fixture were characterized using FEA. A summary of the fixture resonant frequencies is provided in Table 3. The suitability of the fixture for the present test program is later discussed in Section 2.3.1, where the tested natural frequencies of each test board is presented.

Table 3. Table 3. Resonant Frequencies of Test Fixture

Mode #	Frequency (Hz)
1	1846
2	3522
3	3583
4	3944

In this study, the unsupported span between the inner edges of the fixture clamps is nominally 152 mm (6 in). Vernier calipers were used to verify that the fixture was centered on the base plate and that the inner edges of the fixture were spaced 152 mm apart. To minimize relative motion between the fixed clamp and test vehicle, a compliant layer of electrical tape was applied to all clamping surfaces of the fixture, lock washers were also used. In addition, spacers with a thickness slightly less than that of the PBA was used in between each half of the fixture to ensure that the PBA was clamped uniformly across the surface.

Each test vehicle was instrumented with four strain gauges mounted on the unpopulated side of the PBA and positioned approximately mid-way underneath the following selected component footprints: CABGA192 and QFN68. In addition, two board accelerometers were mounted on the reverse side of the PBA near the center. The locations of the sensors are illustrated in Figure 6. One accelerometer was used to measure the dynamic response of the PBA and the other was used for the closed-loop feedback control algorithm used by the uniaxial electro-dynamic (ED) shaker. A schematic of the test setup can be seen in Figure 7, (adapted from [21]). In addition, there are two accelerometers located on the fixture base plate, one for measurement of the table excitation and the other as the main control sensor used for controlling the shaker's excitation level.

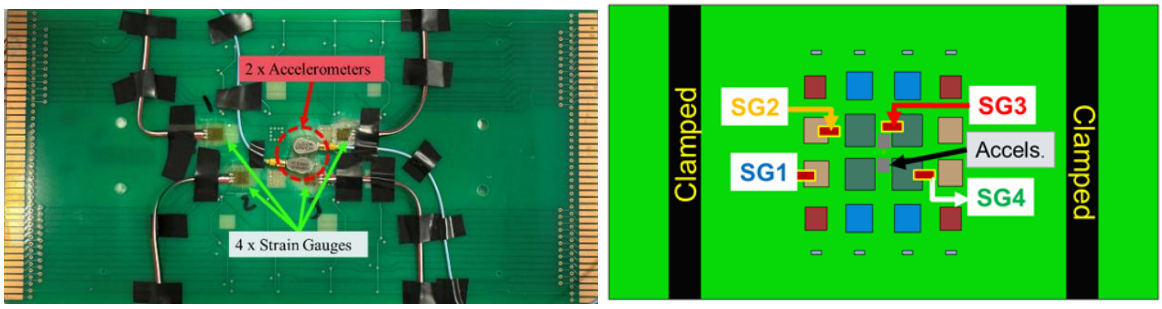

Figure 6. Location of Strain Gauges and Board Accelerometers

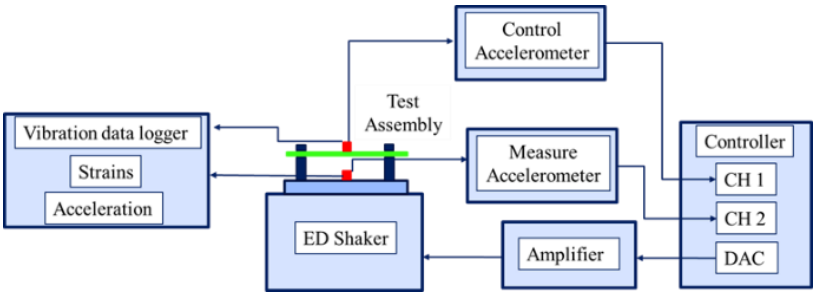

Figure 7. High-level Overview of Test Setup and Closed-Loop Control Algorithm

Based on the mode shapes predicted by FEA (see Appendices A.1), an additional strain gauge was instrumented on a sacrificial test board, the location of which was chosen to ensure that the second and third mode shapes of the PBA were captured. The mode shapes and position of the strain gauge at location A can be found in Figure 26 of Appendices A.1. This additional strain gauge was not used during fatigue life testing, but simply served as a method of validating the separation between the test frequency and modal frequencies. This is later discussed in Section 2.3.1.

The strain gauges and the two measured accelerometers (one on the PBA and one on the base plate) were sampled at a high sampling rate of 5000 samples per second using a multichannel DAQ. Sensor data collected by the DAQ was not part of the closed-loop feedback algorithm. The

sampling rate is 25x larger than the test frequency, more details about the test frequency will be discussed in Section 2.3.1.

Multi-strand wires were used to monitor the resistance of the daisy-chain net for each component, as shown in Figure 1. The resistance data was recorded using an independent DAQ at a rate of 1 sample/sec across all test vehicles. This sampling rate is the fastest for this system and is constant for all tests. The uncertainties introduced by this low sampling rate has been verified to have an insignificant effect on the CTF measurement.

2.2.3. Test Matrix: Design of Experiment

Fatigue life plots are established for each solder and component type. This was done by relating the local printed board (PB) strain response to the measured CTF. To build these relationships, failure data had to be collected at two different load levels that are sufficiently separated. The higher load level results in damage closer to low-cycle-fatigue, while the lower load level produces damage closer to high-cycle-fatigue.

To establish the appropriate load levels, a stepped-stress test was performed to quantify the overstress limit (i.e., PBA cyclic strain amplitude level (με)) that causes instantaneous failure of the interconnects. Failure in both the overstress and fatigue life tests were defined in accordance with IPC-9701 as a 20% increase of initial resistance over 5 consecutive scans [22].

Following the overstress test, fatigue life testing was conducted for each solder type. Each alloy was subjected to at least two fatigue life tests at two different load levels, as discussed above.

The excitation frequency for the harmonic overstress and fatigue life tests, was determined by performing an initial sine-sweep on each test board to identify the first natural frequency. All subsequent harmonic tests (both overstress and fatigue life tests) were conducted near this

resonant frequency to maximize the out-of-plane flexural response of the PBA, for an accelerated stress condition. The first mode shape can be seen in Figure 8. Table 4 summarizes the test type conducted on each test vehicle. Since every board was subjected to a preliminary sine-sweep, this step is not explicitly mentioned in the table.

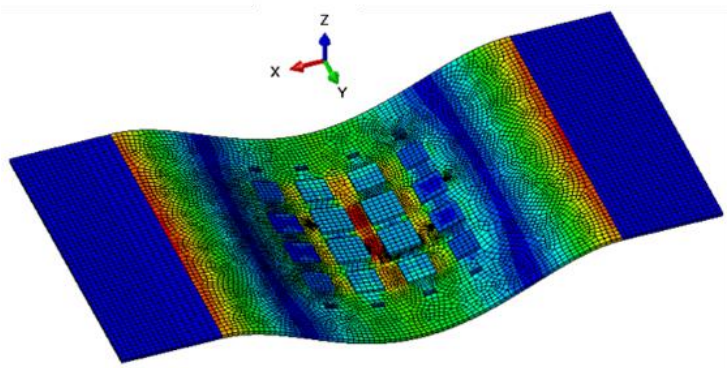

Figure 8. Strain Contour Plot of Mode 1

Table 4. Tests Matrix: Test type for Each Test Vehicle

Source	Test Vehicle ID	Test Type
SAC305	#1	Fatigue life
SAC305	#2	Fatigue life
SAC305	#3	Overstress
SAC305	#5	Fatigue life
LTS1	#1	Fatigue life
LTS1	#2	Fatigue life
LTS2	#1	Fatigue life
LTS2	#3	Fatigue life
LTS2	#4	Fatigue life
LTS3	#1	Fatigue life
LTS3	#2	Overstress
LTS3	#4	Fatigue life

2.2.4. Aging Protocol

To reduce differences in stress and metallurgical states, it is common practice to isothermally age test samples prior to vibration reliability testing. Subjecting the PBA to a period of elevated temperature can allow all test samples to be in the same approximate state. Based on solder, component, and printed board materials, isothermal aging can produce similar PBA to PBA residual stresses, and stabilization of several metallurgical processes (such as growth of intermetallic compounds (IMC), oxidation, and microstructural ripening) [22-24]. Since this study is focused on solder interconnects, each test vehicle was isothermally pre-aged, prior to testing, for 100 hours at approximately 0.8 homologous temperature of the solder, based on procedures presented in the literature [23]. Pre-aging conditions are summarized in Table 2.

2.2.5. Vibration Testing Methodology

The factors to be considered for a vibration fatigue life test is discussed in this section.

2.2.5.1. Dynamic Considerations for Vibration Testing

Before conducting vibration fatigue life tests, several dynamic considerations related to excitation control and instrumentation must be addressed.

The loading profile can be defined using the base accelerometer or the board accelerometer as the reference (control), prior studies typically use the base accelerometer as the reference [18,19]. When controlling at the base, the base excitation does not explicitly define the acceleration response of the PBA, evident by variations in the board transmissibility between test specimens. The fixture, clamps, and mounting interfaces introduce a frequency dependent transfer function between the base and the test specimen. As a result, the board response may deviate from the intended test specification. Kim et al. [25] demonstrated this effect in an environmental vibration study, showing that controlling at a location off of the specimen

produces significant differences between the intended and actual acceleration responses at the component mounting locations, which is an effect of dynamic interactions between the shaker, fixture, and specimen. Furthermore, the dynamic elastic response of the specimen itself adds to the difference between the acceleration measured at the base and the acceleration measured on the test specimen. For these reasons, the present study controls the vibration response using an accelerometer located near the center of the PBA, providing a loading condition more representative of what the mounted components actually experience during testing.

During vibration fatigue testing, the natural frequency of the PBA is known to drift as damage accumulates and the printed board material softens. The increasing gap between the resonant frequency and the excitation frequency progressively reduces the dynamic transmissibility of the PBA. Therefore, when controlling from the PBA at a fixed frequency, the shaker has to progressively supply more energy to maintain a constant response level. To overcome this limitation, this study uses a resonance-tracking control algorithm which continuously senses the current resonant frequency and adjusts the excitation frequency to follow shifts in the resonant frequency. This maintains a consistent transmissibility throughout the test, thus keeping the excitation level, as well as response level, relatively constant throughout the test. Related studies have been reported in the literature [21] where researchers evaluated the merits of resonance-control, but that study was controlling from the base, not from the PBA.

2.2.5.2. Vibration Test Procedure

After mounting each test vehicle in the fixture, a sine-sweep test is first performed to determine the first modal frequency. As an exploratory pre-test, an extended broad-band sine-sweep test was conducted on a sacrificial board from 100-1000 Hz to verify the modal frequencies and the absence of modal coupling (this is further disused in Section 2.3.1). A

representative sine-sweep response is shown in Figure 9. Since the first resonant frequency was found to be nominally around 205 Hz, the sine-sweep characterization for each fatigue life test specimen was conducted over 100-300 Hz bandwidth before the harmonic dwell fatigue life test to identify the precise resonant frequency (and hence excitation frequency) for each test specimen. Fatigue life tests were then conducted at a response level based on the results from the overstress test. Response level was characterized by PBA flexural strain level (με), instead of PBA acceleration level (g), due to large variations in the overstress limit (g) for different component types. This test was conducted by increasing the board response in steps of 25 g, with a 5-second dwell at each step.

Although acceleration serves as a convenient control metric, interconnect fatigue failure is ultimately driven by cyclic strains that are generated by PBA flexure. Therefore, the fatigue life tests were guided by achieving target PBA flexural strain levels rather than acceleration levels. The center strain gauge (SG3 shown in Figure 6) was used as the reference strain gauge for all tests. Results from the overstress test can be found in Section 2.3.3.

In summary, harmonic fatigue life tests were conducted using constant response amplitude at the first natural frequency of the test vehicle by controlling the PBA response with the center accelerometer using a resonance tracking algorithm. PBA strain levels at the edges of selected critical component types were recorded during each test for post-processing and finite element modeling (see Appendices A.1 for details). Two response levels (low and high) were selected for the fatigue life tests, using SG3 as the reference, to ensure sufficiently separated data points. However, an additional LTS2 and SAC305 board was tested due to elevated scatter observed in the initial failure data. A summary of the test excitation and sensor responses can be seen in Table 5.

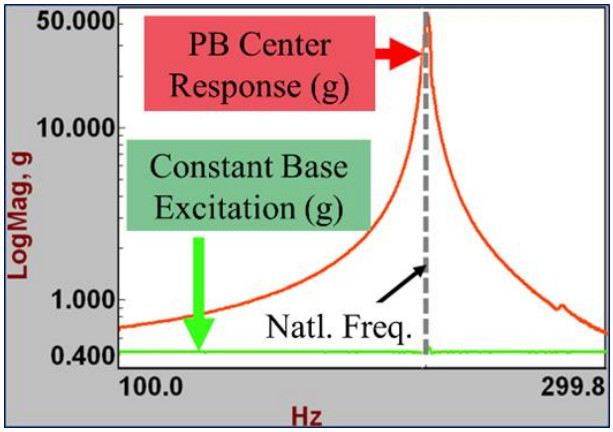

Figure 9. Sample of Sine-Sweep Test

2.3. Results and Discussion

Section 2.3 reports the results from the dynamic characterization and vibration fatigue life tests of all tested PBAs. The discussion begins with verification of the modal behavior, identified though sine-sweep tests, followed by the identification of nonlinear responses observed during testing. Failure progression, fatigue life trends, and dominant failure mechanisms are presented.

2.3.1. Sine-Sweep Results

All test boards exhibited a first natural frequency of approximately 200 Hz, a summary of the first natural frequencies for each test board can be seen in Figure 10. Using a sacrificial test board, an additional broadband sine-sweep was conducted over the range of 100 to 1000 Hz to verify that there were no modal frequencies near the test frequency (~200 Hz). The sweep revealed modal frequencies at approximately 200 and 590 Hz. Based on the predicted mode shapes (discussed in Appendices A.1), 200 Hz corresponds to the first modal frequency and 590 Hz corresponds to the third modal frequency. Figure. 11 depicts the control algorithm's real-time sine-sweep output, displaying both the base excitation (g), measured from the base plate's

accelerometer, as well as the response (g) near the PBA center, measured by the test vehicle's center accelerometer.

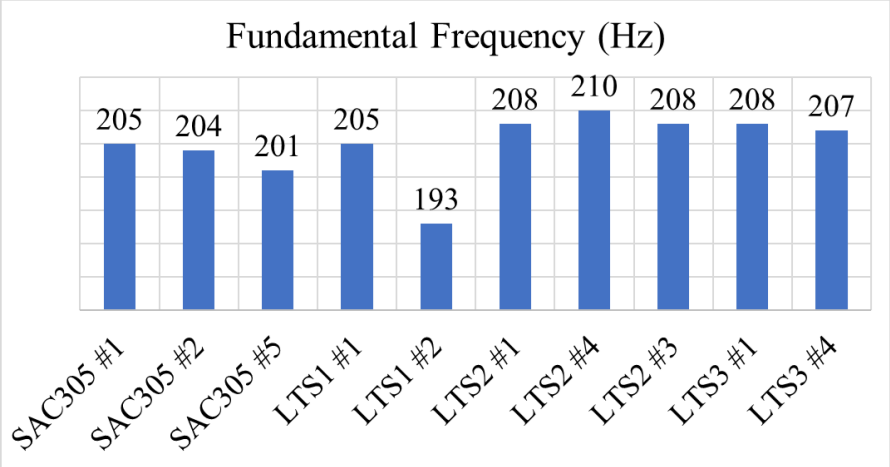

Figure 10. First Natural Frequency of Each Test Vehicle at Start of Test

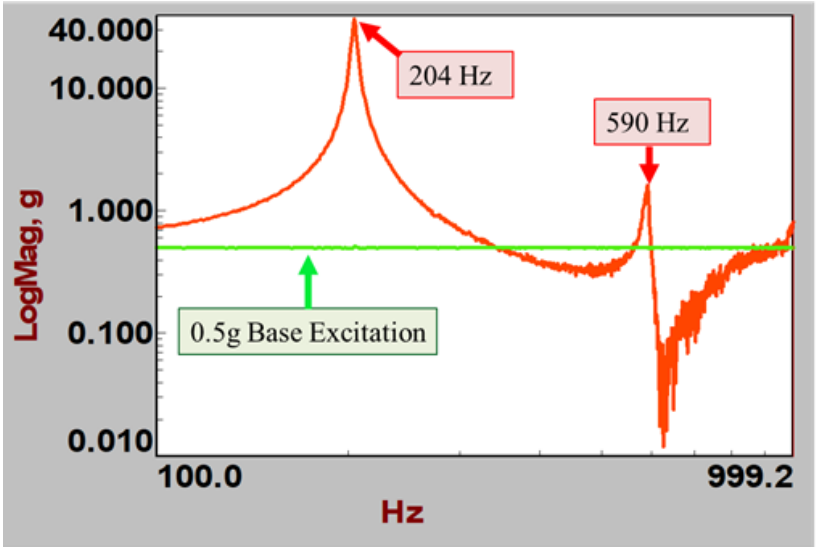

Figure 11. Control Algorithm Software Depiction of the Board-Band Sine-Sweep

As presented in Section 2.2, the first resonant frequency of the test fixture is approximately 1846 Hz (Table 3). Since all test boards exhibited a first natural frequency of approximately 200 Hz, the fixture resonant frequency is approximately nine times higher than that of the test vehicles. This large separation ensures that there is no dynamic coupling between the fixture and the PBA response, confirming that the current fixturing scheme is viable.

To confirm all modal frequencies, a strain gauge was placed at location A (see Appendices A.1). A Fast-Fourier-Transform (FFT) of the strain data from the broad-band sine-sweep test (seen in Figure 12) shows the first three modal frequencies. Comparison with Figure 11 confirms that the accelerometer at the PBA center did not detect Mode 2 (at 274 Hz), because it was located at a node line of Mode 2 (mode shape is seen in Figure 21b in Appendices A.1). This modal analysis confirms that harmonic excitation at the first modal frequency should not produce a strong direct response in Modes 2 or 3, as the modal frequencies are separated sufficiently apart.

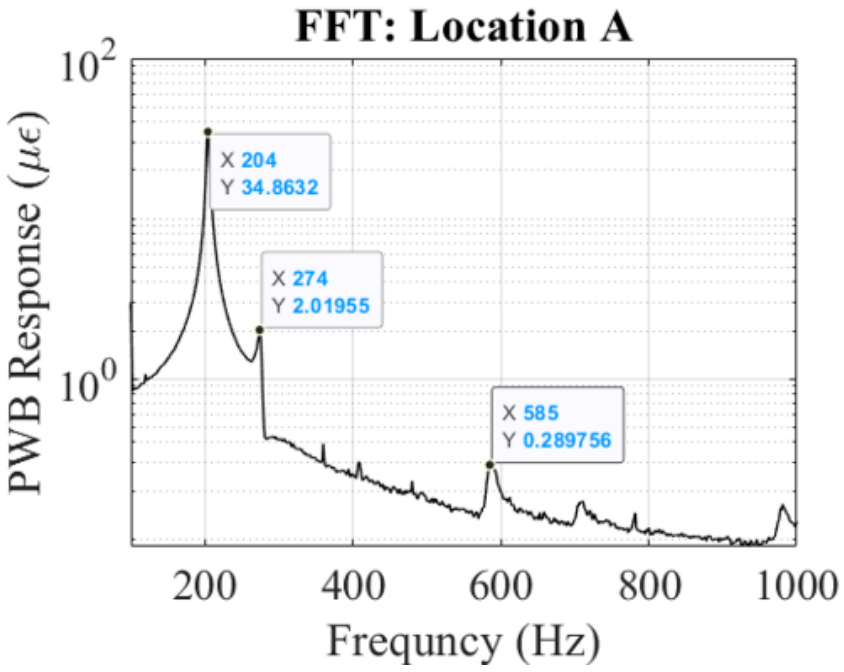

Figure 12. FFT of Strain Gauge at Location A

Table 5. Summary of Base Excitation and Board Response

Source	Test Vehicle ID	Base Excitation (g)	Board Response (g)	SG3 (με)
SAC305	#1	1.91	120	489
SAC305	#2	3.25	190	608
SAC305	#5	3.71	195	645
LTS1	#1	2.5	139	463
LTS1	#2	4.46	182	722
LTS2	#1	9.05	400	925
LTS2	#3	3.6	198	646
LTS2	#4	3.1	200	558
LTS3	#1	8.22	324	1023
LTS3	#4	2.93	161	575

2.3.2. Nonlinear Response of CFCF PBAs

Analysis of the strain and acceleration data from the overstress and fatigue life tests revealed the onset of a nonlinear dynamic response when the PBA experiences large response amplitudes. This nonlinearity manifests as a super harmonic response, where the PBA exhibits a non-harmonic response despite being subjected to harmonic excitation. As described by Porter and Brake [26,27], superharmonic resonances occur in nonlinear systems when the response contains significant frequency content at integer multiples of the forcing frequency. This behavior was confirmed through FFT analysis, which identified dominant frequency components at odd integer multiples of the first natural frequency (~200 Hz), occurring at approximately 600 Hz, 900 Hz, and 1200 Hz. Further discussion about this nonlinear response can be found in Appendices A.2.

This super harmonic response is important to the fatigue life test results because in some test specimens, frequency of one of the super-harmonic responses coincided with the third resonant mode. Consequently, Mode 3 had some participation in the test PBA response, although the excitation was at the first resonant mode, resulting in some degree of unexpected variability in the fatigue life test results. This nonlinear behavior is further discussed in Appendices A.2. in [19].

2.3.3. Overstress Test Results

As discussed in Section 2.5.2, sacrificial test boards were used to estimate the overstress limit, aimed at defining strain levels for the fatigue life tests. These tests were performed on LTS3 #2 and SAC305 #3. Target strain levels for the fatigue life tests were based on the overstress limit (με) for the CABGA192 components, which correspond to SG3. SG3 was chosen as the reference strain gauge since the CABGA192 components experience the largest

strain levels on the PB. Although prior studies recommend conducting fatigue life tests at 60-80% of the overstress limit [22], the selected strain levels in the present study were not strictly constrained within this range due to limitations associated with achieving the target strain responses. The majority of the strain levels during the vibration fatigue life tests ranged from approximately 53-86% of the measured overstress limit (με). The results for the stepped-stress-test can be seen in Table 6 and Table 7.

Table 6. Stepped-Stress Test Results for the LTS3 #2 Board

Component	SG3 (με)
CABGA192: U6	1061
CABGA192: U7	1076
CABGA192: U10	1076
CABGA192: U11	1076

Table 7. Stepped-Stress Test Results for the SAC305 #3 Board

Component	SG3 (με)
CABGA192: U6	872
CABGA192: U7	993
CABGA192: U10	763
CABGA192: U11	944

2.3.4. Failure Data and Fatigue life Results

As discussed in Section 2.2.3, each component has been daisy chained for in-situ resistance monitoring to assess the health of the interconnects for each component. Failure was defined in Section 2.2.2 as a 20% increase in initial resistance over 5 consecutive scans. A 2% resistance increase was considered to be a qualitative indicator of crack initiation and the time for resistance to increase from 2% to 20% was considered to be a qualitative indicator of the time for crack propagation from initiation to failure. Figure 13 illustrates the initiation and propagation

behavior for two selected components (CABGA192 and QFN68). These results indicate that crack initiation occurs earlier in CABGA192 solder interconnects compared to the QFN68 interconnects. However, the crack propagates more rapidly in the QFN68, leading to an earlier failure. Post-test cross-sectional analysis revealed that the cracking in the CABGA192 interconnects occurs through the neck region of the solder. In the case of the QFN68, cracking occurs through the bulk solder, and in some cases in the copper trace. Further details about failure analysis will be presented in Section 2.3.4.

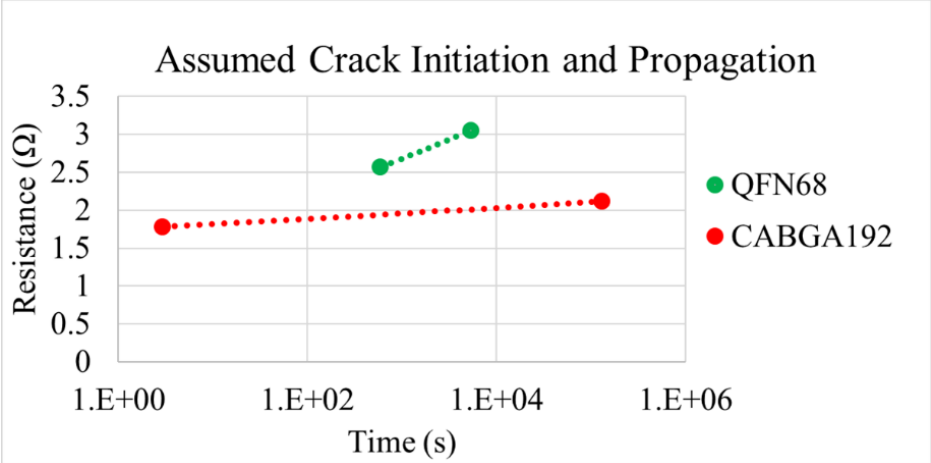

Figure 13. Crack Initiation (2% resistance increase) and Propagation to Failure for QFN68 and CABGA192 (20% resistance increase) components

The results of the fatigue life tests for each tested solder are presented for each component as CTF at a given strain level at the edge of the component. The strain levels were estimated using calibrated FEA with strain gauges positioned at the centered-edge of each component within the model, these are referenced as virtual strain gauges. This methodology produces less variability across each test vehicle, compared to using values from physical strain gauges (because of the variability in placement of the physical strain gauges on the test vehicles). The FEA models are

calibrated using the physical strain gauge outputs. Further details are presented in Appendices A.1.

The fatigue life comparison plots for each distinct solder interconnect for respective components can be seen in Figure 14(a)(b)(c)(d). Significant scatter is observed in the test data, which is attributed to variations in PBA dimensions, interconnect geometry, PBA alignment in the fixture, fixture clamping conditions, strain gauge and accelerometer placement, nonlinearities in the PBA dynamic response, and inherent variability in solder fatigue properties. While these plots do not reflect the solders' S-N fatigue properties, these plots still provide a relative ranking of the fatigue life of each solder type. It is noted that the LTS1 fatigue life curve for the CABGA192 and CTBGA228 components display an anomalous shallow slope relative to the other tested alloys. This behavior is attributed to the superharmonic response observed in the LTS1 #2 test board, the details of which are discussed in Appendices A.2

The fatigue life rankings were consistent across component types, with SAC305 exhibiting the shortest fatigue life in all cases. LTS1 and LTS3 provided the greatest vibration fatigue life for the CABGA192, QFN68, and CTBGA228 interconnects. For the CVBGA360, the three LTS alloys performed at similar levels, though LTS2 showed a slight edge over the other LTSs.

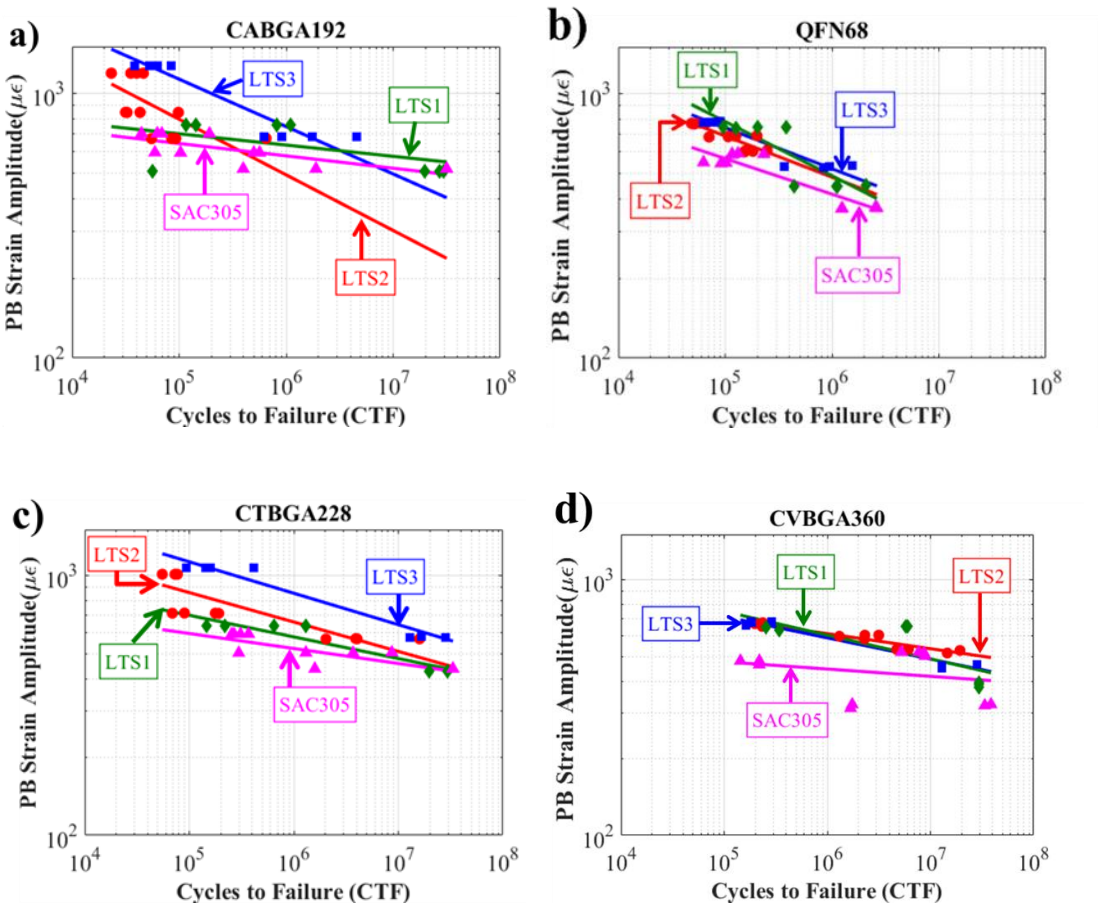

Figure 14(a)(b)(c)(d). Fatigue life Plots for Each Component Style

Table 8. Summary of Solder Interconnect Performance per Component Type

Component Type	Performance Ranking
CABGA192	LTS1&LTS3>LTS2>SAC305
QFN68	LTS1&LTS3>LTS2>SAC305
CTBGA228	LTS3>LTS2>LTS1>SAC305
CVBGA360	LTS2>LTS1&LTS3>SAC305

2.3.5. Failure Analysis

After harmonic vibration tests were completed, failure analysis was conducted for each component style, with a focus on the CABGA192 and QFN68 components to identify dominant failure sites. The failure analysis process was conducted on board sections with components being excised from the PBA and subjected to grinding/polishing from the unpopulated side of the PBA, to examine for copper traces for evidence of cracks, shown in Figure 15 (X orientation). Subsequent cross-sectioning was conducted in the orthogonal direction to the exposed trace surface, to examine the solder interconnects for evidence of cracks, shown in Figure 15 (Y orientation).

Figure 15. Failure Analysis Cross-Sectioning Orientation

Sectioned samples were examined under optical microscopy, cross-polarized microscopy (CPM), and scanning-electron microscopy (SEM). Copper trace failures were not observed in the CABGA192 components. The dominant failure site was solder cracking, typically found in the neck adjacent to the component bond pad, as seen in Figures 16-18. The QFN68 components contained copper trace cracks and solder cracks were found to be predominantly adjacent to the component termination, as seen in Figures 19 and 20, respectively. Cross-section images of the CTBGA228 and CVBGA360 components can be seen in Figures 23 and 24, respectively.

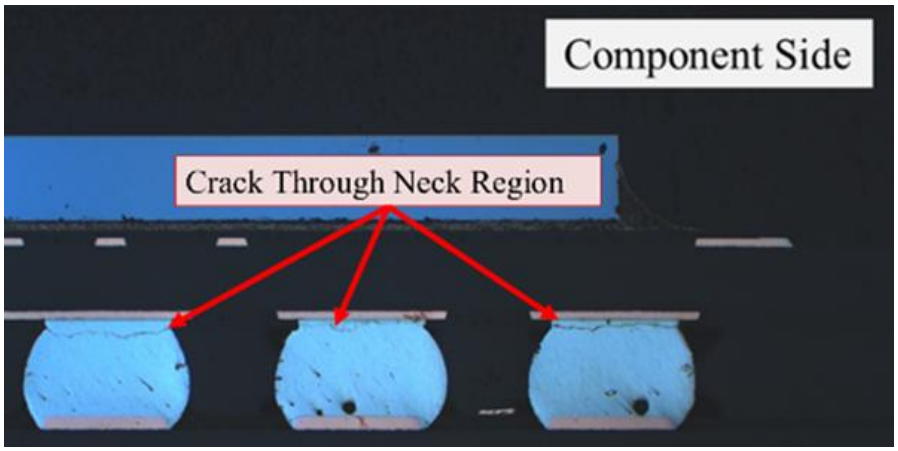

Figure 16. Side View of SAC305, CABGA192

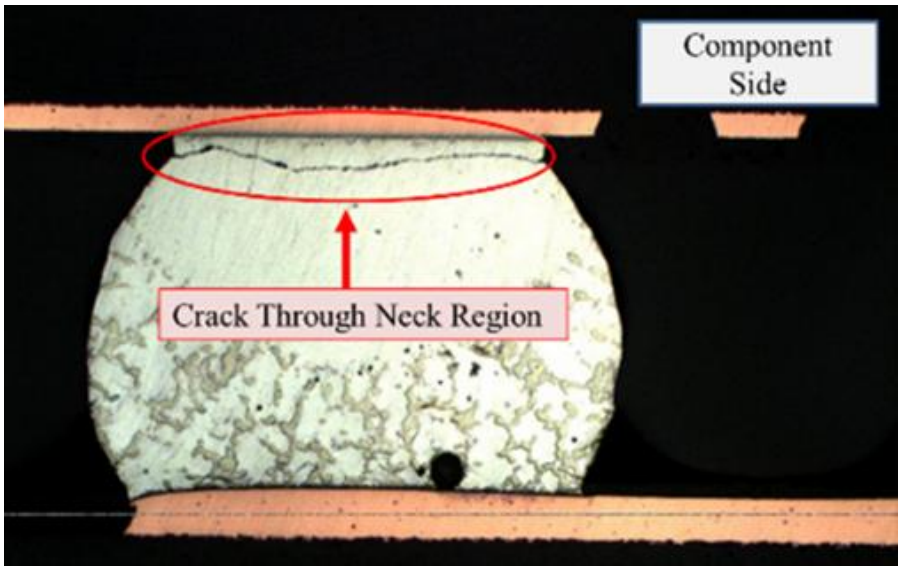

Figure 17. Side View of LTS3, CABGA192

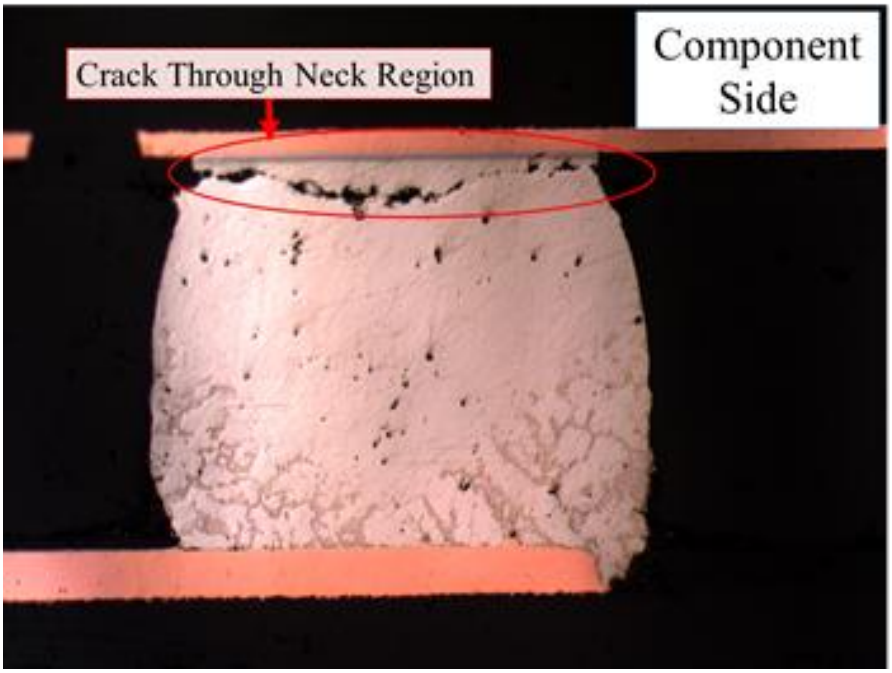

Figure 18. Side View of LTS2, CABGA192

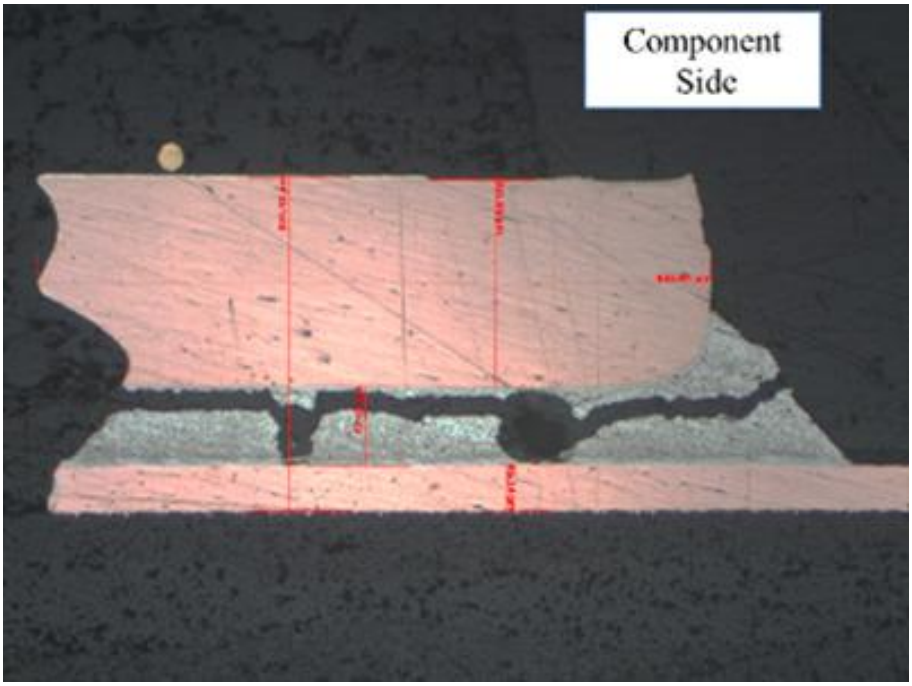

Figure 19. Side View of LTS3, QFN68

Copper trace failures, observed in the QFN68 components, prompted an investigation of the microstructure of the region where cracks had formed. The surface of the traces was chemically etched using a 1-to-1 solution of nitric acid and distilled water. SEM imaging was used to determine if cracks occurred along grain boundaries or through grains, which can be seen in Figure 20. This analysis revealed a mixed-mode fracture morphology, showing both intergranular and transgranular cracking.

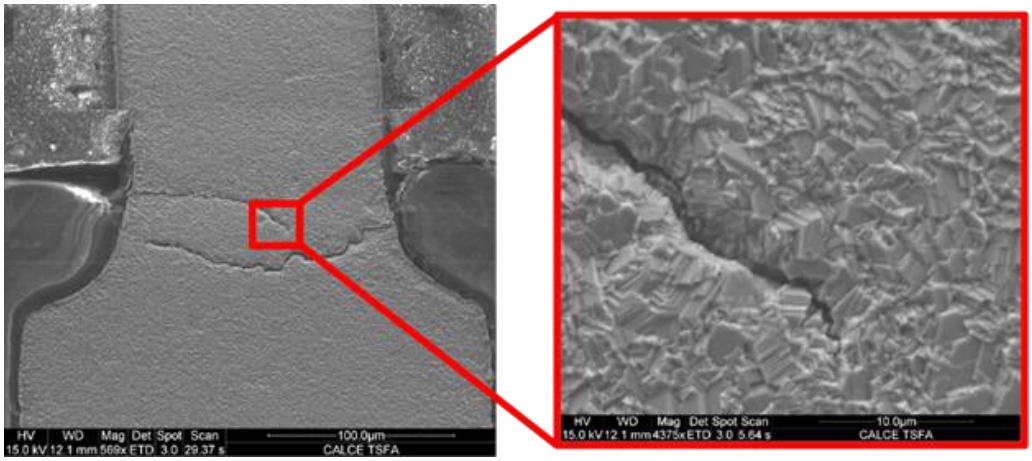

Figure 20. SEM Imaging of Etched QFN68 Copper Trace Crack

Cross-polarized microscopy of the CABGA192 interconnects revealed that intact interconnects typically contained a mix of one to three initial parent grains, as seen in Figure 21. In the failed interconnects, recrystallization was observed to nucleate subsidiary grains near the region surrounding the failure site, as seen in Figure 22(a)(b). The neck region acts as a stress concentration site during cycling vibration loading and is where the crack initiates. As the crack propagates, plastic strain builds up ahead of the crack tip, thus leaving a region of strain-induced recrystallized subsidiary grains in the wake of the propagating crack. This behavior was observed across all test boards.

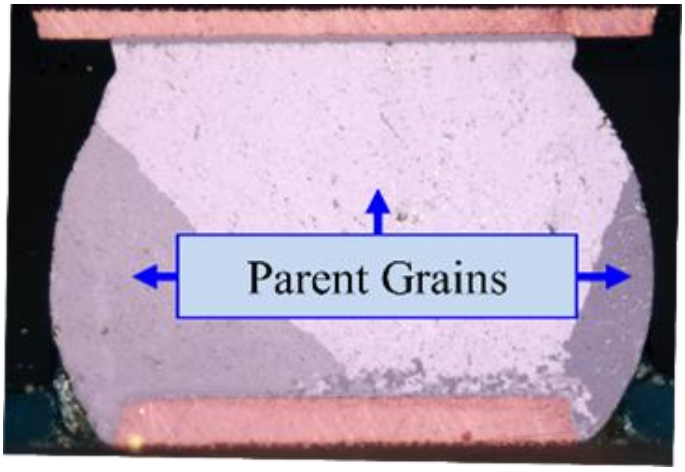

Figure 21. Cross-Polarized Side View of Healthy CABGA192 SAC305 Interconnect

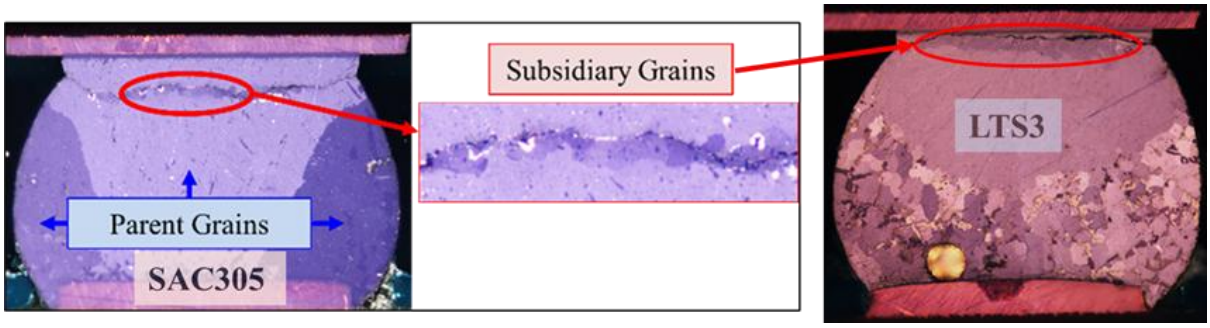

Figure 22(a)(b). Cross-Polarized Side View of Failed CABGA192 SAC305 and LTS3 Interconnect, respectively

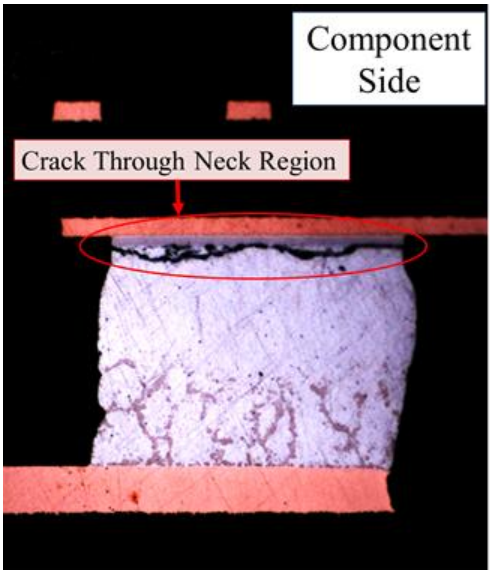

Figure 23. Side View of LTS3, CTBGA228

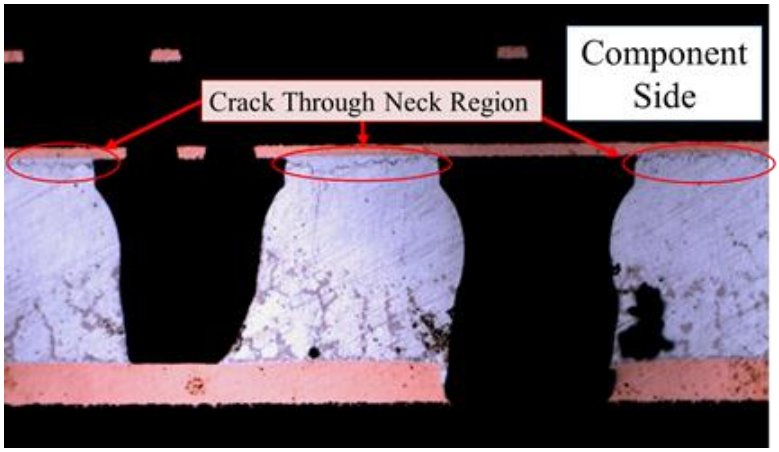

Figure 24. Side View of LTS3, CVBGA360

2.4. Conclusions and Future Work

Harmonic vibration fatigue of LTS is quantified on a relative scale by correlating cycles to failure (CTF) to local board flexural strain amplitudes (which are evaluated at component edges, estimated from FEA). The strain amplitudes were estimated with virtual strain gauges seeded into a calibrated finite element model (summarized in Appendices A.1.). The resulting fatigue

life trends for the LTS interconnects are compared to the benchmark result for SAC305 interconnects. There is variability in test data due to variance in PBA architecture, test conditions, nonlinear dynamic PBA response, and solder fatigue properties.

A method for detecting and assessing the unintended modal participation, caused by the superharmonic mechanism, was developed and presented.

Across all tested component styles, SAC305 interconnects consistently ranked last in vibration fatigue life. The CABGA192, QFN68, and CTBGA228 components assembled with LTS1 and LTS3 achieved the longest fatigue lives, while the CVBGA360 components showed less differentiation among the LTS alloys, with LTS2 performing slightly better than LTS1 and LTS3. A summary of the performance of each solder per component type can be seen in Table 8.

Future work should apply rainflow cycle counting to the PB strain histories to more accurately capture the cumulative fatigue damage. Additional testing at more load levels is recommended to improve the confidence of the fatigue life relationships.

Acknowledgement

The CALCE Consortium has served the electronics industry for more than 40 years, providing a knowledge and resource base for the development and sustainment of competitive electronics products and systems. CALCE members define research needs and direction and share in the findings. The author would like to thank several graduate research assistants who supported this study, including but not limited to Idowu Olajire Olatunji, Randall Silvestro, Jonathan Hower, and Louis Hardock.

Funding Data

This work has been sponsored by members of the CALCE Electronic Products and Systems Consortium.

Conflict of Interest

The corresponding author declares no conflicts of interest regarding this article.

Data Availability Statement

The data presented in this article are available from the corresponding author upon reasonable request.

Nomenclature

με	microstrain
g	gravitational acceleration, m/s^2
CABGA	ChipArray Ball Grid Array
CTBGA	ChipArray Thin Core Ball Grid Array
CTF	Cycles-to-Failure
CVBGA	Very Thin ChipArray Ball Grid Array
FEA	Finite Element Analysis
FFT	Fast Fourier Transform
FR4	Flame Retardant 4
LTS	Low-Temperature Solder
PBA	Printed Board Array
PB	Printed Board
QFN	Quad-Flat-No Lead
SG	Strain Gauge
EDS	Energy dispersive X-ray spectroscopy

A.2. Appendices

The Appendices contain supplementary data which are relevant to several discussions throughout this study.

A.2.1 Multiscale Finite Element Model to Estimate Flexural Strain Distribution

To approximate the strain responses at consistent locations across each test vehicle, a dynamic FE model of the PBA was developed. This model, denoted as the global model, was constructed to reproduce the dynamic response behavior of the test vehicle under harmonic excitation. To accurately estimate PBA strains, the global model must properly account for the local stiffening effects introduced by the surface mounted components, which influence the global bending response of the PBA [29]. These stiffening effects were estimated from a detailed local FE model, which was developed for the CABGA192 and QFN68 components.

In this study, the stiffening behavior of the CVBGA360 and CTBGA228 components was assumed to be comparable to that of the CABGA192. A half-symmetry representation of the CABGA192 local model can be seen in Figure 25. The parameters extracted from the local models, used for calibration of the global model, are the flexural rigidity and the neutral axis position under bending. A complete description of the global and local models, along with the full modeling methodology are provided in [19].

The FR4 material properties used in both the local and global models were taken from [23]. Material properties for the epoxy molding compound, silicon die, component substrate, die attach, and copper were obtained from the calceSARA© software package [30]. The elastic and inelastic material properties for SAC305 were based on values reported in the literature [31]. For simplicity, deformation of all tested solder materials was modeled using elastic-plastic stress-strain curves of SAC305 solder.

After calibrating the local stiffening effects, the stiffness of the global dynamic FE model was adjusted to match the PBAs fundamental frequency measured during sine-sweep testing. Damping was then tuned to reproduce the PBAs experimentally measured transfer function.

This calibrated global FE model was used to estimate flexural strain responses at the footprint of all the components. These estimated strain values were then used to construct the fatigue life plots presented in Section 2.3.4.

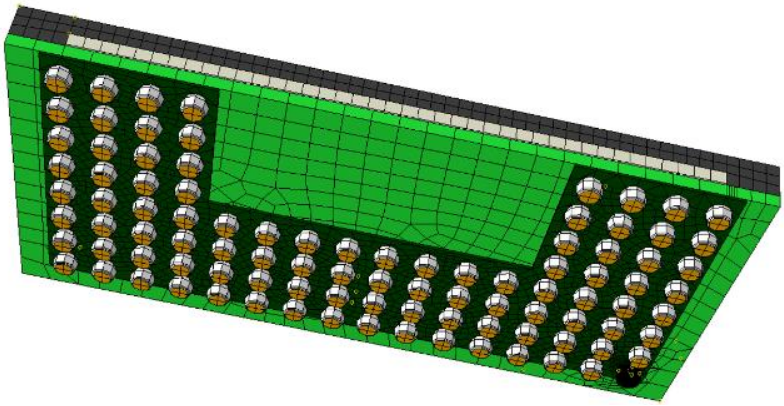

Figure 25. Local Half-Symmetry Model of CABGA192

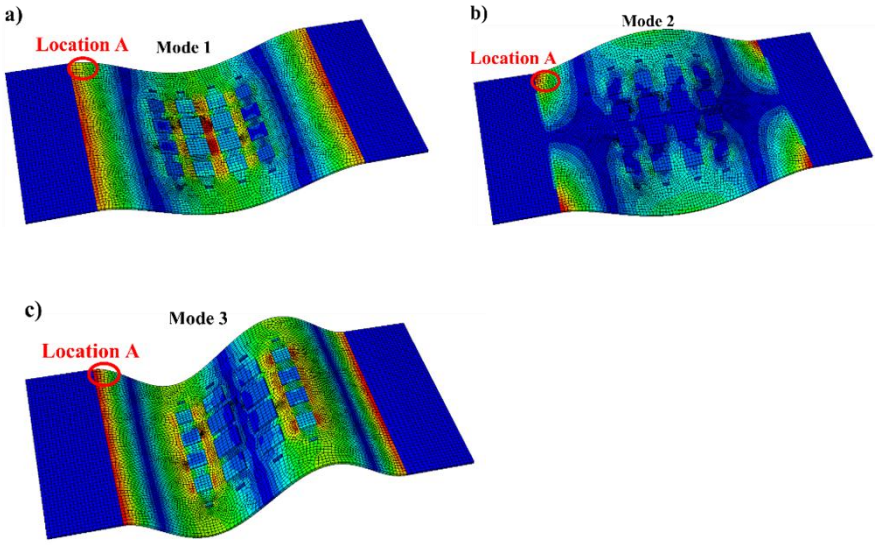

Figure 26(a)(b)(c). FE Estimation of First Three Mode Shapes

A.2.2 Nonlinear Analysis of the CFCF PBA

The transmissibility between the base excitation and the dynamic response of the PBA was observed to vary across different test specimens, due to inherent variability in the specimen mounting process and due to nonlinear deformation inherent in the CFCF fixturing scheme. This nonlinearity has manifested both in the transmissibility (see Figure 27) as well as in experimentally observed superharmonics, resulting in an anomalous Mode 3 response (discussed earlier in Section 2.3.2 and shown in Figures 28 and 29). As described by Porter and Brake [26], superharmonic resonances occur in nonlinear systems when the response contains frequency content at integer multiples of the excitation frequency. The cause for this nonlinear response is believed to be due to stress-stiffening caused by membrane strains at large deformation levels. More detailed analysis of this nonlinearity is presented in [19].

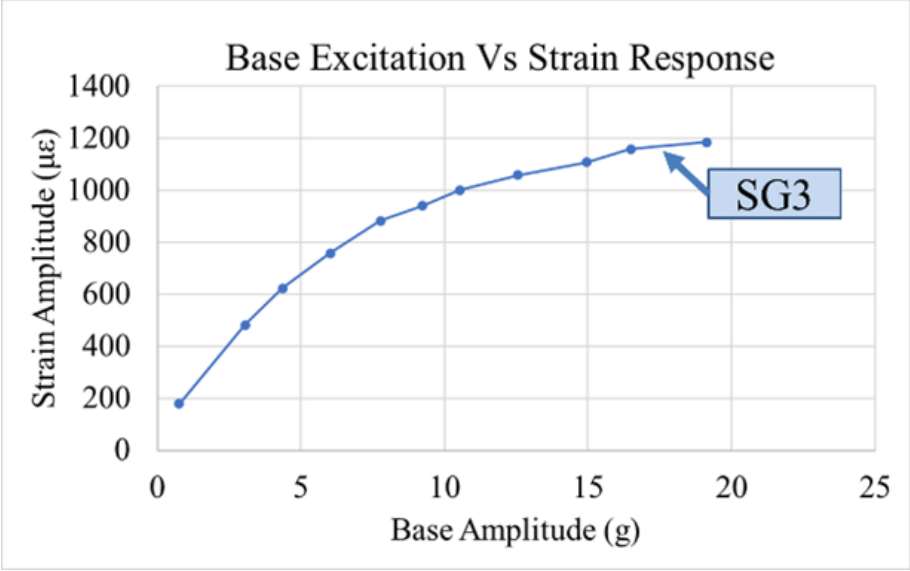

Figure 27. Base Excitation vs PB Strain Response showing nonlinear transmissibility

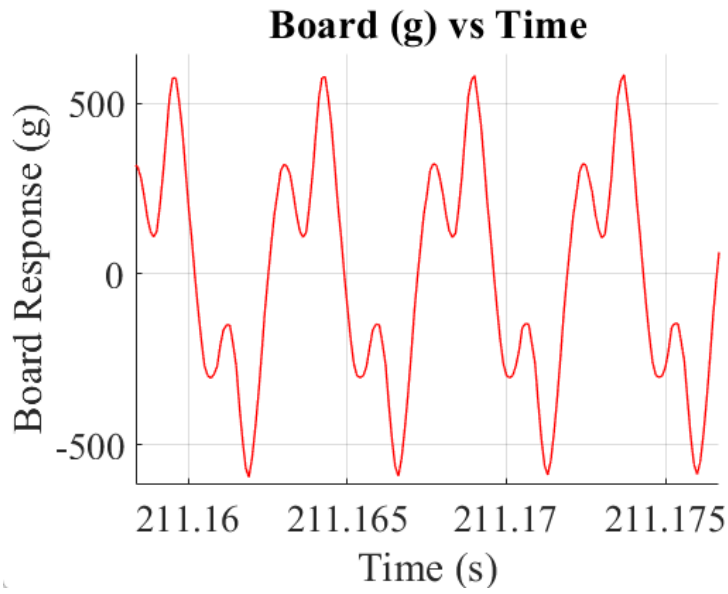

Figure 28. Time History of Board Response (g) during High Excitation

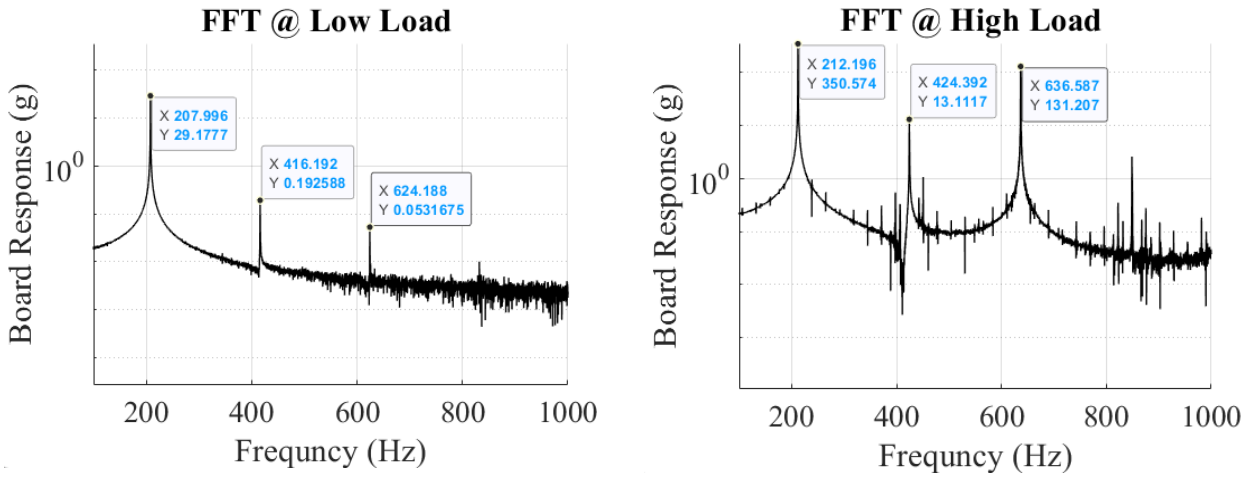

Figure 29. FFT of Board Response (g) under Low and High Excitation, showing Spurious Nonlinear Third Superharmonic Response Under Mode 1 excitation

The Fast Fourier Transform (FFT) plots (shown in Figure 29) reveal a spurious third superharmonic contribution that is nearly absent at low excitation loads, but grows

disproportionately under high excitation loads, indicative of a nonlinear response. Figure 30 confirms the progressive growth of the peak of the third superharmonic relative to that of the first harmonic (termed 3:1 for further discussion) on LTS3 #2 (overstress test). The response (Figure 30) remains approximately linear below 200 g of board response amplitude, where the 3:1 ratio stays below 5%, beyond which the nonlinear contribution grows rapidly as the board response increases. Purely linear responses would have produced no superharmonic content and the 3:1 ratio would have remained insignificant, regardless of the response amplitude. Previous studies have reported similar nonlinear trends, as reported by Yang et al. [32] and Che et al. [33].

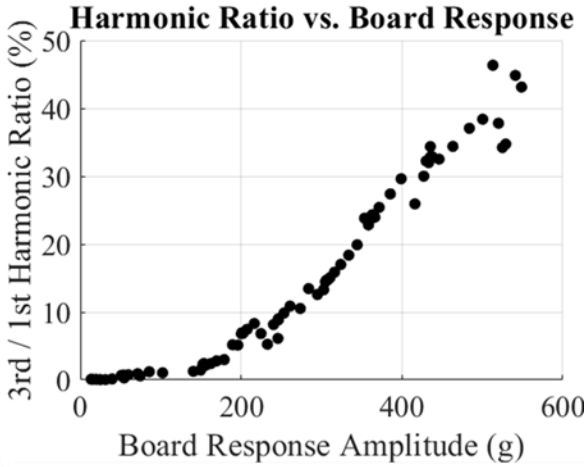

Figure 30. Board Response Amplitude as a Function of the Ratio of the 3:1 Superharmonics for LTS3 #2 (Overstress Test)

To investigate the variability in the superharmonic response across test specimens, two complementary analyses were performed using strain gauge data filtered around the first resonant frequency (~200 Hz) and the third superharmonic frequency (~600 Hz). Strain gauges SG2 and SG4 (see Figure 6) were used for this analysis since they lie at antinodes of the third mode shape (see Figure 26(c)). The first analysis (see Figure 31) computes the 3:1 ratio at SG4 for all test boards, revealing significant piece-to-piece variability in the severity of the

superharmonic response, with LTS2 #4 showing the least superharmonic content and LTS1 #2 showing the most. Figures 32(a)(b) illustrate the change in the 3:1 ratio as a function of the board response amplitude (g) for LTS2 #4 and LTS1 #2 during their fatigue life tests. LTS2 #4 does not reach a 10% ratio until approximately 210 g, while LTS1 #2 crosses 10% at just 75 g.

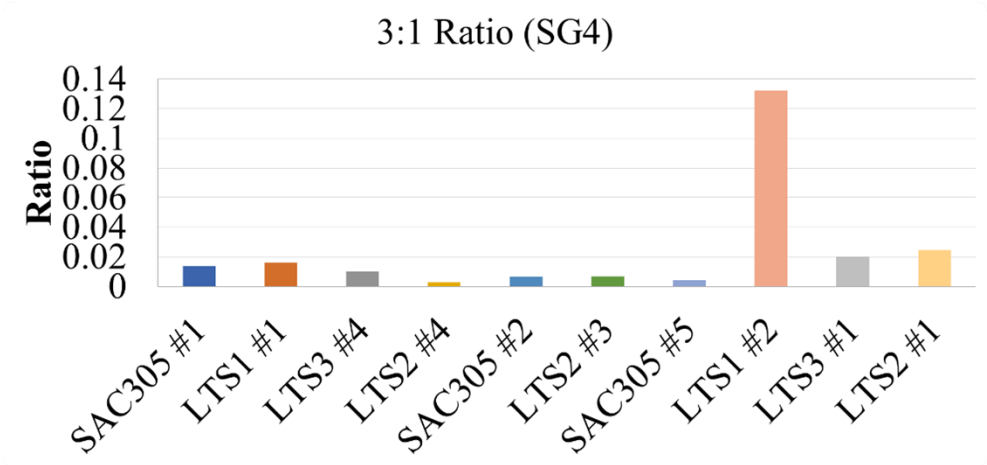

Figure 31. 3:1 Ratio of SG4, sorted by Base Excitation (smallest to largest)

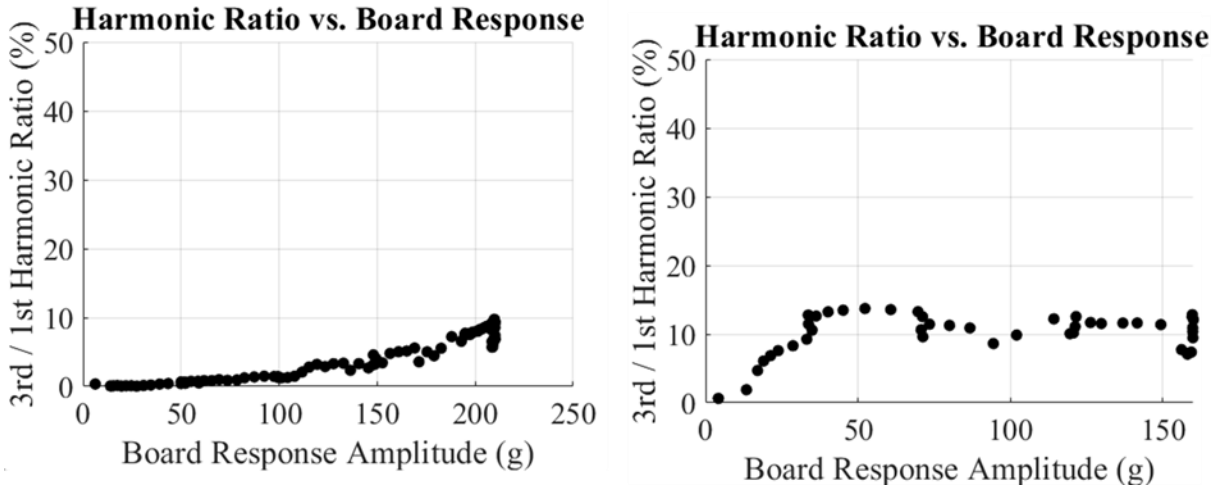

Figure 32(a)(b). Board Response Amplitude as a Function of the Ratio of the 3:1 Superharmonics for LTS2 #4 and LTS1 #2, respectively

The second analysis (Figure 33) identified the spatial phase difference between SG2 and SG4 filtered around ~600 Hz. Figure 34 complements this by showing representative filtered time

histories (from SAC305 #1) of SG2 and SG4 filtered at ~600 Hz and ~200 Hz respectively, highlighting when the two strain gauges are out of phase (Mode 3 response) and in phase (Mode 1 response). A phase difference of ±180° is consistent with the antisymmetric Mode 3 shape (third flexural mode), while a phase difference of 0° is consistent with the symmetric Mode 1 flexural response. Since none of the test boards exhibited a phase difference at either of these values, the results indicate that all test vehicles experienced a mixture of Mode 1 and Mode 3 participation, confirming that energy is leaking from Mode 1 into Mode 3 via the nonlinear superharmonic mechanism. These two analyses do not directly correlate because the phase shift characterizes the spatial shape of the third mode shape, while the 3:1 ratio semi-quantifies energy transfer, which depends on the strain gauges position relative to both the Mode 3 shape and the component footprint.

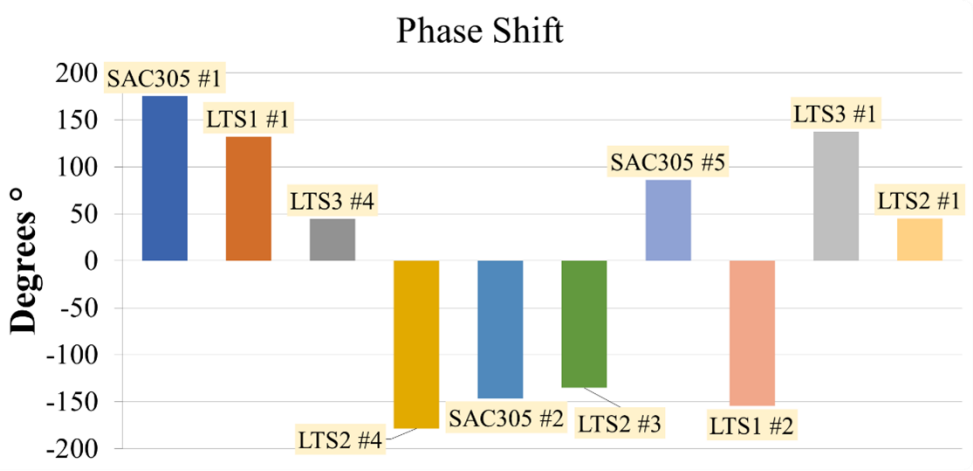

Figure 33. Phase Shift between SG2 and SG4, sorted by Base Excitation (smallest to largest)

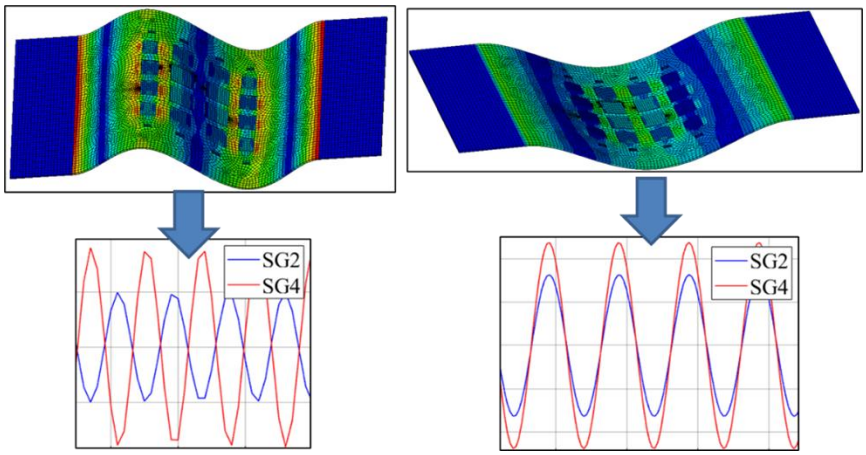

Figure 34. SG2 and SG4 Filtered Around ~600 Hz and ~200 Hz, respectively

When multiple modes are simultaneously activated, the strain experienced by the solder joints can significantly differ from what the single-mode analysis of Appendices A.1. predicts. Choi and Dasgupta [34] demonstrated that when multiple modes are activated, the fatigue damage accumulation rates are correlated with the modal participation of each contributing mode, indicating that the unexpected Mode 3 contribution in the present study likely introduced variability in the fatigue damage accumulation rates and hence in the measured CTF data.

References

[1] European Commission, Restriction of Hazardous Substances in Electrical and Electronic Equipment (RoHS) Directive, Environment – Waste and Recycling, European Commission, (accessed: Mar. 18, 2026), https://environment.ec.europa.eu/topics/waste-and-recycling/rohs-directive_en.

[2] S. Mokler, R. Aspandiar, K. Byrd, O. Chen, S. Walwadkar, K. K. Tang, M. Renavikar, and S. Sane, "The Application of Bi-Based Solders for Low Temperature Reflow to Reduce Cost While Improving SMT Yields in Client Computing Systems," in Proc. SMTA Int., Rosemont, IL, USA, Sep. 2026, https://doi.org/10.37665/smLWOND16110.

[3] H. Zhang, F. Mutuku, and H. Wang, "The Challenge of Lower Temperature Soldering for Large Ball-Grid Array (BGA) Board-Level Assembly Phase 1. Processing," J. Surf. Mount Technol., pp. 2–14, Jan. 2026, https://doi.org/10.37665/jqvy6470.

[4] T. B. Ratanawilai, B. Hunter, G. Subbarayan and D. Rose, "A study on the variation of effective CTE of printed circuit boards through a validated comparison between strain gages and Moire/spl acute/ interferometry," in IEEE Transactions on Components and Packaging Technologies, vol. 26, no. 4, pp. 712-718, Dec. 2003, https://doi.org/10.1109/TCAPT.2003.821685.

[5] J. W. Y. Kong, Jang-Kyo Kim and M. M. F. Yuen, "Warpage in plastic packages: effects of process conditions, geometry and materials," in IEEE Transactions on Electronics Packaging Manufacturing, vol. 26, no. 3, pp. 245-252, July 2003, https://doi.org/10.1109/TEPM.2003.820806.

[6] W. Shen, Z. Lei, K. Liang, G. Wu, T. Zeng and S. Liu, "Effect of Warpage on Solder Joint Fatigue Life by Influencing the Solder Joint Shape in BGA Packages," in IEEE Transactions on Components, Packaging and Manufacturing Technology, vol. 14, no. 4, pp. 611-618, April 2024, https://doi.org/10.1109/TCPMT.2024.3372520.

[7] N. Muthuram and S. Saravanan, "Fatigue life based study of Electronic Package Mounting Locations on Printed Circuit Boards Subjected to Random Vibration Loads", J. Electron. Test, vol. 40, pp. 761–776, (2024). https://doi.org/10.1007/s10836-024-06151-5.

[8] D. Yun Chen and M. Osterman, "Reliability of corner staked surface mount packages," 2016 IEEE Accelerated Stress Testing & Reliability Conference (ASTR), Pensacola Beach, FL, USA, 2016, pp. 1-6, https://doi.org/10.1109/ASTR.2016.7762272.

[9] T. An, F. Qin, B. Zhou, P. Chen, Y. Dai, H. Li, T. Tang, "Vibration lifetime estimation of PBGA solder joints using Steinberg model, Microelectronics Reliability", Microelectron. Reliab., vol. 102 (2019), p. 113474, 2019, https://doi.org/10.1016/j.microrel.2019.113474.

[10] Y. Zhou, M. Al-Bassyiouni and A. Dasgupta, "Harmonic and Random Vibration Fatigue life of SAC305 and Sn37Pb Solder Alloys," in IEEE Transactions on Components and Packaging Technologies, vol. 33, no. 2, pp. 319-328, June 2010, https://doi.org/10.1109/TCAPT.2009.2036834.

[11] B. M. Paquette, "Harmonic Vibration Testing of Electronic Components Attached to Printed Wiring Boards With SAC305 and Eutectic SnPb Solder", M.S. thesis, Dept. of Mech. Eng., University of Maryland, College Park, MD, USA, 2010, http://hdl.handle.net/1903/11101.

[12] J. B. Libot, L. Arnaud, O. Dalverny, J. Alexis, P. Milesi and F. Dulondel, "Mechanical fatigue assessment of SAC305 solder joints under harmonic vibrations," 2016 International Conference on Electronics Packaging (ICEP), Hokkaido, Japan, 2016, pp. 231-236, https://doi.org/10.1109/ICEP.2016.7486818.
[13] B. L. Brinkmeyer, “Thermal Characterization and Vibration of Solder Alloys, M.S. thesis, Dept. of Metallurgical Eng., Missouri University of Science and Technology”, Rolla, MO, USA, 2008, https://scholarsmine.mst.edu/masters_theses/4473/.
[14] Osterman, M., & Mendelsohn, A. “Thermal Cycle Fatigue Life of Low-Temperature Solders”. Proceedings of the SMTA International Conference (SMTAI), Surface Mount Technology Association, original publication year as in proceedings. CALCE, University of Maryland, College Park, MD, USA. https://doi.org/10.37665/smXHJGJ19902.
[15] O. H. Chen, A. Molina, R. Aspandiar, K. Byrd, S. Mokler, and K. K. Tang, "Mechanical shock and drop reliability evaluation of the BGA solder joint stack-ups formed by reflow soldering SAC solder balls BGAs with BiSnAg and resin reinforced BiSn-based solder pastes," Proc. SMTA Int., pp. 215–222, Sep. 2015, https://doi.org/10.37665/smJNMEA29283.
[16] H. Fu et al., "iNEMI project on process development of BiSn-based low temperature solder pastes: Part III: Mechanical shock tests on POP BGA assemblies," 2018 International Conference on Electronics Packaging and iMAPS All Asia Conference (ICEP-IAAC), Mie, Japan, 2018, pp. 13-18, https://doi.org/10.23919/ICEP.2018.8374660.
[17] M. Song, T. S. Lui, L. H. Chen et al., "Resonant vibration behavior of lead-free solders," J. Electron. Mater., vol. 32, pp. 1501–1508, 2003, https://doi.org/10.1007/s11664-003-0121-3.
[18] Derr-Haverlach, G. (2025). Narrow band random vibration reliability of a doped near eutectic tin-bismuth-based alloy with a large fine-pitch ball grid array device (Order No. 31994900). Available from ProQuest Dissertations & Theses Global. (3195958935). Retrieved from https://www.proquest.com/dissertations-theses/narrow-band-random-vibration-reliability-doped/docview/3195958935/se-2.
[19] Martin, J. C., Bharamgonda, A. A., Osterman, M., and Dasgupta, A., submitted, “Finite Element Modeling of Fatigue Life in Low-Temperature Solder Interconnects Under Harmonic Vibration,” ASME Journal, Apr. 2026, manuscript under review.
[20] S. Sahasrabudhe et al., “Low Temperature Solder – A Breakthrough Technology for Surface Mounted Devices,” 2018 IEEE 68th Electronic Components and Technology Conference (ECTC), San Diego, CA, USA, 2018, pp. 1455-1464, https://doi.org/10.1109/ECTC.2018.00222.
[21] Q. Su, J. Pitarresi, M. Gharaibeh, A. Stewart, G. Joshi and M. Anselm, “Accelerated vibration reliability testing of electronic assemblies using sine dwell with resonance tracking,” 2014 IEEE 64th Electronic Components and Technology Conference (ECTC), Orlando, FL, USA, 2014, pp. 119-125, https://doi.org/10.1109/ECTC.2014.6897276.
[22] “Performance Test Methods and Qualification Requirements for Surface Mount Solder Attachments,” IPC-9701A, 2006, https://www.electronics.org/TOC/IPC-9701A.pdf.
[23] E. Lin, “Effect of Isothermal Aging on SAC305 Harmonic Vibration Fatigue life”, M.S. Thesis, Department of Mechanical Engineering, University of Maryland, College Park, MD, USA, 2016, http://hdl.handle.net/1903/18420.

[24] Y. Zhang, Z. Cai, J. C. Suhling, P. Lall, and M. J. Bozack, "The effects of aging temperature on SAC solder joint material behavior and reliability," 2008 58th Electronic Components and Technology Conference, Lake Buena Vista, FL, 2008, pp. 99-112, https://doi.org/10.1109/ECTC.2008.4549956.
[25] Kim, J.Y., Yoon, E.J., Chang, S.J. et al. A study on the determination of optimal reference spectrum for random vibration control in environmental vibration test. KSME Journal 10, 246–254 (1996). https://doi.org/10.1007/BF02953663.
[26] J. H. Porter and M. R. W. Brake, "Tracking superharmonic resonances for nonlinear vibration of conservative and hysteretic single degree of freedom systems", Mechanical Systems and Signal Processing, Volume 215, 2024, 111410, ISSN 0888-3270, https://doi.org/10.1016/j.ymssp.2024.111410.
[27] A. H. Nayfeh and D. T. Mook, Nonlinear Oscillations. New York, NY, USA: Wiley-VCH, 1979, sec. 4.1.3, pp. 175–178.
[28] Y. Zhou, M. Al-Bassyiouni, and A. Dasgupta, "Vibration fatigue life assessment of Sn3.0Ag0.5Cu and Sn37Pb solders under harmonic excitation," ASME J. Electron. Packag., vol. 131, no. 1, p. 011016, Mar. 2009, https://doi.org/10.1115/1.3078195.
[29] I. Olatunji, A. Deshpande, M. Bascolo, A. Dasgupta, U. Becker and G. Jokai, "Fatigue life of Copper Traces in Ball Grid Array (BGA) Assemblies under Sequential Harmonic Vibration and Temperature Cycling," Proceedings of 23rd International Conference on Thermal, Mechanical and Multi-Physics Simulation and Experiments in Microelectronics and Microsystems (EuroSimE), pp. 1-5, St Julian, Malta, 2022, https://doi.org/10.1109/EuroSimE54907.2022.9758863.
[30] CALCE SARA: Shock and Accelerated Reliability Assessment Tool, CALCE, University of Maryland, College Park, MD, USA. [Online]. Available: https://calce.umd.edu (accessed: Feb. 4, 2025).
[31] H. Ma, J. C. Suhling, Y. Zhang, P. Lall and M. J. Bozack, "The Influence of Elevated Temperature Aging on Reliability of Lead Free Solder Joints," Proceedings of 57th Electronic Components and Technology Conference, pp. 653-668, Sparks, NV, USA, 2007, https://doi.org/10.1109/ECTC.2007.373867.
[32] Q. J. Yang, Z. P. Wang, G. H. Lim, J. H. L. Pang, F. F. Yap and R. M. Lin, "Reliability of PBGA assemblies under out-of-plane vibration excitations," in IEEE Transactions on Components and Packaging Technologies, vol. 25, no. 2, pp. 293-300, June 2002, https://doi.org/10.1109/TCAPT.2002.1010020.
[33] F. X. Che and J. H. L. Pang, "Vibration reliability test and finite element analysis for flip chip solder joints," Microelectron. Reliab., vol. 49, no. 7, pp. 754–760, 2009, https://doi.org/10.1016/j.microrel.2009.03.022.
[34] C. Choi and A. Dasgupta, "Fatigue of solder interconnects in microelectronic assemblies under random vibration," Procedia Eng., vol. 74, pp. 165–169, 2014, https://doi.org/10.1016/j.proeng.2014.06.243.

CHAPTER 3: FINITE ELEMENT MODELING

ABSTRACT – This paper presents multiscale finite element (FE) modeling for the development of vibration fatigue life model constants for three selected low-temperature solders (LTSs). The fatigue performance is compared to SAC305 assemblies for benchmarking purposes. The FE modeling in this study addresses ball grid array and bottom terminated components. The solder interconnects for these two components have different aspect ratios and difference stress states. A global-local calibrated FE modeling approach is used for estimating strain histories within the solder interconnects, since the strain is not directly monitored during fatigue experiments. A global model of the printed board assembly (PBA) under test is created using a reduced-order linear FE model calibrated by experiments. This global model is used to infer the dynamic response of the PBA at the component positions. This is followed by detailed nonlinear sub-modeling of the components of interest. The detailed sub-models provide estimates of cyclic solder strain for the solder interconnects of interest. These estimated cyclic strains are used, along with experimentally measured cycles-to-failure, to obtain fatigue strain-life (SN) model constants. The proposed methodology provides a generic methodology for vibration fatigue life modeling.

3.1 Introduction

Low-temperature solders (LTS) have become alternatives to SAC305 for applications where reduced solder reflow temperatures are required to reduce electronic assembly defects caused by CTE mismatch induced warpage. However, the high-cycle fatigue (HCF) behavior of LTS under vibration loading remains insufficiently characterized. HCF model constants are necessary inputs

for physics-based life prediction models, which in turn, form the basis for design decisions such as component placement and mechanical enforcement, such as edge bonding, corner staking, and applying an underfill [1,2].

This paper presents a multi-scale finite element analysis (FEA) methodology to estimate strain in solder interconnects used in creating strain-based fatigue life model constants from vibration experiments [3]. To create fatigue life curves, time-to-failure (TTF) must be coupled with strain level at the failure site. Ideally, this is done through physical metrology, using strain measurement instrumentation and resistance monitoring. However, for solder interconnects formed between packaged electronic components and a printed board (PB), the ability to measure strain in the solder is infeasible. As a result, strain is generally measured on the PB near the component of interest. In this situation, a calibrated finite element (FE) model offers a reasonable alternative approach to estimate strain histories at the failure site.

Several FEA-based strategies have been proposed in literature for the purpose of estimating solder strains during physical testing [4-16]. These approaches primarily differ in the model geometry and in how solder joints are represented. In the context of vibration, FE modeling falls into three approaches. The first is the direct model, which includes the PB, the component, and solder joint of interest. The second is the submodeling approach, where a coarse representative global model is used to supply a nodal displacement field to a detailed local model; this methodology is used in the present study. The third is what literature calls the global-local-beam approach, which uses an equivalent 2-node beam to represent the solder, which drives a local solid solder model.

The direct global model method uses one global model, which contains the detailed component geometry. Variations of this method exist in the literature. In one common version,

only the component(s) of interest are modeled with the full component geometry, while other components are represented using uniform equivalent layers [4,5]. In another version, all components and their associated geometry are explicitly modeled in detail within the same global model [6,7]. Of the three most common methods, this is the easiest to implement due to the exclusion of local models. However, this method scales poorly when modeling large assemblies, often resulting in high computational costs due to the large number of elements.

The submodeling approach, commonly referred to as multiscale global/local submodeling, is the most widely used method, and is used in this study. This method generally consists of two finite element models: a reduced-order global model (GM) with limited details and a more detailed local model (LM). In the GM, components are typically represented using simplified geometries, such as shell elements [8] or layered representations [9]. Two variations of the LM are commonly reported in the literature. In the first, the LM consists of a symmetric half or quarter model of the component with fully detailed solder joint geometry [8]. In the second, the LM consists of a cut column cell surrounding the solder joint with the highest cyclic strain range (typically the corner joint), referred to as the critical solder joint in this study [10]. In both cases, the GM provides a 3D nodal displacement field, which is interpolated and applied as boundary conditions to the LM. This method is widely adopted in the literature and is considered to produce satisfactory results. The transfer of the displacement fields from the GM to the LM is often done with automated submodeling capabilities available in commercial FEA codes, ABAQUS CAE is used in this study. However, this approach is more complex to implement than the direct method, as it requires the use of models (discussed in Section 3.3).

The last family of modeling methods is known as the global-local-beam (GLB) approach. It shares a similar framework to the submodeling approach, but the primary difference is how

solder joints are represented in the GM and what geometries are modeled within the LM. In some variations, a LM is not used and solder strains are extracted directly from the GM [11]. In the GLB approach, solder joints in the GM are replaced with a 2-node beam with an equivalent stiffness. This simplification greatly reduces the number of elements and is considered to be computationally inexpensive. Similar to submodeling, a nodal displacement field is calculated and transferred to a LM. The LM in the GLB approach typically consists of only the critical solder joint. GLB is reasonable only when solder deformation is primarily elastic, due to solder joints being represented as elastic beam elements [12,13]. Otherwise, alternative methods are suggested.

In all cases, it is important to assess the validity of the FE model to ensure that the model is properly calibrated and suitable for predictive analysis. In the literature, it is common for studies to perform validation through modal analysis, where natural frequencies obtained from the FE model are compared against experimentally measured natural frequencies [4,9,12]. However, this method of validation is limited, matching natural frequencies only validates the global stiffness and mass distributions, which may result in inaccurate solder strain predictions. It does not ensure that the stiffening effects introduced by the components, the resulting neutral surface shift, or the damping parameters are accurately being captured.

Existing FEA approaches are often validated through a limited number of physical parameters, such as natural frequency matching, this alone is insufficient to capture accurate solder strain predictions. This paper addresses this gap by expanding upon the global/local submodeling method, previously proposed in [8,14-16], with a more rigorously validated model calibration procedure to generate strain-based fatigue life model constants for LTS alloys which have not yet been characterized under harmonic vibration loading.

3.2 Summary of Experimental Results

This section provides a summary of the test vehicle and tests that are the subject of the FE modeling presented in this study.

The test vehicle (Figure 1) consisted of an FR4 composite PBA with dimensions of 228 x 114 x 1.44 mm. Each test vehicle consists of 24 surface-mounted components: four CABGA192, four CVBGA360, four CTBGA228, four QFN68, and eight surface-mounted resistors (SMR1206). All BGAs contain SAC305 solder balls. The SMR components are not considered for analysis in the present study. PBA and component designs consist of complementary daisy-chain networks, to enable real-time monitoring of the health of the interconnects in each component. A picture of a mounted test board is provided in Figure 2.

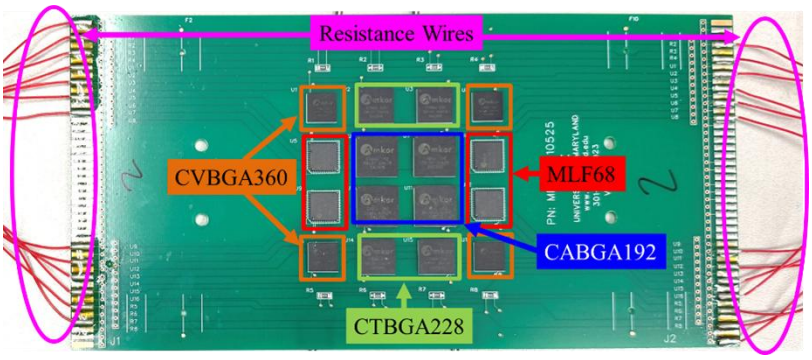

Figure 1. Assembled Test Vehicle

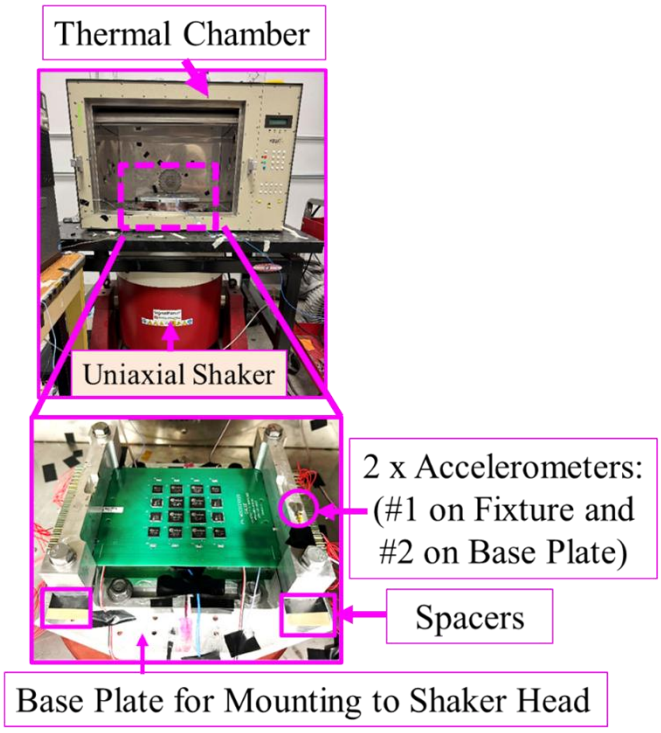

Figure 2. Mounted Test Vehicle

Test vehicles were assembled using three different LTS pastes, designated as LTS1, LTS2, and LTS3. In addition, reference specimens assembled with SAC305 paste were also tested for benchmarking purposes. Table 1 presents details about LTS composition, melting temperature, and isothermal aging conditions.

Table 1. Tested Solder Alloy Composition

Source	Alloy/Composition	Melting Temperature (°C)	Aging Temperature (°C)
SAC305	SAC305	217	125
LTS1	Sn57.3Bi0.5Ag	137-142	62
LTS2	Sn56.2Bi1.4Sb	140-145	62
LTS3	Sn48.2Bi0.5Ag0.2Sb	145-150	62

The vibration test fixture employed two rigid clamps mounted to the shaker base plate of an electro-dynamic (ED) shaker, resulting in a clamped-free-clamped-free (CFCF) boundary condition on the test vehicle, with a nominal unsupported span of 152 mm.

Four strain gauges (SG) and two accelerometers were used to capture the dynamic response of the PBA. Sensor data will be used in this paper to develop a calibrated finite element (FE) model. The placement of the strain gages and accelerometers are depicted in Figure 3. All sensors were placed in identical locations across all test vehicles on the side opposite the components. Under test, the electrical resistance of solder interconnects for individual components were monitored through daisy chains created by the component and board connections. Failure was defined in accordance with IPC-9701, which is a 20% increase of initial resistance over 5 consecutive scans [17].

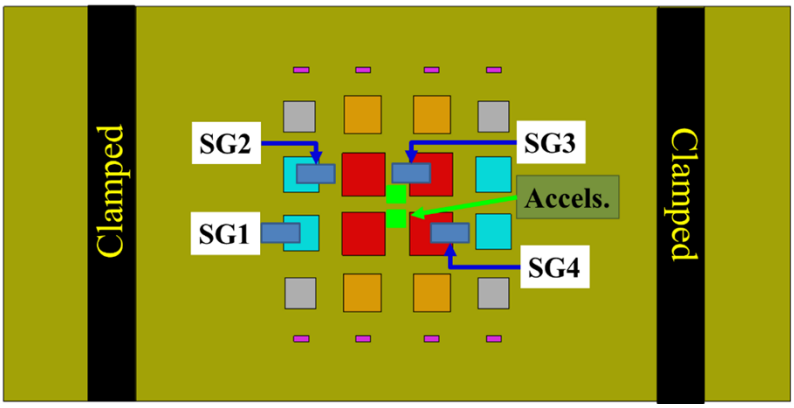

Figure 3. Approximate Sensor Location and Nomenclature on Test Vehicle

Prior to testing, all test boards were isothermally aged for 100 hours at 0.8 homologous temperature of the tested solder. The aging condition was chosen to allow microstructural evolution and intermetallic compound (IMC) growth to approach a more stable state across all specimens, thereby reducing variability between boards at the start of testing [17-19]. The aging

temperatures are presented in Table 1. Prior to fatigue life testing, a sine-sweep test was conducted to identify the test vehicle's first natural frequency. Each test vehicle exhibited a first natural frequency of approximately 200 Hz, a summary of the first resonant frequencies for each PBA can be found in Table 2 The load level was defined, then the fatigue life tests were conducted. The PBA strain and acceleration response, during fatigue life testing, can be found in Table 3. Each fatigue life test was conducted near the test vehicle's unique natural frequency, using resonance-control from an accelerometer near the PBA center.

Table 2. Summary of each Test Vehicles' Fundamental Frequency

Test Vehicle ID	Fundamental Frequency (Hz)
SAC305 #1	205
SAC305 #2	204
SAC305 #5	201
LTS1 #1	205
LTS1 #2	193
LTS2 #1	208
LTS2 #3	210
LTS2 #4	208
LTS3 #1	208
LTS3 #4	207

Table 3. Summary of each Test Vehicles' Base Excitation, Board Response, and SG3 Response. Board (g) and SG3 (με) response show variability of ±79 g and ±145 με, respectively, at 90% confidence.

Test Vehicle ID	Nominal Base Excitation (g)	Nominal Board Response (g)	Nominal SG3 (με)
SAC305 #1	1.91	120	489
SAC305 #2	3.25	190	608
SAC305 #5	3.71	195	645
LTS1 #1	2.5	139	463
LTS1 #2	4.46	182	722
LTS2 #1	9.05	400	925
LTS2 #3	3.6	198	646
LTS2 #4	3.1	200	558
LTS3 #1	8.22	324	1023
LTS3 #4	2.93	161	575

The PBA strain amplitude was estimated from the calibrated global model (details presented in Section 3.3.3 and 3.3.4) and was plotted against cycles-to-failure (CTF) for each component to assess the fatigue life performance of each interconnect [3]. In the calibrated global model, edge-centered virtual strain gauges were placed at the edges of the components' footprint, as illustrated in Figure 5. Results from the fatigue life tests revealed that LTS1 and LTS3 generally performed the best. All LTS interconnects outperformed SAC305. Tables 4 and 5 summarize the results from the fatigue life tests for the CABGA192 and QFN68 components. For each test board, the CTF values of the four QFN68 components and the four CABGA192 components were averaged separately, yielding one mean CTF value per component type per board.

Table 4. Fatigue Life Test Results for QFN68 from Prior Work [3]

QFN68

Board ID	AVG CTF	Strain Amplitude (με)
SAC305 #5	8.70E+04	547
SAC305 #2	1.49E+05	590
SAC305 #1	1.91E+06	369
LTS1 #2	1.99E+05	745
LTS1 #1	1.19E+06	447
LTS2 #1	5.58E+04	771
LTS2 #3	1.25E+05	688
LTS2 #4	1.84E+05	606
LTS3 #1	7.96E+04	779
LTS3 #4	9.23E+05	529

Table 5. Fatigue Life Test Results for QFN68 from Prior Work [3]

CABGA192

Board ID	AVG CTF	Strain Amplitude (με)
SAC305 #5	9.21E+04	547
SAC305 #2	3.07E+05	590
SAC305 #1	1.64E+07	369
LTS1 #2	5.47E+05	745
LTS1 #1	1.91E+07	447
LTS2 #1	3.63E+04	771
LTS2 #3	5.15E+04	688
LTS2 #4	2.21E+05	606
LTS3 #1	5.99E+04	779
LTS3 #4	1.97E+06	529

3.3 Finite Element Modeling

Finite element modeling is required to estimate the local PB strains used to build the fatigue life comparison plots and to extract solder strains within the critical region of the joint, ultimately to extract solder fatigue life model constants. The critical regions are defined in Section 3.4.1. Section 3.3 discusses how those models were built, assumptions made, and how these models aid

in obtaining the parameters used for analysis. The components modeled here include one of the tested BGAs (CABGA192) and one of the QFN68. As discussed earlier, this choice was motivated by the need to explore the effect of the interconnect geometry (different aspect ratios) on the stress state and on the resulting fatigue damage accumulation rates.

3.3.1 Global/Local Sub-modeling Approach

A multiscale global/local sub-modeling approach was used to address two limitations of physical strain measurement: (i) strain gauges cannot be placed at perfectly consistent locations across all test vehicles, introducing variability in the measured PB strain at component footprints; and (ii) solder-level strains cannot be directly measured using physical sensors due to size and access limitations.

In this study, the global model (GM) refers to a reduced-order model of the entire PBA populated with surface-mounted packages, as seen in Figures 4 and 7. The local model (LM) consists of a detailed symmetric half or quarter model representation of the CABGA192 and QFN68 components, their solder interconnects, and a section of the PB extending to the midpoint between the component of interest and the nearest component. A linear elastic version of these local models was used for calibration of the GM. A nonlinear version of the LM was used to estimate the strain histories on the PBA and in the critical solder joints, as discussed later in this sub-section.

The GM of the PBA was developed and calibrated to reproduce the same dynamic response observed during physical vibration testing. Once a fully calibrated GM has been developed,

strain responses were estimated at locations of interest on the PBA and the resulting PB displacements were transferred to a local half model for solder strain estimation.

As discussed above, a detailed local half model (LHM) was developed to estimate the strain response at component footprint locations on the PBA, and also at critical locations in the corner solder joints. Critical locations were defined as regions where solder cracking was observed during failure analysis, through destructive cross-sectioning [3]. Solder strain estimation was accomplished by transferring the nodal displacement fields, calculated in the GM, to the LHM to reproduce the PB strains observed during test. A quasi-static non-linear solver was used for the LHM solder strain analysis. It is acknowledged that a quasi-static solver does not capture inertial contributions of the component mass to the solder joint stress state. However, PB flexure is expected to be the primary loading mechanism, with inertial forces at the joint level being small in comparison. This assumption was validated through an analytical peel stress estimation for the QFN68 interconnects, which are more susceptible to peel loading than the CABGA192 joints and is discussed further in Section 3.4.4.

3.3.2 Modeling of Materials

The mechanical properties of each material can be found in Tables 6-8. Because full nonlinear mechanical properties for the LTSs are unavailable, SAC305 properties were adopted for all solder joints in each model, following similar practice in the literature [20].

3.3.3 Global Model (GM)

The board assembly was modeled using an FR4 substrate with surface partitions representing the solder array footprints and discrete instances for each of the 24 components, this is illustrated

in Figure 4. Tie constraints were used to constrain the packages to the surface of the FR4. Boundary conditions were defined using surface and cell partitions. The clamped edges were modeled by restricting all displacements and rotations. The FR4 and components were modeled using orthotropic 8-node continuum shell elements with reduced integration.

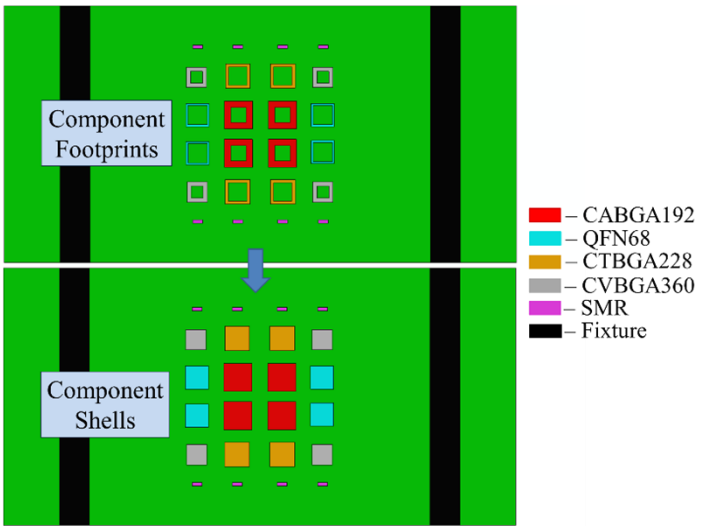

Figure 4. FEM of the GM PB

Two separate GM variations were created, each for a different purpose. The first is referenced as the edge-centered model, where virtual strain gauges are being modeled and positioned mid-way and centered underneath each component and are referred to as edge-centered virtual strain gauges. This model is not representative of the physical strain gauges used during test. This model was used to develop a method to estimate the PB strain response at consistent locations across each test vehicle, these strain responses were used to develop the fatigue life plots. Figure 5 illustrates this edge-centered model and the respective edge-centered virtual strain gauges. The second variation also contains virtual strain gauges; however, these virtual strain gauges are positioned in the same location as the physical strain gauges used on each test vehicle during the vibration experiments and are referred to as representative virtual

strain gauges. This model is referenced as the representative GM and is used for GM calibration, this model can be seen in Figure 6.

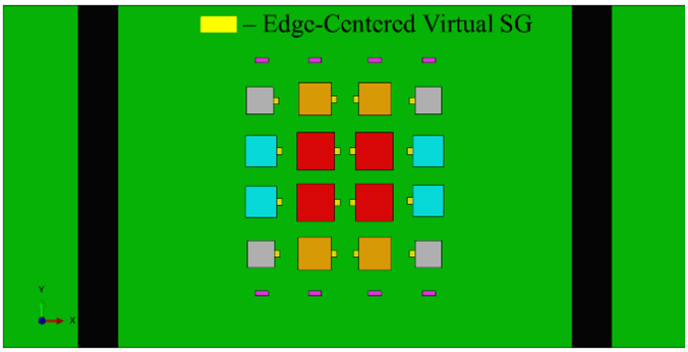

Figure 5. Edge-Centered Virtual Strain Gauge on Global Model

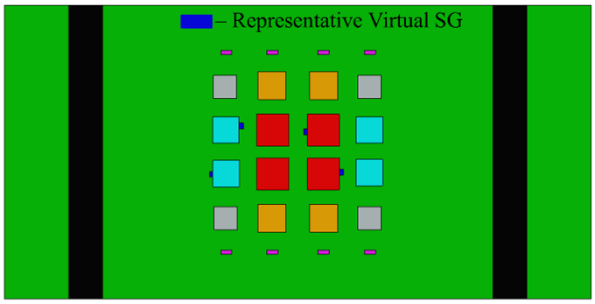

Figure 6. Representative Virtual Strain Gauge on Global Model

A linear approach (based on modal-superposition) was used, allowing for a relatively fine mesh throughout the PBA. A swept mesh was applied over the majority of the PBA for computational efficiency and ease of implementation. Local mesh refinement was introduced around the representative and edge-centered virtual strain gauges to ensure accurate strain predictions, a mesh density of 5 x 8 elements was used for the each of these types virtual strain gauges. A depiction of the GM mesh can be seen in Figure 7. The GM exclusively contains 8-noded quadrilateral continuum shell elements with reduced integration. All continuum shell element materials contain one element through the thickness. Continuum shells elements were

adopted over conventional shell elements based on their ability to capture strain variation through the thickness and reduce the total number of elements needed, therefore decreasing computational cost. Shell elements are appropriate for these layers, since the primary deformation is caused by bending. The GM contains a total of 18967 elements.

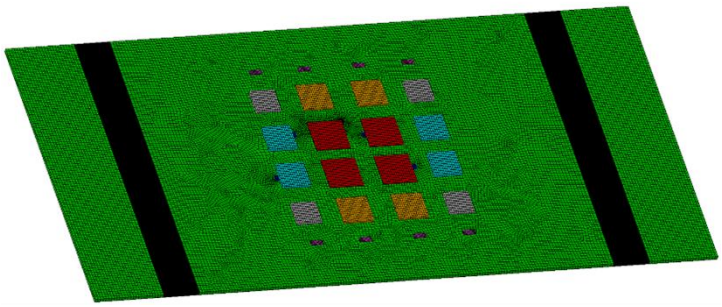

Figure 7. Mesh Density of GM

3.3.4 Global Model (GM) Calibration

The calibration process requires the satisfying the following three conditions:

a. The stiffening effect of the components must be correctly captured by identifying and matching: (i) the shift of the neutral surface (under the component footprint) and (ii) stiffening factor given by the curvature ratio (under the component footprint) between the bare PB and the populated PBA.

b. Once this relative stiffness factor is established, the experimentally measured natural frequency must be reproduced within the FE GM. This is done by uniformly scaling the stiffness of the entire system (while preserving the calibrated stiffening effect), until the measured natural frequency is duplicated in the FE GM.

c. Damping parameters must be adjusted to reproduce the experientially measured strain response at the locations of representative virtual strain gauges.

3.3.4.1 Stiffening Effect due to Components

The surface mounted components, on the PB, introduce a localized flexural stiffening effect that shifts the neutral surface away from the midplane of the PB towards the component. Accurately capturing this effect within the GM, via GM calibration, requires the characterization of two metrics: the neutral surface location and the stiffing factor. The following subsections describe the methodology used to extract these metrics from local quarter-symmetry models (LQMs) and replicate them within the GM. Details regarding the LQM mesh and element selection can be found in Section 3.3.5.

3.3.4.1.1 Neutral Surface Calibration

The flexural stiffening, due to the surface mount components, results in shifting of the neutral surface from the PB midplane towards the component (under the footprint of the component) in single-sided assemblies. This shift of the neutral surface is estimated using the LM and replicated within the GM under the footprint of each component. This involves the use of two additional models: a LQM of the QFN68 component as well as the CABGA192 component. These LQMs are limited to linear elastic modeling and their purpose is to identify the neutral surface shift associated with each component type. Since the detailed finite element LQM was limited to the CABGA192 and QFN68 in this study, the stiffening effect (*i.e.,* the neutral surface location) for all the other BGA style components was approximated in the GM to be similar to that obtained from the LQM of the CABGA192, while the stiffening effect of the surface-mounted resistors (SMRs) was approximated to be similar to that found in the QFN68 LQM.

To locate the neutral surface, a simple uniaxial pure-bending moment was applied on the x-face of the of the PBA in LQM, an illustrative example can be observed in Figure 8. The

boundary conditions were defined to enforce component symmetry and to suppress ridged body degrees of freedom, while allowing for bending deformation. The neutral surface was identified, by comparing the volume-averaged surface strains, in the xx direction, at the top and bottom surfaces of the PB under the component footprint. An illustration of the shift in the neutral surface can be seen in Figure 9 for the QFN68 assembly.

3.3.4.1.2 Stiffening Factor

The averaged surface-strains and neutral surface location was used to estimate the curvature, K (under the component footprint), as shown in Equation (1). The LQM was repeated for a bare PB and a stiffening factor, SF, is defined by the ratio of the curvature between the bare PB and populated PBA, as depicted by Equation (2).

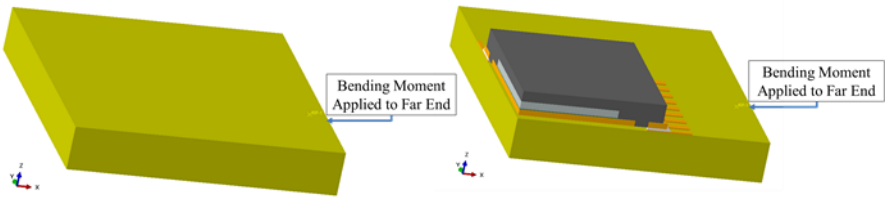

Figure 8. Local Quarter-Symmetry Model (LQM) of QFN68, using Linear FE Analysis

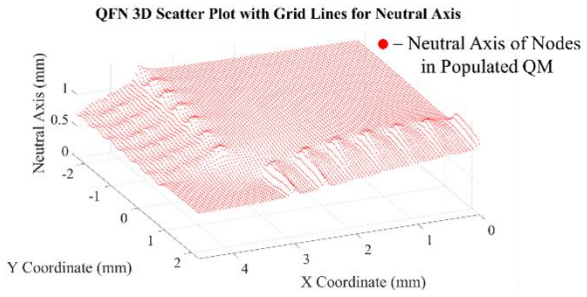

Figure 9. Neutral Surface Shift Distribution Across the Entire Package Footprint for a QFN68 assembly

$$K = \frac{Strain}{Neutral\ Axis\ Height\ (mm)} \quad (1)$$

$$SF = \frac{K_{bare\ PWB}}{K_{component}} \quad (2)$$

Two parameters in the GM can be adjusted to match these two metrics of component stiffening: (i) the effective component height (see Figure 10), and (ii) stiffness ratio between the shell representations of the component and the PB. The process described earlier for estimating the neutral surface location and stiffening ratio in the LQM is repeated here for the GM. Once the stiffening effect (neutral surface location and stiffness factor) is matched, this step is complete. The calibrated stiffening effect is preserved; unchanged through the remaining calibration steps. Table 9 presents the neutral surface heights in the LQM and the GM.

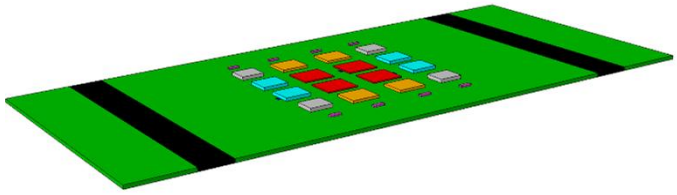

Figure 10. Component Shell Heights in Global Model

Table 9. Neutral Surface Position in LQM and GM

Component	Neutral Surface (mm) in LQM	Neutral Surface (mm) in GM	% Difference
CABGA192	0.93	0.93	0
QFN68	0.96	0.95	1.04

3.3.4.2 Calibration of Resonant Frequencies

After the stiffening effect is successfully reproduced in the GM, the natural frequencies are matched to those measured experimentally. The measured resonant frequencies can be found in Table 2. To ensure that the stiffening effect is unaltered, the ratio between the stiffnesses of the PB shell and component shell is held constant. By uniformly scaling the stiffness of the PB shell and the component shell, without changing their ratio, the correct natural frequencies are matched without altering the relative stiffening effects. A comparison of the measured natural frequencies and those predicted by the FE GM simulation can be found in Table 10. The mode shapes can be found in Figure 26(a)(b)(c) of [3].

Table 10. Comparison Between Measured and Calculated Resonant Frequencies

Mode	Measured Natural Frequency (Hz)	FEM Natural Frequency (Hz)	% Difference
1	205	206	0.49
2	273	271	0.74
3	590	582	1.37

3.3.4.3 Calibration of the Dynamic Strain and Acceleration Responses

The next step in the GM calibration process is reproducing the measured strain and board acceleration responses. Strain gauges installed on the physical PB were explicitly modeled within the GM and are referenced as representative virtual strain gauges. The strain response estimated at these representative strain gauge locations were compared to the experimental measurements.

A modal dynamic solver was used since it allows for a time-based simulation. The base excitation, measured during test, was used as the input acceleration-based load. The duration of the analysis was adequately extended to ensure that any transient solution decays sufficiently to ensure a steady state response. As shown in Figure 11, 0.4 seconds was sufficient for the transient response to decay. To match the strain and acceleration responses, the damping factor was adjusted until the desired response amplitudes were achieved. Table 11 reports a comparison between the FE model prediction and measurements from the SAC305 #2 test board.

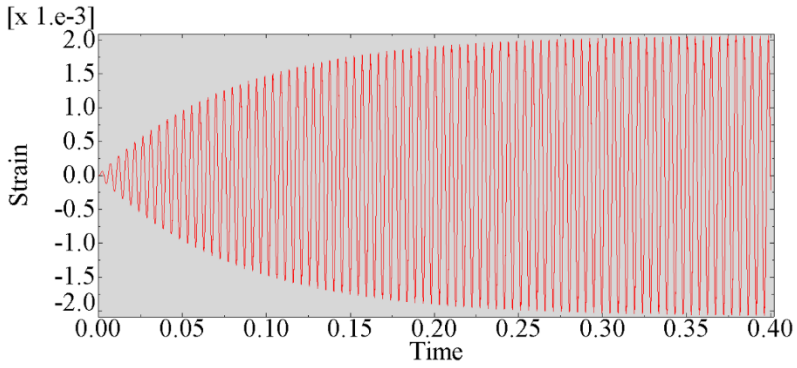

Figure 11. FEM PB Strain Response vs Time

Table 11. FE Model Prediction vs Experimental Measurement

Sensor	Experimental Measurement	FE Model Prediction	% Difference
SG1 (με)	238	243	2.1
SG2 (με)	438	424	3.25
SG3 (με)	600	607	1.16
SG4 (με)	540	548	1.47
Board Accelerometer (g)	190	174	8.8

The calibrated GM was then used to transfer the nodal displacements to the nonlinear LHMs of the CABGA192 and QFN68 components, as boundary condition histories, to estimate the cyclic strain history in the critical solder joints. The calibrated GM was also used to estimate PB strain amplitudes at the edges of the components (from the edge-centered virtual strain gauges). These PB strains, estimated from the edge-centered virtual strain gauges, provided measurements to develop the fatigue life data, as presented in Tables 4 and 5.

The author notes that the GM was calibrated using sensor data from a single test vehicle (SAC305 #2), where the calibrated damping and stiffness parameters were applied uniformly to all representative global models (Figure 6). Piece-to-piece variability in the dynamic transfer function (board acceleration response relative to base excitation) across the physical test vehicles was not individually accounted for in the GM, which is a source of uncertainty in the estimated PB strain amplitudes**.**

3.3.5 Local Half Model

In the local half-models (LHMs) and local quarter-models (LQMs), the following package features were modeled with continuum shell elements: silicon die, die attach, component substrate (where applicable), solder mask (where applicable), and FR4. The epoxy molding

compound (EMC) and solder were modeled as 8-noded linear hexahedral elements with reduced integration since they experience complex three-dimensional deformation fields.

The displacement field, estimated from the GM, around each selected component type is transferred to the corresponding LHM using the built-in displacement boundary condition transfer utility (termed ‘Submodeling’) within ABAQUS CAE. Additional boundary conditions were used to ensure symmetry in the LHM. The CABGA192 and QFN68 LHMs can be seen in Figure 12. Model dimensions were averaged from measurements obtained through cross-section images of pristine components.

In the LHM of the CABGA192, several model simplifications were made to improve the computational efficiency, without compromising the accuracy of the solder strain predictions. These simplifications include the use of a geometric half-symmetry model, reduction of the solder mask in-plane dimensions, exclusion of copper traces, and adopting a strategic mesh density.

The critical solder joint is the corner joint (furthest from the neutral point), since this is where the maximum deformation occurs [12]. The critical solder joint and its copper pads were modeled using a continuous mesh, all other solder interconnects were joined together using tie constraints. The critical joint was meshed with a fine mesh density, all other solder interconnects contained a coarse mesh, as seen in Figure 13. All regions which were in contact with the solder and copper pad were meshed using a localized fine mesh. This greatly reduces the number of elements, while maintaining model accuracy. The LHM of the CABGA192 contains 53263 elements. A mesh sensitivity analysis was conducted, under a simple bending moment loading condition, to verify that the selected mesh strategy yields sufficiently accurate results. This analysis is presented in Appendix A.2.

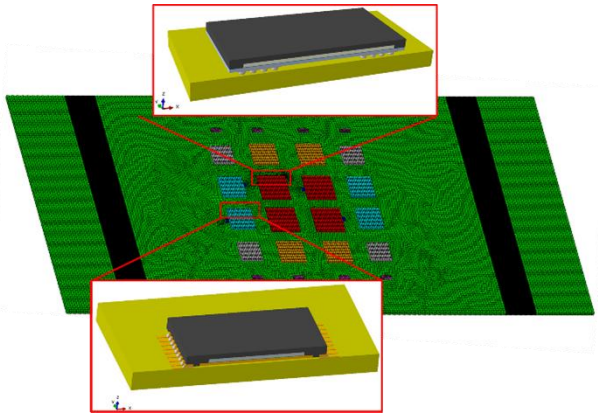

Figure 12. Position of the LHM of the QFN68 & CABGA192 on the GM

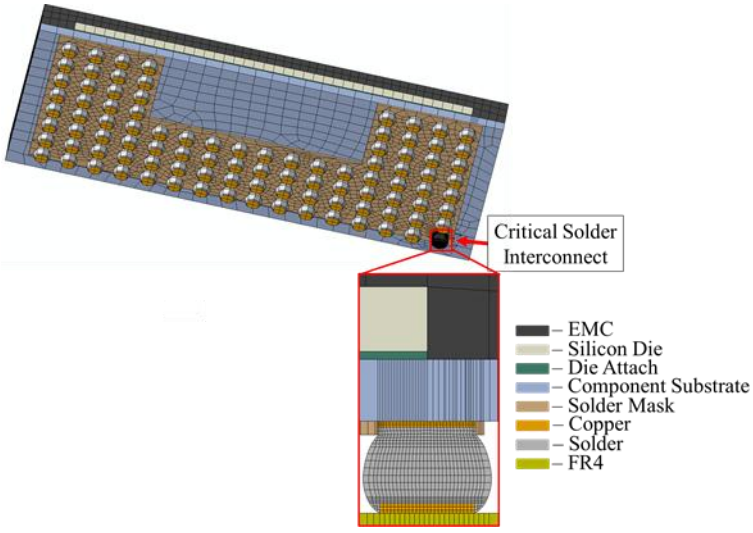

Figure 13. Cross Section & Mesh of CABGA192 LHM

The QFN68 LHM contains similar simplifications and model parameters as the LHM of the CABGA192. The copper lead pads were modeled, while the lead frame fingers were not. A significant amount of piece-to-piece stochastic dimensional variability in the solder joint geometry was present, but most tend to have bulbous fillets. The FEM captures this bulbous fillet

in the critical interconnect, as seen in Figure 14. The non-critical interconnects were modeled with straight fillets, also seen in Figure 14.

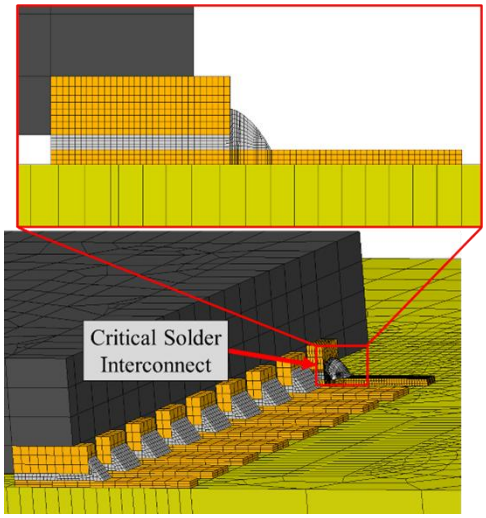

Figure 14. LHM of QFN68 Solder Joint Geometry & Cross Section

3.4 Results and Discussion

Fatigue relationships for each of the tested solders were developed by estimating the average cyclic strain amplitude within the critical region of the solder joint (discussed later in this section), for each test. To facilitate this process, FEA simulations were conducted to develop a strain transfer function, which relates the solder strain amplitude (volume-averaged in the critical region of the critical interconnect) to the PB bending strain amplitude (surface-averaged at the location of the corner virtual strain gauge). Details are presented in Section 3.4.1. For each test, the solder strain amplitude was estimated from the PB strain reported in the strain transfer function. The resulting strain amplitudes were then plotted against experimentally observed CTF data to construct solder fatigue life curves. The current study presents fatigue results primarily

within the HCF region as well as in the transition region between the HCF and LCF regions of the fatigue life curves, as seen in Figures 19-21.

3.4.1 Strain Transfer Functions

Strain transfer functions were developed for regions of the solder joints found to fail in test. The critical region in the CABGA192 solder joint was selected in the neck, as shown in Figure 15, representing 6.35% of the total volume of the solder ball. The critical region in the QFN68 solder joint, was selected to be 10 μm away from the top copper pad, as shown in Figure 16, representing 5.87% of the total volume of the solder joint. The volume-averaged strain in the footprint of the corner virtual strain gauge was assessed in the appropriate elements on the PB surface, as seen in Figure 17.

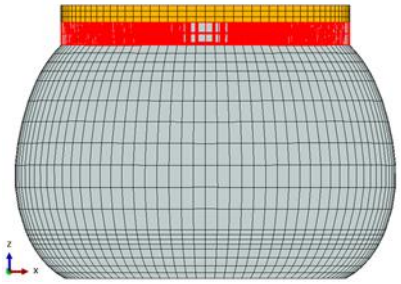

Figure 15. Critical Neck Region of CABGA192 Solder Ball.

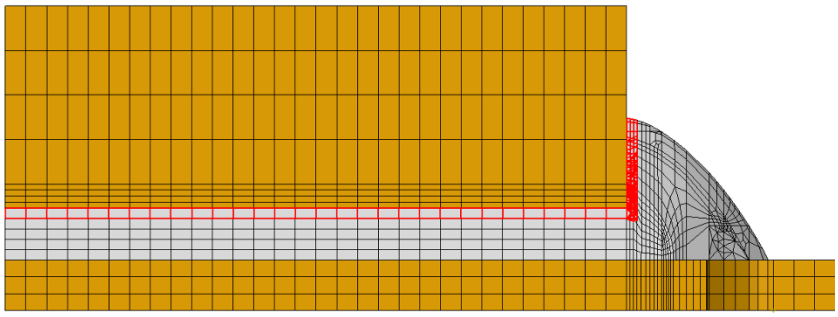

Figure 16. Critical Region of QFN68 Solder Joint

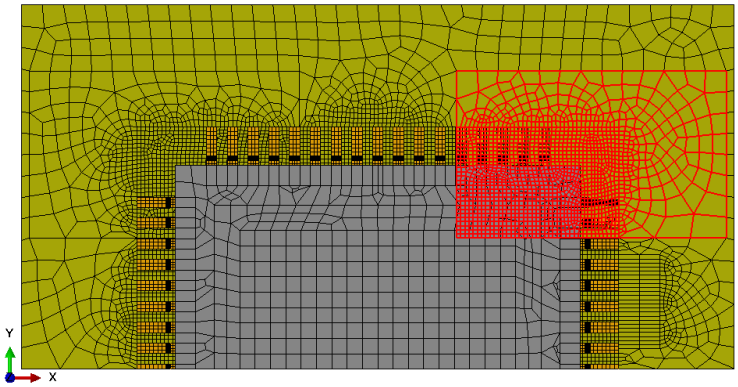

Figure 17. Representation of footprint of Corner Strain Gauge for the QFN68 component

Following GM calibration and transfer of boundary conditions to the LHMs, five GM simulations and 5 corresponding LHM simulations were performed for each CABGA192 and QFN68 component. Python scripts were used to compute the volume averaged strain (xx-direction) within both the corner strain gauge and the respective critical regions, using Equations (3) and (4). In Equation (3), the von Mises' (VM) strain, ε_{VM}, is computed using the components of the strain tensor, including the normal strain components, ε_{ii}, and shear strain components, ε_{ij}. In Equation (4), the volume averaged VM strain is computed from element volume, V_i, and previously defined VM strain. The strain transfer functions can be found in Figure 18.

$$\varepsilon_{\text{vm}} = \frac{\sqrt{2}}{3}\sqrt{(\varepsilon_{11}-\varepsilon_{22})^2+(\varepsilon_{22}-\varepsilon_{33})^2+(\varepsilon_{33}-\varepsilon_{11})^2+6[\varepsilon_{12}{}^2+(\varepsilon_{13})^2+(\varepsilon_{23})^2]} \quad (3)$$

$$\varepsilon_{Vol\ Avg} = \frac{\sum_{i=1}^{N}\varepsilon_{vm_i}V_i}{\sum_{i=1}^{N}V_i} \quad (4)$$

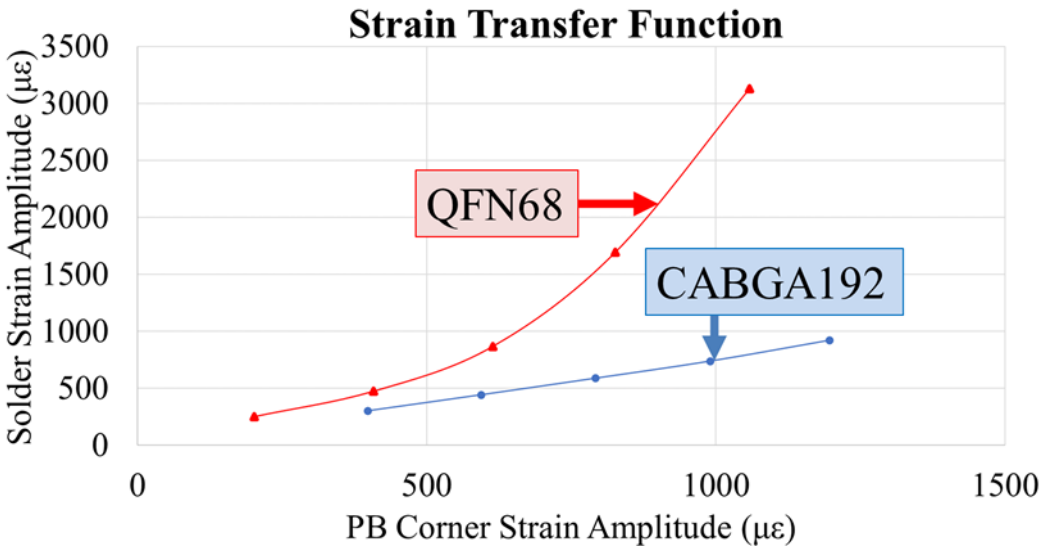

Figure 18. Strain Transfer Functions for the QFN68 and CABGA192 assemblies

3.4.2 Fatigue Life Curves

The SAC305 fatigue life curve was developed from datasets consolidated from this study and the literature [21-23], as seen in Figure 19(b). Solder fatigue relationships for the LTS interconnects are presented in Figures 20 and 21. The SAC305 data points from the CABGA192 and QFN68 components tested in this study are superposed on these plots to show the relative fatigue life between SAC305 and LTS. The master SAC305 SN curve is also included as a reference. Note that the master curve represents a best-fit through a broad compilation of SAC305 data and is not a fit through the present study's data points alone. A generalized Coffin-Manson relation (see Equation (5)) is developed by a least-square fitting approach. In Equation (5), ε_a is the total strain amplitude, σ_f', is the fatigue strength coefficient, E is the elastic modulus, b is the fatigue strength exponent, ε_f' is the fatigue ductility coefficient, c is the fatigue docility exponent, and N_f is the number of cycles to failure. For the CABGA192 components,

the fatigue curves represent the best available estimates of solder fatigue life given that the CABGA192 interconnects contain a hybrid ball joint construction. Similarly, the QFN68 fatigue curves represent the best available estimates given the presence of competing failure mechanisms in the copper traces and solder joints. Detailed failure analysis supporting these conclusions is presented in [3]. Thus, the fatigue curves presented here should be interpreted as a lower-bound representation for safe design. In other words, the true solder fatigue life is expected to exceed the value predicted by these curves.

$$\varepsilon_a = \frac{\sigma_f'}{E}\left(2N_f\right)^b + \varepsilon_f'\left(2N_f\right)^c \qquad (5)$$

In the QFN68 components, all LTS joints demonstrated higher fatigue life than SAC305 joints, while LTS1 and LTS3 outperformed LTS2. In the CABGA192 components, the best performing interconnect was dependent on the strain amplitude, with LTS1 performing better at strain amplitudes less than 500 με and LTS3 providing the best performance at strain levels greater than 500 με, both performed better than SAC305 and LTS2. These same solders have previously been studied under thermal cycling conditions, and the reported trends are similar with the findings of the present study, *i.e.*, all LTS joints displayed better fatigue life than SAC305 joints, while LTS1 and LTS3 demonstrated the highest fatigue life [24].

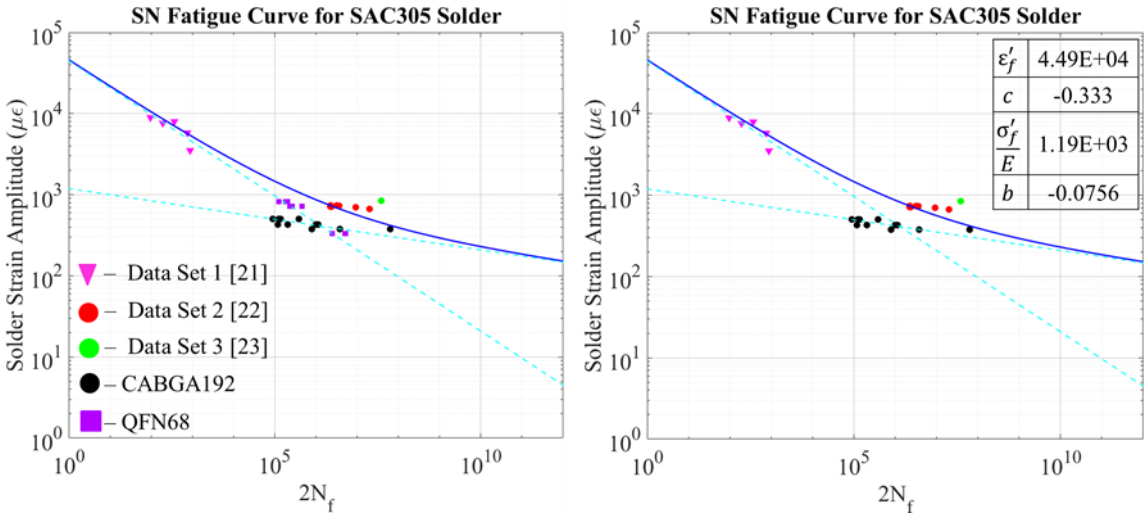

Figure 19(a)(b). Consolidated SAC305 Fatigue SN Curve, with and without QFN68 Data

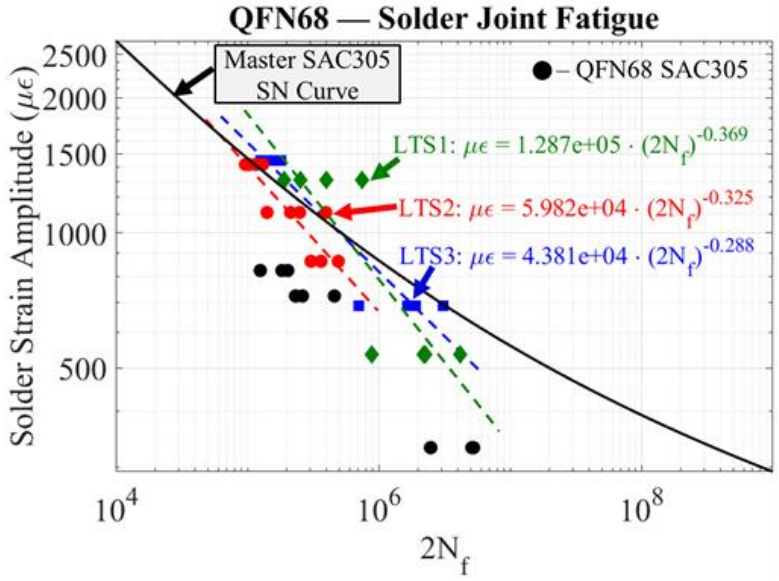

Figure 20. LTS Fatigue Life Curve for QFN68 Component

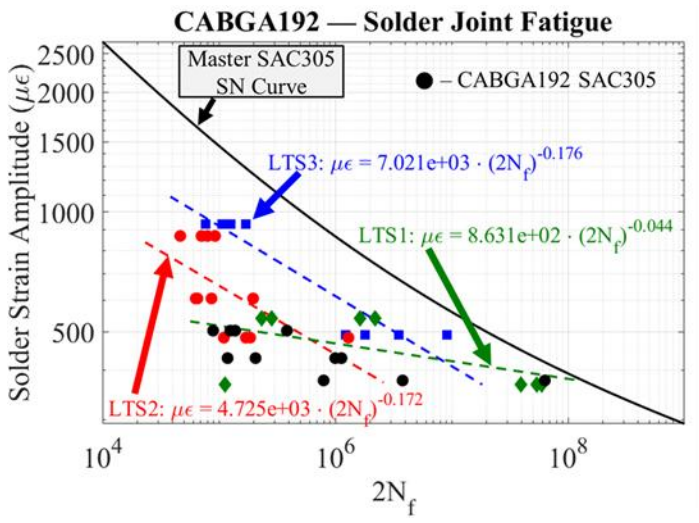

Figure 21. LTS Fatigue Life Curves for CABGA192 Components

3.4.2.1 Influence of Strain State (Triaxiality Ratio) on Solder Joint Fatigue

As seen in Figure 19(a) the QFN68 SAC305 joints are more fatigue-resistant than the CABGA192 SAC305 joints, i.e., QFN68 data points are shifted to the right of the CABGA192 data points under the same solder strain levels. This discrepancy originates from differences in the stress/strain state in the two different interconnect types, since geometry of BGA joint is very different from that of QFN joint (the aspect ratio of in-plane length vs height is smaller for BGA joints than for QFN joints). This geometric difference results in different strain triaxiality ratios in the two interconnect types (defined in Equation (4)). Both triaxiality ratios were estimated in this study with FEA simulations, using volume-averaged estimates of the hydrostatic and von Mises' strains in the critical regions within the critical joints, under the same response levels. The variables were defined earlier in Section 3.4.1.

$$\eta = \frac{\varepsilon_h}{\varepsilon_{VM}}, \quad \varepsilon_h = \frac{\varepsilon_{11}+\varepsilon_{22}+\varepsilon_{33}}{3} \qquad (4)$$

As shown in Figures 22 and 23, the VM strain versus triaxiality ratio and the triaxiality time histories reveal a clear difference between the cyclic histories of the strain states of the two interconnect types. The CABGA192 operates within a nearly symmetric triaxiality range, spending approximately equal portions of each cycle in tension and compression. On the other hand, the QFN68 spends the majority of its loading cycle at negative triaxiality states, with only a brief transition into positive triaxiality. In other words, the average cyclic strain state is more compressive in the QFN68 joint than the CABGA192 joint.

Prior work has shown that compressive hydrostatic stresses suppress void nucleation and crack opening in BGA solder interconnects [25,26], and therefore the higher (tensile) triaxiality experienced by the CABGA192 joint is expected to increase fatigue damage accumulation rates compared to that in the QFN68 joint. Similar trends were reported for solder specimens of high aspect-ratio (similar to the aspect ratio of QFN68 joints) by Deshpande et al. [21] for SAC305 under cyclic shear, tensile, and multiaxial tests. Their failure analysis revealed that under multiaxial loading, failures occurred at both the IMC layer and the solder bulk, consistent with the failures found in the QFN68 solder joints [3,21]. Thus, the higher strain triaxiality in CABGA192 joint is consistent with the fact that the CABGA192 interconnects failed sooner than QFN68 interconnects, under similar cyclic amplitudes of von Mises' strain.

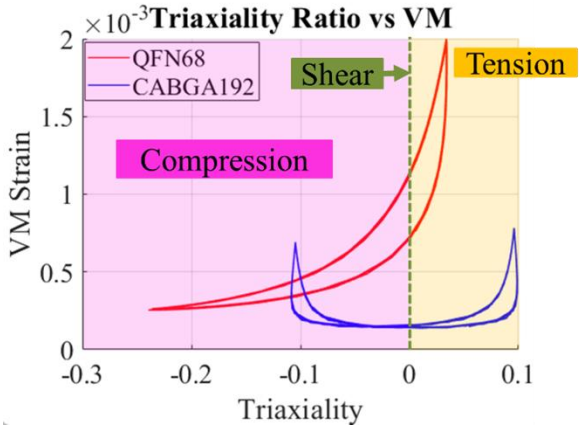

Figure 22. Strain Triaxiality Ratio vs VM Strain in CABGA192 and QFN68 Components

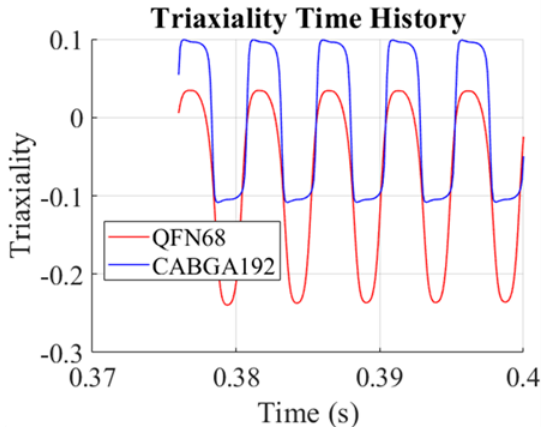

Figure 23. Triaxiality Ratio History for CABGA192 and QFN68 Components

3.4.2.2 Influence of Hybrid Construction on Failure of LTS Joints

The LTS CABGA192 components consist of hybrid interconnects (SAC305 solder ball combined with LTS paste) [27,28], while the SAC305 CABGA192 consists of fully SAC305 solder joints. From experiments, the vibration fatigue failures in all the BGA components consistently occurred in the neck region of the joint, within the SAC305 ball, regardless of whether the joint was a hybrid LTS configuration or pure SAC305 configuration. Despite failures occurring within the SAC305 ball, the LTS interconnects displayed superior vibration

fatigue life compared to the pure SAC305 joints. This behavior is hypothesized to be in part due to strain redistribution within the joint, as the higher compliance of the LTS paste (compared to SAC305) reduces the cyclic strain experienced in the neck of the SAC305 ball.

To verify this hypothesis, one additional simulation was conducted for the highest-strain corner case of the CABGA192 LHM. In this case, the critical solder joint was modeled as a simplified hybrid joint, with 57% of the joint volume being represented by 42Sn68Bi LTS material properties, shown in Figure 24. The LTS elastic modulus was approximated to be about 54% of the SAC305 elastic modulus based on the literature [26]. The stress in the LTS region was well below its yield strength, thus generating only elastic deformation in that region. This analysis approximates the effect of utilizing a hybrid interconnect, and reveals that the LTS paste reduced the volume-averaged VM strains in the critical region (at the neck of the SAC305 ball) by approximately 6%, confirming that the LTS portion of the hybrid ball absorbs strain energy thereby increasing the fatigue life of hybrid joints.

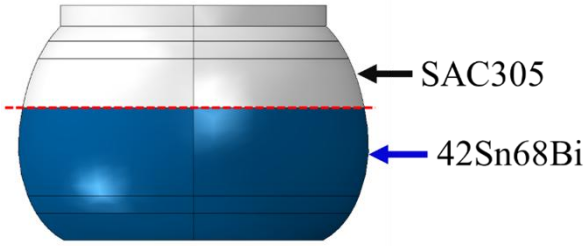

Figure 24. FEA Approximation of LTS Hybrid BGA

3.4.3 Non-linear Vibration Contributions in CFCF Test Setups

During post-processing of the acceleration data from the harmonic vibration tests, several test boards exhibited a significant non-harmonic response history. Figure 25 presents representative

acceleration time histories, from the same test, recorded during the initial ramp-up phase and at the end of the ramp-up phase. The response at low excitation, during the ramp-up phase, is harmonic. However, as the test progresses and reaches the full excitation level, the response transitions to a non-harmonic form [3, 29]. This behavior was observed in multiple test boards subjected to higher excitation levels [3], motivating a further investigation into the underlying mechanics responsible for this observed non-linear dynamic response. This analysis can be found in Appendices A.3.

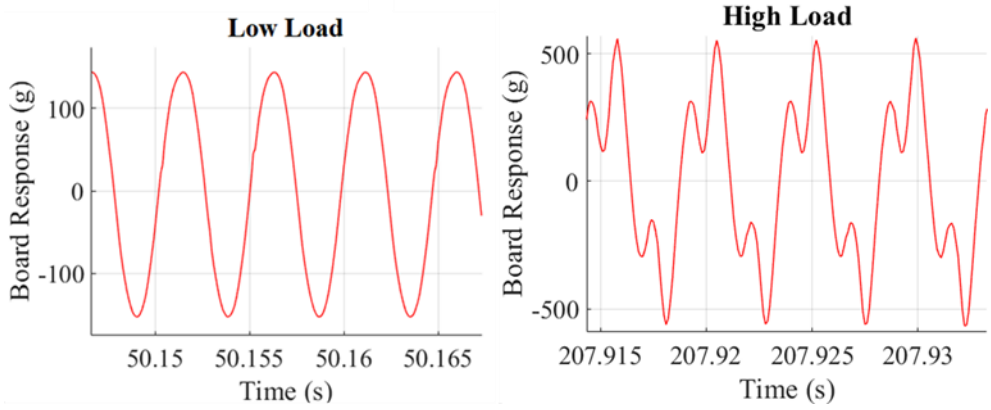

Figure 25. Time Histories of PBA Accelerometer Reading: Ramp-Up (Low Load) and Dwell (High Load)

3.4.4. Validation of Quasi-Static LHM Assumption

As discussed in Section 3.3.1, the detailed nonlinear LHM modeling is based on quasi-static analysis (instead of fully dynamic analysis) for computational expedience. This approach captures the solder joint deformation induced by the flexure of the PB, but does not account for the inertial forces generated by the component mass during vibration. To assess the impact of this simplification, the peel stress contribution from the component inertia is analytically estimated and compared against the flexure-induced peel stress predicted by FEA. The QFN68

component was selected for this verification as it is more susceptible to inertial loading due to the smaller total footprint area of interconnects, compared to the much higher I/O count and area in the CABGA192 component.

The inertial stress contribution was estimated by considering the inertial force acting on the interconnects due to the component mass undergoing the board acceleration. The resulting peel stress was estimated by approximating the inertial force as being uniformly distributed across the footprint area of each of the 68 solder joints. This analytically estimated inertial stress contribution is 0.101 MPa. In contrast, the volume-averaged peel stress, estimated in the LHM FEA at the critical corner joint of the QFN68 (representative of the flexure induced contribution), was 13.8 MPa.

The inertial stress contribution is approximately two orders of magnitude smaller than the flexure-induced peel stress, which confirms that PB flexure is the dominant loading mechanism on the solder joint. The inertial contribution represents less than 1% of the total joint stress, indicating that the error introduced by the quasi-static approximation is negligible.

3.5 Conclusion

In this study, a multiscale global/local sub-modeling approach was developed to extract solder strains from vibration fatigue life tests of several low-temperature solder (LTS) and SAC305 assemblies. Two types of interconnect styles were studied here: CABGA12 and QFN68A. The LTS BGA components had hybrid bi-material joints with SAC305 solder ball and LTS paste, while the QFN solder joints were mono-material joints. A simplified linear-elastic global model was developed for the PBA and calibrated to within 5% of experimentally

measured response strain levels. Detailed nonlinear local half models were built for CABGA192 and QFN68 components and were used to estimate solder strains within the critical solder joint. Due to limited availability and consensus in the literature for material properties of the LTSs, all solder joints were modeled using elastic-plastic mechanical properties of SAC305.

Estimated solder strains in the critical regions of the critical joints were used to develop fatigue life curves for each solder system for the CABGA192 and QFN68 interconnects. All the LTS joints were found to be more fatigue resistant than their SAC305 counterparts, across both component styles. Failures in all the BGA joints were found to be in the neck of the SAC305 solder ball, and the higher fatigue life of the hybrid LTS BGA joints was attributed in part to the reduction of strain levels in the SAC305 neck due to the higher compliance of the LTS paste materials. LTS1 and LTS3 exhibited comparable behavior and displayed the highest fatigue resistance for the QFN68 interconnects. In contrast, the solder with the greatest fatigue resistance was dependent on the strain amplitude. For the CABGA192 interconnects. LTS1 performed the best at strain amplitudes below 500 με, while LTS3 performed best above this strain level.

A mesh sensitivity analysis was conducted to verify that the implemented meshing strategy, used during solder strain extraction, was both efficient and accurate. Results confirm that the adopted meshing strategy was sufficiently refined to provide meaningful comparisons of fatigue results.

A.3. Appendices

The Appendices contain supplementary data which are relevant to several discussions throughout this study.

A.3.1 Material Properties

Table 6. Summary of Material Properties

Material	Density (Tonne/mm^3)	Young's Modulus (MPa)	ν	Source
Die Attach	2.80E-09	3000	0.28	[30]
Silicon Die	2.33E-09	See Table 7	See Table 7	[31]
EMC	1.79E-09	23000	0.3	[32]
FR4 (Non-Calibrated)	2.00E-09	See Table 7	See Table 7	[18]
SAC305	8.40E-09	See Table 8	See Table 8	[19]
Solder Mask	1.20E-09	3000	0.35	[33]
Component Substrate	2.00E-09	21700	0.18	[32]
Copper Pad	8.96E-09	120000	0.35	[10]
FR4 (Calibrated)	2.00E-09	See Table 7	See Table 7	~

Table 7. Detailed material properties for orthotropic materials

Material	E_x (MPa)	E_y (MPa)	E_z (MPa)	ν_{xy}	ν_{xz}	ν_{yz}	G_{xy}	G_{xz}	G_{yz}
FR4 (Non-Calibrated)	12668	12668	6228.4	0.105	0.238	0.238	2900	2900	3700
FR4 (Calibrated)	21789	21789	10713	0.105	0.238	0.238	6364	4988	4988
Silicon Die	169000	169000	130000	0.0642	0.362	0.362	50900	79600	79600

Table 8. Inelastic material properties for SAC305

Young's Modulus (MPa)	ν	Yield Stress	Plastic Strain
36000	0.36	5.68	0
		28.2	6.05E-05
		33.3	0.000161
		37.1	0.000301
		44.2	0.000841
		54.9	0.003
		67.4	0.01
		88.6	0.05
		99.7	0.1
		112	0.2

A.3.2 Mesh Sensitivity Analysis

Due to the complexity of each of the LHMs, several modifications were made to ensure computational efficiency while maintaining solution accuracy. As discussed in Section 3.3.5, several geometrical simplifications were introduced to reduce computational cost. In addition, a strategic mesh density was implemented to further improve efficiency. To understand how mesh density affects the solution, a simple bending moment was applied to the LHM of the CABGA192, which was similarly done during the GM calibration.

Three LHMs of the CABGA192 were used, denoted as MD1, MD2, and MD3. In all cases, the mesh within the PB, EMC, Si die, and die attach are the exact same size. The varying parameter is the mesh density within the component substrate and the solder mask. MD1 represents a coarse mesh, MD2 represents a very fine mesh, and MD3 represents a fine mesh

density only in the region near the critical solder joint, depictions of the mesh density of each of these cases can be seen in Figure 26.

Figure 26. Mesh Density in Each Case

A simple bending moment was applied to one end and the strains within the critical region in the solder joint were analyzed. The results shown in Figure 27 indicate that the coarse mesh contains the largest strain response, while MD2 and MD3 are virtually identical, with a difference of just 0.1%. The corresponding simulation times for MD1, MD2, and MD3 were approximately 12 minutes, 8 hours, and 20 minutes, respectively. These results show how that the MD3 meshing strategy achieves accurate strain predictions, while significantly reducing computational costs. These results are consistent with findings from Fan et al [11].

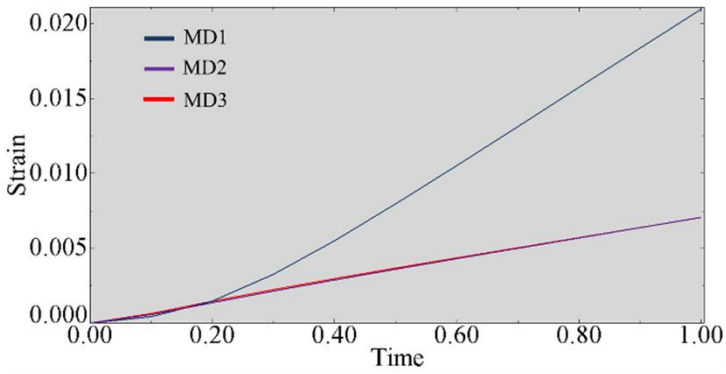

Figure 27. Results from Mesh Sensitivity Analysis

A.3.3 Nonlinear Response Leading to Super-Harmonics of a PBA

A Fast Fourier Transform (FFT) analysis was performed on the strain and acceleration responses of the PB, which revealed dominant frequnecy components occuring at exact multiples of the first natural frequnecy, indicative of a superharmonic response [29,34], a represenative example can be seen in Figure 30. Although several high load test vehciles exhibited superharmonic behavior, the magitude of the third superharmonic response varied significantly, even among tests condcuted at comparable load levels [3]. This is believed to occur when the third superharmonic frequency is sufficenty close to the third modal frequency of the PBA, thus activating the third flexural mode, causing energy to leak from Mode 1 into Mode 3 [34,35].

To study this effect, parametric FEA simulations were conducted, using a nonlinear version of the calibrated GM. Two modifications to the GM were introduced to isolate and quantify this observed behavior. First, kinematic nonlinearity (for large deformations) was activated in the model with a non-linear dynamic solver, to capture their influence on membrane strains and the non-linear response of the PB. Second, the FE model mesh was coarsened to increase computational efficency for nonlinear simulations.

Two parametric versions of the PBA of were simulated to investigate the possibility of Mode 3 participation in the nonlinear response to Mode1 excitation. The stiffness distribution of the printed board in the model was parametrically varied in these two model cases, to vary the separation Δf between the frequencies of Mode 3 and the 3rd superharmonic of Mode 1, i.e. $\Delta f = 3f_1 - f_3$ (where f_1 is the fundamental resonant frequency and f_3 is the 3rd resonant frequency). Case 1 is the original GM with a relatively large Δf, while Case 2 is tailored to make Δf very small. Figure 28 shows the third mode shape and the blue region that was parametrically stiffened to

tailor Δf. Table 12 summarizes the first three natural frequncies of the FE GM in each case, illustrating that the resulting Δf is 92.5 Hz for Case 1 and 0.6 Hz for Case 2.

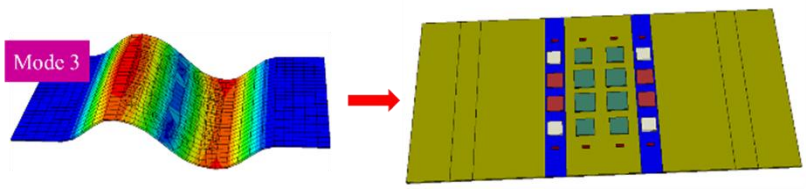

Figure 28. FEA Guided Locations where the PB is Artificially Stiffened

Table 12. Summary of Case 1 and Case 2 FEA Natural Frequencies

Mode #	Case 1 (Hz)	Case 2 (Hz)
1	207.98	203.95
2	263.95	299.06
3	531.45	611.37

To quantify the effects of energy transfer between the third superharmonic of Mode 1 and the third natural mode, the acceleration response at two locations on the PB was analyzed using FFTs. Then, the ratios between the magnitudes at the third and first (3:1) frequency responses were compared for each of the two cases at each of the two locations. The first location is denoted as the "Center" and the second is labeled as "Side", Figure 29 shows these locations.

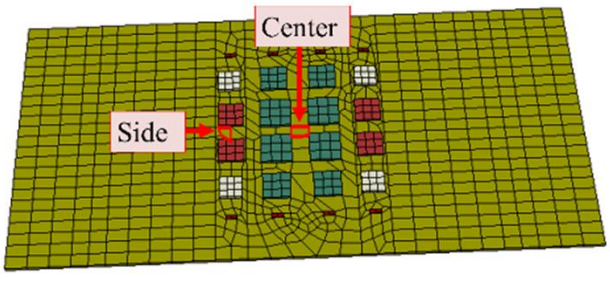

Figure 29. Analyzed Locations for Non-Linear Effect Analysis in FEA

FFTs for the presented cases can be seen in Figure 30. Based on the responses at 'Side' location, Case 1 displayed a 3:1 ratio of 0.034 and Case 2 displayed a 3:1 ratio of 0.11 increasing by 3.24x from Case 1 to Case 2. In the center location responses, Case 1 displayed a 3:1 ratio of 0.032 and Case 2 displayed a 3:1 ratio of 0.068, increasing by 2.13x. A summary of the FFT ratios is provided in Table 13. These findings suggest that when Δf approaches zero, *i.e.* when the third natural frequency approaches the third superharmonic frequency (thrice the first natural frequency) energy is likely to be transferred from Mode 1 response to Mode 3 response. Additional FFT plots for all cases can be found in the supplementary material section.

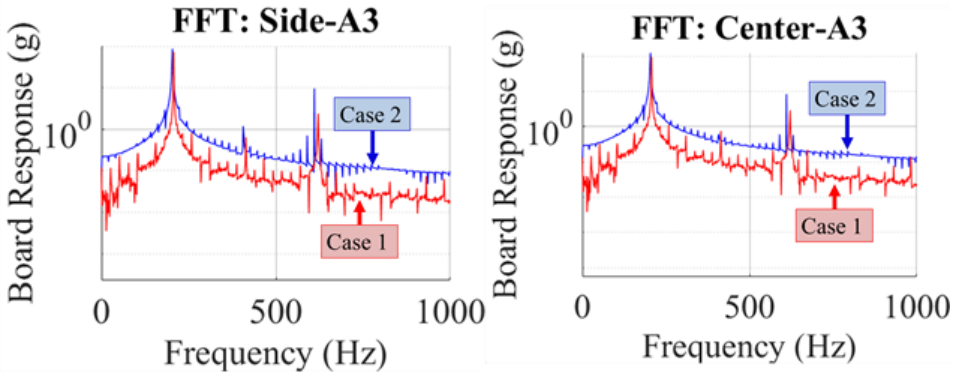

Figure 30. Example of the FFTs Performed in this Analysis

Table 13. Summary of FFT Ratio Analysis

Case	Side Ratio	Center Ratio
1	0.034	0.11
2	0.032	0.068

Acknowledgement

The CALCE Consortium has served the electronics industry for more than 40 years, providing a knowledge and resource base for the development and sustainment of competitive electronics products and systems. CALCE members define research needs and direction and share in the findings. The author would like to thank several graduate research assistants who supported this study, including but not limited to Idowu Olajire Olatunji, Randall Silvestro, Jonathan Hower, Louis Hardock, and Alix Lemaile.

Funding Data

This work has been sponsored by members of the CALCE Electronic Products and Systems Consortium.

Conflict of Interest

The corresponding author declares no conflicts of interest regarding this article.

Data Availability Statement

The data presented in this article are available from the corresponding author upon reasonable request.

Nomenclature

f_1	fundamental resonant frequency
f_3	3rd resonant frequency
ε_a	strain amplitude
$\varepsilon_f^{'}$	fatigue ductility coefficient
ε_h	hydrostatic strain
ε_{ij}	Tensorial strain components
ε_{VM}	von Mises’

$\varepsilon_{Vol,Avg}$	volume averaged strain
$\sigma_f^{'}$	fatigue strength coefficient
b	fatigue strength exponent
c	fatigue ductility exponent
E	Young's modulus
K	curvature
V	element volume
Δf	change in frequency
ε	strain
η	strain triaxiality ratio
με	microstrain
BGA	Ball Grid Array
CABGA	ChipArray Ball Grid Array
CFCF	Clamped-Free-Clamped-Free
CTBGA	ChipArray Thin Core Ball Grid Array
CTE	Coefficient of Thermal Expansion
CTF	Cycles-to-Failure
CVBGA	Very Thin Chip Array Ball Grid Array
EDS	Energy Dispersive X-ray Spectroscopy
EMC	Epoxy Molding Compound
FE	Finite Element
FEA	Finite Element Analysis
FEM	Finite Element Model
FFT	Fast Fourier Transform
FR4	Flame Retardant 4
GLB	Global Local Beam
GM	Global Model
HCF	High-Cycle Fatigue
IMC	Intermetallic Compound
LCF	Low-Cycle Fatigue
LHM	Local Half Model
LM	Local Model
LQM	Local Quarter-Symmetry Model
LTS	Low-Temperature Solder
MD	Mesh Density
PB	Printed Board
PBA	Printed Board Assembly
QFN	Quad-Flat-No Lead
SAC305	Tin-Silver-Copper solder alloy (96.5Sn-3.0Ag-0.5Cu)
SF	Stiffening Factor
SG	Strain Gauge
SMR	Surface Mounted Resistor
SN	Strain-life
VM	von Mises

References

[1] N. Muthuram and S. Saravanan, "Fatigue life based study of Electronic Package Mounting Locations on Printed Circuit Boards Subjected to Random Vibration Loads", *J. Electron. Test*, vol. 40, pp. 761–776, (2024). https://doi.org/10.1007/s10836-024-06151-5

[2] D. Yun Chen and M. Osterman, "Reliability of corner staked surface mount packages," 2016 IEEE Accelerated Stress Testing & Reliability Conference (ASTR), Pensacola Beach, FL, USA, 2016, pp. 1-6, https://doi.org/10.1109/ASTR.2016.7762272

[3] Martin, J. C., Bharamgonda, A. A., Osterman, M., and Dasgupta, A., submitted, "Experimental Fatigue Life Comparison of Low-Temperature Solders Under Harmonic Vibration," ASME Journal, Apr. 2026, manuscript under review.

[4] T. An, F. Qin, B. Zhou, P. Chen, Y. Dai, H. Li, T. Tang, Vibration lifetime estimation of PBGA solder joints using Steinberg model, Microelectronics Reliability 102 (2019) 113474. https://doi.org/10.1016/j.microrel.2019.113474

[5] Da Yu, Abdullah Al-Yafawi, Tung T. Nguyen, Seungbae Park, Soonwan Chung, High-cycle fatigue life prediction for Pb-free BGA under random vibration loading, Microelectronics Reliability, Volume 51, Issue 3, 2011, Pages 649-656, ISSN 0026-2714, https://doi.org/10.1016/j.microrel.2010.10.003.

[6] Y.S. Chen, C.S. Wang, Y.J. Yang, Combining vibration test with finite element analysis for the fatigue life estimation of PBGA components, Microelectronics Reliability, Volume 48, Issue 4, 2008, Pages 638-644, ISSN 0026-2714, https://doi.org/10.1016/j.microrel.2007.11.006.

[7] Richards, H., Dasgupta, A., Bujanda, A., Tsang, H., and Bowman, M. (August 25, 2025). "Low-Cycle Fatigue of Sintered Silver in Polymeric-Substrate Printed Hybrid Electronic Assemblies Subject to Extreme Strain Induced by Mechanical Shock." ASME. J. Electron. Packag. December 2025; 147(4): 041103. https://doi.org/10.1115/1.4069321

[8] I. Olatunji, A. Deshpande, M. Bascolo, A. Dasgupta, U. Becker and G. Jokai, "Durability of Copper Traces in Ball Grid Array (BGA) Assemblies under Sequential Harmonic Vibration and Temperature Cycling," 2022 23rd International Conference on Thermal, Mechanical and Multi-Physics Simulation and Experiments in Microelectronics and Microsystems (EuroSimE), St Julian, Malta, 2022, pp. 1-5, https://doi.org/10.1109/EuroSimE54907.2022.9758863.

[9] Kim, Y. K., Lee, S.-M., Hwang, D.-S., & Jang, S., "Analyses on the large size PBGA packaging reliability under random vibrations for space applications," Microelectronics Reliability, vol. 109, p. 113654, 2020. https://doi.org/10.1016/j.microrel.2020.113654

[10] D. Farley, Y. Zhou, F. Askari, M. Al-Bassyiouni, A. Dasgupta, J.F.J. Caers, J.W.C. DeVries, Copper trace fatigue models for mechanical cycling, vibration and shock/drop of high-density PWAs, Microelectronics Reliability, Volume 50, Issue 7, 2010, Pages 937-947, ISSN 0026-2714, https://doi.org/10.1016/j.microrel.2010.03.004

[11] Xuejun Fan, Min Pei and P. K. Bhatti, "Effect of finite element modeling techniques on solder joint fatigue life prediction of flip-chip BGA packages," 56th Electronic Components and Technology Conference 2006, San Diego, CA, USA, 2006, pp. 9 pp.-, https://doi.org/10.1109/ECTC.2006.1645772.

[12] Che, F.X., Pang, J.H.L., Vibration reliability test and finite element analysis for flip chip solder joints, Microelectronics Reliability, Vol. 49, No. 7, pp. 754–760, 2009, https://doi.org/10.1016/j.microrel.2009.03.022.
[13] F. X. Che et al., "Development and Assessment of Global-Local Modeling Technique Used in Advanced Microelectronic Packaging," 2007 International Conference on Thermal, Mechanical and Multi-Physics Simulation Experiments in Microelectronics and Micro-Systems. EuroSime 2007, London, UK, 2007, pp. 1-7, https://doi.org/10.1109/ESIME.2007.360018.
[14] Hower, Jonathan. "DROP DURABILITY ASSESSMENT OF ELECTRONIC ASSEMBLIES UNDER OFF-AXIS LOADING WITH SKEWED FIXTURES." , Aug. 2025., http://hdl.handle.net/1903/34735
[15] Yusuf Cinar, Jinwoo Jang, Gunhee Jang, Seonsik Kim, Jaeseok Jang, Effect of solder pads on the fatigue life of FBGA memory modules under harmonic excitation by using a global–local modeling technique, Microelectronics Reliability, Volume 53, Issue 12, 2013, Pages 2043-2051, ISSN 0026-2714, https://doi.org/10.1016/j.microrel.2013.06.018.
[16] Martin, J.C., Bharamgonda, A.A., Osterman, M., and Dasgupta, A., "Low-Temperature Solder Vibration Durability," *SMTA International*, pp. 194–198, October 19, 2025. https://doi.org/10.37665/smEUQHO14789

[17] "Performance Test Methods and Qualification Requirements for Surface Mount Solder Attachments," IPC-9701A, 2006, https://www.electronics.org/TOC/IPC-9701A.pdf
[18] E. Lin, "Effect of Isothermal Aging on SAC305 Harmonic Vibration Fatigue life", M.S. Thesis, Department of Mechanical Engineering, University of Maryland, College Park, MD, USA, 2016, http://hdl.handle.net/1903/18420
[19] Y. Zhang, Z. Cai, J. C. Suhling, P. Lall, and M. J. Bozack, "The effects of aging temperature on SAC solder joint material behavior and reliability," *2008 58th Electronic Components and Technology Conference*, Lake Buena Vista, FL, 2008, pp. 99-112, https://doi.org/10.1109/ECTC.2008.4549956
[20] Deng Yun Chen, Michael Osterman, Abhijit Dasgupta, Energy based modeling for temperature cycling induced tin silver copper solder interconnect fatigue life, Microelectronics Reliability, Volume 109, 2020, 113651, ISSN 0026-2714, https://doi.org/10.1016/j.microrel.2020.113651.

[21] Deshpande, A., Jiang, Q., Dasgupta, A., and Becker, U. (September 15, 2021). "Role of Nominal Stress State on Cyclic Fatigue Durability of SAC305 Grain-Scale Solder Joints." ASME. *J. Electron. Packag*. September 2022; 144(3): 031006. https://doi.org/10.1115/1.4051647
[22] I. Olatunji, M. Osterman, and A. Dasgupta, "CALCE Internal Report," Center for Advanced Life Cycle Engineering (CALCE), University of Maryland, College Park, MD, USA, 2026.

[23] A. Bharamgonda, M. Osterman, and A. Dasgupta, "CALCE Internal Report RSS_Spring2026_09," Center for Advanced Life Cycle Engineering (CALCE), University of Maryland, College Park, MD, USA, 2026.
[24] Osterman, M., & Mendelsohn, A. "Thermal Cycle Fatigue Life of Low-Temperature Solders". Proceedings of the SMTA International Conference (SMTAI), Surface Mount

Technology Association, original publication year as in proceedings. CALCE, University of Maryland, College Park, MD, USA, https://doi.org/10.37665/smXHJGJ19902.
[25] Shetty, S., Lehtinen , V., Dasgupta, A., Halkola , V., and Reinikainen, T. (March 25, 2000). "Fatigue of Chip Scale Package Interconnects Due to Cyclic Bending ." ASME. J. Electron. Packag. September 2001; 123(3): 302–308. https://doi.org/10.1115/1.1362673
[26] Darbha, K., Okura, J. H., Shetty, S., Dasgupta, A., Reinikainen, T., Zhu, J., and Caers, J. F. J. M. (December 1, 1999). "Thermomechanical Durability Analysis of Flip Chip Solder Interconnects: Part 2—With Underfill." ASME. J. Electron. Packag. December 1999; 121(4): 237–241. https://doi.org/10.1115/1.2793846
[27] S. Chakraborty, M. A. Maruf, G. R. Mazumder, J. C. Suhling, and P. Lall, "Investigation of the Tensile and Creep Responses of Mixed SAC-LTS Alloys with Varying Bi Concentration," *Proceedings of the 2026 Intersociety Conference on Thermal and Thermomechanical Phenomena in Electronic Systems (ITherm)*, 2026.
[28] S. Sahasrabudhe et al., "Low Temperature Solder – A Breakthrough Technology for Surface Mounted Devices," 2018 IEEE 68th Electronic Components and Technology Conference (ECTC), San Diego, CA, USA, 2018, pp. 1455-1464, https://doi.org/10.1109/ECTC.2018.00222
[29] U. Andreaus, P. Baragatti, Experimental damage detection of cracked beams by using nonlinear characteristics of forced response, Mechanical Systems and Signal Processing, Volume 31, 2012, Pages 382-404, ISSN 0888-3270, https://doi.org/10.1016/j.ymssp.2012.04.007.
[30] I. Maus et al., "Characterization of epoxy based highly filled die attach materials in microelectronics," 2017 18th International Conference on Thermal, Mechanical and Multi-Physics Simulation and Experiments in Microelectronics and Microsystems (EuroSimE), Dresden, Germany, 2017, pp. 1-7, https://doi.org/10.1109/EuroSimE.2017.7926237.
[31] M. A. Hopcroft, W. D. Nix and T. W. Kenny, "What is the Young's Modulus of Silicon?," in Journal of Microelectromechanical Systems, vol. 19, no. 2, pp. 229-238, April 2010, https://doi.org/10.1109/JMEMS.2009.2039697
[32] Zhang, Q., Lo, J. C. C., Ricky Lee, S. W., and Xu, W. (September 10, 2018). "Correlation of Warpage Distribution With the Material Property Scattering for Warpage Range Prediction of PBGA Components." ASME. J. Electron. Packag. December 2018; 140(4): 041005. https://doi.org/10.1115/1.4041064.
[33] I. C. Ume and T. Martin, "Finite element analysis of PWB warpage due to cured solder mask-sensitivity analysis," in IEEE Transactions on Components, Packaging, and Manufacturing Technology: Part A, vol. 20, no. 3, pp. 307-316, Sept. 1997, https://doi.org/10.1109/95.623025.
[34] Justin H. Porter, Matthew R.W. Brake, Tracking superharmonic resonances for nonlinear vibration of conservative and hysteretic single degree of freedom systems, Mechanical Systems and Signal Processing, Volume 215, 2024, 111410, ISSN 0888-3270, https://doi.org/10.1016/j.ymssp.2024.111410.
[35] H. Nayfeh and D. T. Mook, *Nonlinear Oscillations*. New York, NY, USA, Wiley, 1979, sec. 6.3.2.

Chapter 4: Conclusions, Contributions, Future Work

4.1. Conclusions, Contributions, Future Work

This thesis presents the outcome of harmonic vibration durability experiments and finite element modeling to develop durability curves and fatigue curves for three commercially available low-temperature solder (LTS) materials. Results are compared to SAC305 durability for benchmarking purposes. A summary of the conclusions, contributions, and future work are presented in this Chapter.

4.1.1. Summary and Conclusions

The research conducted was organized into three sequential phases: (i) developing a vibration test methodology, (ii) conducting harmonic vibration durability tests, and (iii) establishing a finite element modeling framework to develop fatigue models for LTS solders, based on simulation of the interconnects of the CABGA192 and QFN68 components.

Phase 1 established a recommended test procedure for conducting harmonic vibration durability tests on printed board assemblies (PBA) populated with 24 surface mounted components, consisting of four each of the following component styles: CABGA192, CTBGA228, CVBGA360, QFN68, and two styles of 1206 surface mounted resistors (SMR). All components other than the SMRs were tested to failure. Separate test vehicles were assembled using one of four distinct solder configurations: SAC305, LTS1, LTS2, and LTS3. All LTS materials are micro-alloyed tin-bismuth based solders with melt temperatures ranging from 137-150°C, in contrast to SAC305 solder with melt temperature 217°C. BGA components in the LTS test vehicles had SAC305 balls forming a hybrid bi-material interconnect using LTS paste with a

SAC305 solder ball. QFN68 components contained homogeneous single-material joints that assembled using an appropriate solder alloy.

A custom clamped-free-clamped-free (CFCF) fixture was designed, and a resonance tracking control algorithm was used to maintain consistent board response levels throughout each test. During durability trials, the vibration response was controlled using the board accelerometer, ensuring that the printed wiring board (PWB) response remained at the intended target level regardless of variations in fixturing or clamping conditions. Test boards were thermally pre-aged for 100 hours at 0.8 homologous temperature to stabilize the metallurgical state and minimize piece-to-piece variability. Afterwards, each test board was instrumented with strain gauges, accelerometers, and resistance monitoring wires. Sine sweep tests were conducted on all test vehicles prior to any overstress or durability tests. Overstress tests were conducted to define target load levels for the durability tests, at least two durability trials were conducted per solder configuration. Due to the high sensitivity of strain measurements with respect to gauge placement underneath the component footprints, achieving consistent gauge locations across all test vehicles is unrealistic. To address this, PWB strain amplitudes were estimated from a calibrated global model, which allowed for consistent and precise measurement locations across all test vehicles. These FEA estimated strains were used to construct the durability plots.

In the second phase, vibration durability tests were conducted at multiple load levels for each of the tested solder configurations. The durability results revealed that the performance of each interconnect is dependent on both the PWB strain and component type. Across all component types and tested strain levels, all LTS interconnects demonstrated higher durability than SAC305. LTS1 and LTS3 generally displayed the highest vibration durability for the CABGA192, QFN68, and CTBGA228 components, while the CVBGA360 components showed

relatively little differentiation among the three LTS interconnects, with LTS2 performing slightly better. Failure analysis, through destructive cross-sectioning, was performed on all components. Within the BGA styles, failures were observed to occur mostly within the neck region of the SAC305 solder ball, towards the component side. Copper trace failures were not observed in the BGA components. The QFN68 components contained cracks through the solder, biased towards the component. QFN68 components frequently contained copper trace failures. Cross-polarized microscopy of the CABGA192 interconnects revealed recrystallization of the subsidiary grains in the region surrounding the failure site, consistent with strain-induced microstructural evolution. Scanning electron microscopy of the chemically etched QFN68 copper traces revealed a mixed mode of inter- and transgranular cracking.

During Phase 2, a nonlinear dynamic response was observed across several durability and overstress trials. Fast Fourier Transform (FFT) analysis revealed dominant frequency content at odd integer multiples of the first natural frequency, consistent with superharmonic resonance behavior. This nonlinear response was caused by stress-stiffening effects due to large amplitude membrane strains due to the CFCF boundary condition. FFT and phase shift analyses of strain gauge signals, filtered around the third superharmonic frequency and positioned at Mode 3 antinode locations, confirmed that all test vehicles experienced some degree of mixed Mode 1 and Mode 3 participation, with significant piece-to-piece variability in the severity of the superharmonic response. A pure Mode 1 response would produce a 0° in-phase relationship between the Mode 3 antinode strain gauges, while a pure Mode 3 response would produce a 180° out-of-phase relationship. Since none of the test boards showed either of these, all test vehicles were confirmed to experience simultaneous participation of both modes, indicating that energy

was leaking from Mode 1 into Mode 3 via the superharmonic mechanism. Significant piece-to-piece variability in the severity of this energy transfer was also observed.

In the third phase, a multiscale global/local finite element modeling framework was developed and validated through experimental results. The global model (GM) was calibrated in three stages: component stiffening effect, natural frequency, and dynamic strain and acceleration response. Strain estimations, used in the durability plots, were extracted from this calibrated global model using volume averaged strains (xx-direction) on the unpopulated surface of the PWB representation. Nodal displacement fields from the calibrated GM were transferred to a detailed nonlinear local half model (LHM) of the CABGA192 and QFN68 components. A strain transfer function was developed to relate the volume-averaged Von Mises (VM) solder strain amplitude within the critical region of the corner joint to the PWB bending strain amplitude at the component edge, enabling solder strain amplitudes to be estimated for each durability test from the corresponding PWB strain response, and was used to develop the fatigue curves for each tested interconnect and component style.

The fatigue curves confirmed that all LTS interconnects are more fatigue resistant than SAC305 for both component styles. A notable difference in the fatigue behavior between the CABGA192 and QFN68 was observed, despite being tested on the same board under identical loading conditions. Strain triaxiality analysis revealed that the QFN68 solder joints operate primarily under compressive triaxiality, which suppresses void nucleation and crack opening. This results in a longer fatigue life at equivalent VM strain amplitudes compared to the CABGA192 joints. These findings indicate that fatigue life is influenced not only by VM strain amplitude, but also interconnect geometry.

In the hybrid LTS CABGA192 joints, failures consistently occurred within the SAC305 ball, rather than in the LTS paste region. A supplementary FEA simulation confirmed that the higher compliance of the LTS paste reduces cyclic strain in the critical neck region of the SAC305 ball. This strain redistribution mechanism provides a mechanistic explanation as to why hybrid LTS BGA joints outperform pure SAC305 joints, despite sharing the same failure site.

4.2. Contributions

The contributions from this thesis are provided below:

a. Conducted first harmonic vibration fatigue characterization of micro-alloyed LTS interconnects at the board level: Existing vibration studies of LTS materials focus primarily on eutectic SnBi alloys in BGA and LGA configurations. This work presents the first dataset characterizing the harmonic vibration durability of micro-alloyed LTS interconnects across multiple component styles.

b. First study to demonstrate that LTS interconnects consistently outperform SAC305 interconnects under harmonic vibration: LTS interconnects provide higher vibration durability life over SAC305 interconnects across four component styles (CABGA192, CTBGA228, CVBGA360, QFN68) and across multiple load levels. For the BGA components, the LTS interconnects consisted of hybrid joints, which combine an LTS paste with a SAC305 solder ball. LTS interconnects still demonstrated superior durability to pure SAC305 joints, suggesting that even partial incorporation of LTS paste is sufficient to improve vibration fatigue resistance.

c. Provided first SN comparison for HCF of selected LTS interconnects against SAC305 HCF behavior: Lower-bound estimates for fatigue strain-life (SN) curves are developed for each tested solder interconnect for both the CABGA192 and QFN68 joints using a calibrated multiscale finite element modeling framework.

d. Demonstrated new global/local submodeling finite element approach for vibration fatigue assessment: A new FE methodology for three-stage calibration is demonstrated for estimating solder strain amplitudes under harmonic excitation by capturing: (i) the stiffening effect of the components, (ii) matching PWB natural frequencies, and (iii) matching PWB strain and acceleration responses. This approach provides a more rigorous validation standard than matching just the natural frequency.

e. Demonstrated influence of interconnect geometry on fatigue life through strain triaxiality: FEA-based triaxiality analysis reveals a fundamental difference in the cyclic stress state between the CABGA192 and QFN68 solder joints. QFN68 joints operate primarily under compressive triaxiality, which inhibits void nucleation and crack growth. CABGA192 joints operate more within the tensile triaxiality range, which promotes damage accumulation. This result explains why QFN68 interconnects display longer fatigue lives than CABGA192 interconnects at equivalent VM strain amplitudes, and demonstrates that interconnect geometry also contributes to fatigue life, not just VM strain amplitude alone.

f. Provided mechanistic explanation for the higher fatigue life of hybrid LTS BGA interconnects: Through FEA, the higher compliance of the LTS paste was shown to redistribute cyclic strain away from the critical neck region of the SAC305 ball,

reducing the local strain amplitude and providing a physical basis for the observed durability advantage of LTS BGA assemblies over pure SAC305.

g. Developed first demonstration of the role of nonlinear vibration on fatigue durability of CFCF PBAs results: FFT analysis at Mode 3 antinode strain gauge locations, filtered time history phase shift analysis between antinode gauges, and FEA simulations are used together to identify, quantify, and explain the mechanism behind superharmonic energy leaked from Mode 1 into Mode 3 in CFCF test configurations. This combined approach provides a methodology for detecting and assessing the unintended mode participation in vibration fatigue trials.

4.3. Future Work

There are several opportunities to build upon the findings presented in this thesis.

The durability dataset, developed in this thesis, contains scatter arising from variability in test conditions, PBA architecture, and nonlinear dynamic responses. Additional durability testing at a broader range of load levels and with a larger number of test vehicles per solder configuration would reduce this scatter and improve the statistical confidence of the fatigue models. Additional data points spanning a wider range of cycles-to-failure would also better define the transition region between low cycle and high cycle fatigue for each tested interconnect.

The fatigue models developed in this study are limited to two component types, the CABGA192 and QFN68. Extending the modeling framework to additional component styles, such as the CTBGA228, CVBGA360, and SMR1206, would provide a more complete set of

fatigue model constants across a broader range of interconnect geometries and aspect ratios. This would also allow the influence of strain triaxiality on fatigue life to be further investigated across a wider range of package styles.

Finally, future tests should consider making improvements to the test design to reduce sources of variability. The use of a more ridged shaker base plate would improve the transmissibility between the test vehicle response and base plate excitation, allowing for an increased load at the board level. Additionally, the nonlinear superharmonic response could be mitigated by increasing the bending stiffness of the test vehicle or by adopting an alternative fixturing scheme such as a cantilever beam configuration, which would suppress the membrane stiffening mechanism responsible for the observed superharmonics at higher excitation levels.

BIBLIOGRAPHY

“Performance Test Methods and Qualification Requirements for Surface Mount Solder Attachments,” IPC-9701A, 2006, https://www.electronics.org/TOC/IPC-9701A.pdf

A. Bharamgonda, M. Osterman, and A. Dasgupta, "CALCE Internal Report RSS_Spring2026_09," Center for Advanced Life Cycle Engineering (CALCE), University of Maryland, College Park, MD, USA, 2026.

A. H. Nayfeh and D. T. Mook, Nonlinear Oscillations. New York, NY, USA: Wiley-VCH, 1979, sec. 4.1.3, pp. 175–178

B. L. Brinkmeyer, “Thermal Characterization and Vibration of Solder Alloys, M.S. thesis, Dept. of Metallurgical Eng., Missouri University of Science and Technology”, Rolla, MO, USA, 2008, https://scholarsmine.mst.edu/masters_theses/4473/

B. M. Paquette, “Harmonic Vibration Testing of Electronic Components Attached to Printed Wiring Boards With SAC305 and Eutectic SnPb Solder”, M.S. thesis, Dept. of Mech. Eng., University of Maryland, College Park, MD, USA, 2010, http://hdl.handle.net/1903/11101

C. Choi and A. Dasgupta, "Fatigue of solder interconnects in microelectronic assemblies under random vibration," Procedia Eng., vol. 74, pp. 165–169, 2014, https://doi.org/10.1016/j.proeng.2014.06.243

CALCE SARA: Shock and Accelerated Reliability Assessment Tool, CALCE, University of Maryland, College Park, MD, USA. [Online]. Available: https://calce.umd.edu (accessed: Feb. 4, 2025).

Che, F.X., Pang, J.H.L., Vibration reliability test and finite element analysis for flip chip solder joints, Microelectronics Reliability, Vol. 49, No. 7, pp. 754–760, 2009, https://doi.org/10.1016/j.microrel.2009.03.022.

D. Farley, Y. Zhou, F. Askari, M. Al-Bassyiouni, A. Dasgupta, J.F.J. Caers, J.W.C. DeVries, Copper trace fatigue models for mechanical cycling, vibration and shock/drop of high-density PWAs, Microelectronics Reliability, Volume 50, Issue 7, 2010, Pages 937-947, ISSN 0026-2714, https://doi.org/10.1016/j.microrel.2010.03.004

D. Yun Chen and M. Osterman, "Reliability of corner staked surface mount packages," 2016 IEEE Accelerated Stress Testing & Reliability Conference (ASTR), Pensacola Beach, FL, USA, 2016, pp. 1-6, https://doi.org/10.1109/ASTR.2016.7762272

Da Yu, Abdullah Al-Yafawi, Tung T. Nguyen, Seungbae Park, Soonwan Chung, High-cycle fatigue life prediction for Pb-free BGA under random vibration loading,

Microelectronics Reliability, Volume 51, Issue 3, 2011, Pages 649-656, ISSN 0026-2714, https://doi.org/10.1016/j.microrel.2010.10.003.

Darbha, K., Okura, J. H., Shetty, S., Dasgupta, A., Reinikainen, T., Zhu, J., and Caers, J. F. J. M. (December 1, 1999). "Thermomechanical Durability Analysis of Flip Chip Solder Interconnects: Part 2—With Underfill." ASME. J. Electron. Packag. December 1999; 121(4): 237–241. https://doi.org/10.1115/1.2793846

Deng Yun Chen, Michael Osterman, Abhijit Dasgupta, Energy based modeling for temperature cycling induced tin silver copper solder interconnect fatigue life, Microelectronics Reliability, Volume 109, 2020, 113651, ISSN 0026-2714, https://doi.org/10.1016/j.microrel.2020.113651.

Derr-Haverlach, G. (2025). Narrow band random vibration reliability of a doped near eutectic tin-bismuth-based alloy with a large fine-pitch ball grid array device (Order No. 31994900). Available from ProQuest Dissertations & Theses Global. (3195958935). Retrieved from https://www.proquest.com/dissertations-theses/narrow-band-random-vibration-reliability-doped/docview/3195958935/se-2

Deshpande, A., Jiang, Q., Dasgupta, A., and Becker, U. (September 15, 2021). "Role of Nominal Stress State on Cyclic Fatigue Durability of SAC305 Grain-Scale Solder Joints." ASME. J. Electron. Packag. September 2022; 144(3): 031006. https://doi.org/10.1115/1.4051647

E. Lin, “Effect of Isothermal Aging on SAC305 Harmonic Vibration Fatigue life”, M.S. Thesis, Department of Mechanical Engineering, University of Maryland, College Park, MD, USA, 2016, http://hdl.handle.net/1903/18420

European Commission, Restriction of Hazardous Substances in Electrical and Electronic Equipment (RoHS) Directive, Environment – Waste and Recycling, European Commission, (accessed: Mar. 18, 2026), https://environment.ec.europa.eu/topics/waste-and-recycling/rohs-directive_en

F. X. Che and J. H. L. Pang, "Vibration reliability test and finite element analysis for flip chip solder joints," Microelectron. Reliab., vol. 49, no. 7, pp. 754–760, 2009, https://doi.org/10.1016/j.microrel.2009.03.022

F. X. Che et al., "Development and Assessment of Global-Local Modeling Technique Used in Advanced Microelectronic Packaging," 2007 International Conference on Thermal, Mechanical and Multi-Physics Simulation Experiments in Microelectronics and Micro-Systems. EuroSime 2007, London, UK, 2007, pp. 1-7, https://doi.org/10.1109/ESIME.2007.360018.

H. Fu et al., "iNEMI project on process development of BiSn-based low temperature solder pastes: Part III: Mechanical shock tests on POP BGA assemblies," 2018 International

Conference on Electronics Packaging and iMAPS All Asia Conference (ICEP-IAAC), Mie, Japan, 2018, pp. 13-18, https://doi.org/10.23919/ICEP.2018.8374660

H. Ma, J. C. Suhling, Y. Zhang, P. Lall and M. J. Bozack, “The Influence of Elevated Temperature Aging on Reliability of Lead Free Solder Joints,” Proceedings of 57th Electronic Components and Technology Conference, pp. 653-668, Sparks, NV, USA, 2007, https://doi.org/10.1109/ECTC.2007.373867

H. Nayfeh and D. T. Mook, Nonlinear Oscillations. New York, NY, USA, Wiley, 1979, sec. 6.3.2.

H. Zhang, F. Mutuku, and H. Wang, "The Challenge of Lower Temperature Soldering for Large Ball-Grid Array (BGA) Board-Level Assembly Phase 1. Processing," J. Surf. Mount Technol., pp. 2–14, Jan. 2026, https://doi.org/10.37665/jqvy6470

Hower, Jonathan. "DROP DURABILITY ASSESSMENT OF ELECTRONIC ASSEMBLIES UNDER OFF-AXIS LOADING WITH SKEWED FIXTURES." , Aug. 2025., http://hdl.handle.net/1903/34735

C. Ume and T. Martin, "Finite element analysis of PWB warpage due to cured solder mask-sensitivity analysis," in IEEE Transactions on Components, Packaging, and Manufacturing Technology: Part A, vol. 20, no. 3, pp. 307-316, Sept. 1997, https://doi.org/10.1109/95.623025

I. Maus et al., "Characterization of epoxy based highly filled die attach materials in microelectronics," 2017 18th International Conference on Thermal, Mechanical and Multi-Physics Simulation and Experiments in Microelectronics and Microsystems (EuroSimE), Dresden, Germany, 2017, pp. 1-7, https://doi.org/10.1109/EuroSimE.2017.7926237.

I. Olatunji, A. Deshpande, M. Bascolo, A. Dasgupta, U. Becker and G. Jokai, “Fatigue life of Copper Traces in Ball Grid Array (BGA) Assemblies under Sequential Harmonic Vibration and Temperature Cycling,” Proceedings of 23rd International Conference on Thermal, Mechanical and Multi-Physics Simulation and Experiments in Microelectronics and Microsystems (EuroSimE), pp. 1-5, St Julian, Malta, 2022, https://doi.org/10.1109/EuroSimE54907.2022.9758863

I. Olatunji, A. Deshpande, M. Bascolo, A. Dasgupta, U. Becker and G. Jokai, "Durability of Copper Traces in Ball Grid Array (BGA) Assemblies under Sequential Harmonic Vibration and Temperature Cycling," 2022 23rd International Conference on Thermal, Mechanical and Multi-Physics Simulation and Experiments in Microelectronics and Microsystems (EuroSimE), St Julian, Malta, 2022, pp. 1-5, https://doi.org/10.1109/EuroSimE54907.2022.9758863.

I. Olatunji, M. Osterman, and A. Dasgupta, "CALCE Internal Report," Center for Advanced Life Cycle Engineering (CALCE), University of Maryland, College Park, MD, USA, 2026.

J. B. Libot, L. Arnaud, O. Dalverny, J. Alexis, P. Milesi and F. Dulondel, "Mechanical fatigue assessment of SAC305 solder joints under harmonic vibrations," 2016 International Conference on Electronics Packaging (ICEP), Hokkaido, Japan, 2016, pp. 231-236, https://doi.org/10.1109/ICEP.2016.7486818

J. H. Porter and M. R. W. Brake, “Tracking superharmonic resonances for nonlinear vibration of conservative and hysteretic single degree of freedom systems”, Mechanical Systems and Signal Processing, Volume 215, 2024, 111410, ISSN 0888-3270, https://doi.org/10.1016/j.ymssp.2024.111410.

J. W. Y. Kong, Jang-Kyo Kim and M. M. F. Yuen, "Warpage in plastic packages: effects of process conditions, geometry and materials," in IEEE Transactions on Electronics Packaging Manufacturing, vol. 26, no. 3, pp. 245-252, July 2003, https://doi.org/10.1109/TEPM.2003.820806

Kim, J.Y., Yoon, E.J., Chang, S.J. et al. A study on the determination of optimal reference spectrum for random vibration control in environmental vibration test. KSME Journal 10, 246–254 (1996). https://doi.org/10.1007/BF02953663

Kim, Y. K., Lee, S.-M., Hwang, D.-S., & Jang, S., “Analyses on the large size PBGA packaging reliability under random vibrations for space applications,” Microelectronics Reliability, vol. 109, p. 113654, 2020. https://doi.org/10.1016/j.microrel.2020.113654

M. A. Hopcroft, W. D. Nix and T. W. Kenny, "What is the Young's Modulus of Silicon?," in Journal of Microelectromechanical Systems, vol. 19, no. 2, pp. 229-238, April 2010, https://doi.org/10.1109/JMEMS.2009.2039697

M. Song, T. S. Lui, L. H. Chen et al., "Resonant vibration behavior of lead-free solders," J. Electron. Mater., vol. 32, pp. 1501–1508, 2003, https://doi.org/10.1007/s11664-003-0121-3

Martin, J. C., Bharamgonda, A. A., Osterman, M., and Dasgupta, A., submitted, “Finite Element Modeling of Fatigue Life in Low-Temperature Solder Interconnects Under Harmonic Vibration,” ASME Journal, Apr. 2026, manuscript under review.

Martin, J. C., Bharamgonda, A. A., Osterman, M., and Dasgupta, A., submitted, “Experimental Fatigue Life Comparison of Low-Temperature Solders Under Harmonic Vibration,” ASME Journal, Apr. 2026, manuscript under review.

Martin, J.C., Bharamgonda, A.A., Osterman, M., and Dasgupta, A., "Low-Temperature Solder Vibration Durability," SMTA International, pp. 194–198, October 19, 2025. https://doi.org/10.37665/smEUQHO14789

N. Muthuram and S. Saravanan, "Fatigue life based study of Electronic Package Mounting Locations on Printed Circuit Boards Subjected to Random Vibration Loads", J. Electron. Test, vol. 40, pp. 761–776, (2024). https://doi.org/10.1007/s10836-024-06151-5

O. H. Chen, A. Molina, R. Aspandiar, K. Byrd, S. Mokler, and K. K. Tang, "Mechanical shock and drop reliability evaluation of the BGA solder joint stack-ups formed by reflow soldering SAC solder balls BGAs with BiSnAg and resin reinforced BiSn-based solder pastes," Proc. SMTA Int., pp. 215–222, Sep. 2015, https://doi.org/10.37665/smJNMEA29283

Osterman, M., & Mendelsohn, A. "Thermal Cycle Fatigue Life of Low-Temperature Solders". Proceedings of the SMTA International Conference (SMTAI), Surface Mount Technology Association, original publication year as in proceedings. CALCE, University of Maryland, College Park, MD, USA. https://doi.org/10.37665/smXHJGJ19902

Q. J. Yang, Z. P. Wang, G. H. Lim, J. H. L. Pang, F. F. Yap and R. M. Lin, "Reliability of PBGA assemblies under out-of-plane vibration excitations," in IEEE Transactions on Components and Packaging Technologies, vol. 25, no. 2, pp. 293-300, June 2002, https://doi.org/10.1109/TCAPT.2002.1010020

Q. Su, J. Pitarresi, M. Gharaibeh, A. Stewart, G. Joshi and M. Anselm, "Accelerated vibration reliability testing of electronic assemblies using sine dwell with resonance tracking," 2014 IEEE 64th Electronic Components and Technology Conference (ECTC), Orlando, FL, USA, 2014, pp. 119-125, https://doi.org/10.1109/ECTC.2014.6897276

Richards, H., Dasgupta, A., Bujanda, A., Tsang, H., and Bowman, M. (August 25, 2025). "Low-Cycle Fatigue of Sintered Silver in Polymeric-Substrate Printed Hybrid Electronic Assemblies Subject to Extreme Strain Induced by Mechanical Shock." ASME. J. Electron. Packag. December 2025; 147(4): 041103. https://doi.org/10.1115/1.4069321

S. Chakraborty, M. A. Maruf, G. R. Mazumder, J. C. Suhling, and P. Lall, "Investigation of the Tensile and Creep Responses of Mixed SAC-LTS Alloys with Varying Bi Concentration," Proceedings of the 2026 Intersociety Conference on Thermal and Thermomechanical Phenomena in Electronic Systems (ITherm), 2026.

S. Mokler, R. Aspandiar, K. Byrd, O. Chen, S. Walwadkar, K. K. Tang, M. Renavikar, and S. Sane, "The Application of Bi-Based Solders for Low Temperature Reflow to Reduce Cost While Improving SMT Yields in Client Computing Systems," in Proc. SMTA Int., Rosemont, IL, USA, Sep. 2026, https://doi.org/10.37665/smLWOND16110

S. Sahasrabudhe et al., "Low Temperature Solder – A Breakthrough Technology for Surface Mounted Devices," 2018 IEEE 68th Electronic Components and Technology

Conference (ECTC), San Diego, CA, USA, 2018, pp. 1455-1464, https://doi.org/10.1109/ECTC.2018.00222

Shetty, S., Lehtinen , V., Dasgupta, A., Halkola , V., and Reinikainen, T. (March 25, 2000). "Fatigue of Chip Scale Package Interconnects Due to Cyclic Bending ." ASME. J. Electron. Packag. September 2001; 123(3): 302–308. https://doi.org/10.1115/1.1362673

T. An, F. Qin, B. Zhou, P. Chen, Y. Dai, H. Li, T. Tang, “Vibration lifetime estimation of PBGA solder joints using Steinberg model, Microelectronics Reliability”,Microelectron. Reliab., vol. 102 (2019), p. 113474, 2019, https://doi.org/10.1016/j.microrel.2019.113474

T. B. Ratanawilai, B. Hunter, G. Subbarayan and D. Rose, "A study on the variation of effective CTE of printed circuit boards through a validated comparison between strain gages and Moire/spl acute/ interferometry," in IEEE Transactions on Components and Packaging Technologies, vol. 26, no. 4, pp. 712-718, Dec. 2003, https://doi.org/10.1109/TCAPT.2003.821685

U. Andreaus, P. Baragatti, Experimental damage detection of cracked beams by using nonlinear characteristics of forced response, Mechanical Systems and Signal Processing, Volume 31, 2012, Pages 382-404, ISSN 0888-3270, https://doi.org/10.1016/j.ymssp.2012.04.007.

W. Shen, Z. Lei, K. Liang, G. Wu, T. Zeng and S. Liu, "Effect of Warpage on Solder Joint Fatigue Life by Influencing the Solder Joint Shape in BGA Packages," in IEEE Transactions on Components, Packaging and Manufacturing Technology, vol. 14, no. 4, pp. 611-618, April 2024, https://doi.org/10.1109/TCPMT.2024.3372520

Xuejun Fan, Min Pei and P. K. Bhatti, "Effect of finite element modeling techniques on solder joint fatigue life prediction of flip-chip BGA packages," 56th Electronic Components and Technology Conference 2006, San Diego, CA, USA, 2006, pp. 9 pp.-, https://doi.org/10.1109/ECTC.2006.1645772.

Y. Zhang, Z. Cai, J. C. Suhling, P. Lall, and M. J. Bozack, "The effects of aging temperature on SAC solder joint material behavior and reliability," 2008 58th Electronic Components and Technology Conference, Lake Buena Vista, FL, 2008, pp. 99-112, https://doi.org/10.1109/ECTC.2008.4549956

Y. Zhou, M. Al-Bassyiouni and A. Dasgupta, “Harmonic and Random Vibration Fatigue life of SAC305 and Sn37Pb Solder Alloys,” in IEEE Transactions on Components and Packaging Technologies, vol. 33, no. 2, pp. 319-328, June 2010, https://doi.org/10.1109/TCAPT.2009.2036834

Y. Zhou, M. Al-Bassyiouni, and A. Dasgupta, "Vibration fatigue life assessment of Sn3.0Ag0.5Cu and Sn37Pb solders under harmonic excitation," ASME J. Electron. Packag., vol. 131, no. 1, p. 011016, Mar. 2009, https://doi.org/10.1115/1.3078195

Y.S. Chen, C.S. Wang, Y.J. Yang, Combining vibration test with finite element analysis for the fatigue life estimation of PBGA components, Microelectronics Reliability, Volume 48, Issue 4, 2008, Pages 638-644, ISSN 0026-2714, https://doi.org/10.1016/j.microrel.2007.11.006.

Yusuf Cinar, Jinwoo Jang, Gunhee Jang, Seonsik Kim, Jaeseok Jang, Effect of solder pads on the fatigue life of FBGA memory modules under harmonic excitation by using a global–local modeling technique, Microelectronics Reliability, Volume 53, Issue 12, 2013, Pages 2043-2051, ISSN 0026-2714, https://doi.org/10.1016/j.microrel.2013.06.018.

Zhang, Q., Lo, J. C. C., Ricky Lee, S. W., and Xu, W. (September 10, 2018). "Correlation of Warpage Distribution With the Material Property Scattering for Warpage Range Prediction of PBGA Components." ASME. J. Electron. Packag. December 2018; 140(4): 041005. https://doi.org/10.1115/1.4041064.